Title

Enhancing Anisotropy in ErCOT-based molecular magnets through dipolar coupling

Permalink

https://escholarship.org/uc/item/3j65s9th

Author

Bernbeck, Maximilian Gordon

Publication Date

2023

Peer reviewed|Thesis/dissertation

UNIVERSITY OF CALIFORNIA SAN DIEGO

Enhancing anisotropy in ErCOT-based molecular magnets through dipolar coupling

A Dissertation submitted in partial satisfaction of the requirements
for the degree Doctor of Philosophy

in

Chemistry

by

Maximilian Gordon Bernbeck

Committee in charge:

Professor Jeffrey Rinehart, Chair
Professor Brian Maple
Professor Alina Schimpf
Professor Mark Thiemens

2023

The Dissertation of Maximilian Gordon Bernbeck is approved, and it is acceptable in quality and form for publication on microfilm and electronically.

University of California San Diego

2023

DEDICATION

To Mom and Dad,

who gave me unconditional love and support for me to chase my dreams.

To Angelica, Tara, Carl, John, Sam, and so many more

who made everything in grad school worth it.

To Jake,

my fuzzy partner from the very beginning.

In loving memory of Großpapa and Omi,

whose brief time on earth made it all the brighter.

We miss you every day.

EPIGRAPH

"Miracles each and every where you look

And nobody has to stay where they put

This world is yours for you to explore

There's nothing but miracles beyond your doors"

− Joseph Frank Bruce and Joseph William Utsler

"Miracles" by Insane Clown Posse

"...Magnets, how do they work?"

− Joseph Frank Bruce and Joseph William Utsler

"Miracles" by Insane Clown Posse

TABLE OF CONTENTS

LIST OF FIGURES

LIST OF SCHEMA

LIST OF ABBREVIATIONS

SMM	Single-molecule magnet
SIM	Single-ion magnet
QTM	Quantum tunneling of the magnetization
SOC	Spin-orbit coupling
COT, COT^{2-}	1,3,5,7-cyclooctatetraene dianion
ErCOT	Containing the $Er^{3+}COT^{2-}$ fragment $[ErCOT]^{+}$
KD	Kramers doublet
DD	Dipole doublet
THF	Tetrahydrofuran
DME	Dimethoxyethane
OEt	Ethoxide anion
$O^{t}Bu$	*tert*-Butoxide anion/fragment
Me	Methyl anion/fragment
Bn	Benzyl (deprotonated toluene at the methyl group) anion/fragment
TMS	Trimethylsilyl functional group
RT	Room temperature
IR	Infrared
FIR	Far Infrared
FIRMS	Far Infrared Magnetospectroscopy
SQUID	Superconducting Quantum Interference Device
ZFC	Zero-field cooled
FC	Field cooled

ACKNOWLEDGEMENTS

It's dangerous for me to have tackled this as the last section of my dissertation, as now it threatens to double the length of the manuscript. I couldn't possibly do justice to the overwhelming wealth of love and support that those close to me have given to me and to those who made me into the person I am today. The family I have been blessed with and the people who have given me the gift of their friendship are the only reason I could make it this far. If I do not thank someone, it is not because I cherish them any less, but merely because I cannot even fathom the full extent of the love I have received.

I of course must start by thanking my wonderful family. My parents have made it their lives' mission to support me in pursuing any whim that crossed my mind. At every event, every performance, every ceremony, I could count on Mom and Dad being there to support me. They always encouraged me to succeed, and I've got to say, nothing gets you through your Ph.D. than having two parents who go by "Dr." (and, like, actual doctors. The kind you want in an airplane emergency). To my father, to Dad, Dr. Johannes Bernbeck, I can never express the number of roles you've taken to mold who I am now. As a kid, a protector; growing up, a role model; as an adult, a mentor and, at times, a verbal sparring partner. Throughout it all, though, you were above all things my best friend and my beloved father; you were someone who I could always count to jump into my corner whenever I needed you. And to Mom, Dr. Sabine (Käsgen) Bernbeck, you've always stood as a pillar of strength and resolve for me, but I'm most happy for how we only ever grow closer as mother and son. You have no idea how thankful I am that throughout my life, I knew I could come to you for with the hard questions. You never judged, you never turned me away, and now I could never imagine a world where I love you more.

Alongside them is my younger sister Karina, whom I cherish and hold dear to my heart. We haven't always been the kindest to each other – actually, if memory serves, we've always been a pair of gremlins who would fight at any opportunity. I wouldn't dream of another partner in crime growing up, though; when it came time to buckle down and grit our teeth, there's no one I'd count on more than my little sister. Below the veneer of constant teasing and harsh tones, I'm glad we have a bond that will withstand any trial. And of course, my older sister Stephanie and the wonderful family she's brought to us: Mike, Adeline, and Amelie. You give me hope that I'll be able to capture a fraction of the wonderful new story you've made for yourself.

Even beyond the warmth of home I have been surrounded by the love of my family. Grandma Lily, you were a beacon of inspiration through any storm. It would be enough to see how far you came in your own life to the point of bringing our family to the lives we are able to lead now, but you go the extra mile and even a few more to bring as much joy and support to others as you could possibly muster. Thank you for inspiring me to always hunger to learn more. Meine Lieber Opa, Günther, ich werde dich immer gern lieb haben. Ich kann dein Herz immer fühlen über das ganze Meer. To Großpapa, grandpa Volkert, and meine liebe Omi, Liesel, I miss you dearly. Thank you for the love you showered me with growing up, and I look forward to when I will see you again. To all my aunts and uncles – from the inspiring and bombastic Franzi and Ken, to the infinitely warm Mark and Michelle, to my second German home away from home with Ralf and Greta – because of you I know that I can find a home wherever I am, and if it isn't already there it will come and find me.

I figured that it would be appropriate to punctuate me gushing about my family with thanking the second sort of family who found and fostered me away from home. The nucleus of this family is of course the Rinehart group and the community at UCSD. If I were to go back

and restart my doctoral work a thousand times, I don't think I could have been happier with anyone but Prof. Jeffrey Rinehart as my advisor. There are very few places in the world where you can find such a pronounced duality of genuine ubiquitous curiosity and grounded, profound compassion. Over the last six years, I don't know whether Jeff's helped me grow more as a scientist or as a person. I feel privileged to have been able to call him a mentor, and I am grateful to be able to call him a friend. I owe just as much to the rest of the group, with whom I've spent as much time laughing over drinks as I have discussing science in the office. To Angelica – for me, there might not have been a crossing of the finish line if it weren't for you. You rocket through life with a flair that makes it impossible to resist just trying to keep up. I'll always cherish what we could share, from pondering science over coffee in the morning to the late-night explorations of life's hidden truths in between working up reactions. We've been to hell and back, and I'd say it barely cracks the top 5 of our adventures. Tara, you've been that spot of sunshine in lab that refused to go out no matter how hard it got. I'd say far more people than just I am grateful that you're there to improve their day. I'm grateful to Kyle and Dr. Phil (I'm sorry); you somehow toed the line between being the stoic pillars of the lab and friends I could confide in who weren't afraid to be a little goofy. Zach, despite reminding everyone that sometimes we don't need to take everything so seriously, you've got a momentum that I'm excited to see, and I'm excited to see what you'll be up to. I had to save Max for last to best stabilize the superposition of our and Angelica's delocalized brain cell. In the short time I've known you, I'm both giddy to see what science you'll be up to and grateful for the good times you've been able to share with us. While you've been Max″ thus far to help graph us easier, with my departure I wish to bestow you with my phase angle. You can cut it out at the end of this paragraph here. (′)

I also have to thank the magnet folk who've helped me get here but have since left the group. Dr. Alex Mantanona – it feels good to be able to say that. You said in your dissertation that I felt like I was like a (slightly [extremely] annoying) little brother; the feeling is mutual. You brought me in to this group (with the help of certain monkey-based headware), and by God you were always there to help lead me through everything while growing into an expert scientist in your own right. The size of your brain is only eclipsed by the room you somehow make for the people around you in your heart. It's such sweet justice that you've found someone as willing to spread her love as you are in Nenny. I also want to thank Dr. Jeremy Hilgar, who was tasked with picking me up on day one and getting me on my feet. While by the end of our time we may not have always seen eye-to-eye, I will always be grateful that you pushed me to build enough momentum to get my footing in grad school. Dr. Ben Zhou (yes, I'm going to keep using their titles. These people worked *hard* for them, dammit!) and Dr. Yijun Xie both brought their own brands and flavors of life to the lab that made it the cocktail of personalities that it was. I also want to shout out the undergraduate alumni who helped us play with molecules, from my own capable mentee Joanne to folks like Brandon, McKenna, and the rest of the magnetic ensemble who have been part of the Rinehart group.

It's come to my attention now that I've spanned pages of praises to sing about those near and dear to me, and I've barely been able to scratch the surface. I hope that it's clear that any brevity from here on out isn't for any disparity or lack of affection, but rather so that this document doesn't become a textbook-length autobiography with a little bit of science as a footnote. It would honestly feel like an understatement to say that the Schimpf group practically felt like the second half of a bigger group (I affectionately call us the Schineharts). Prof. Alina Schimpf herself, alongside being on my dissertation committee, is someone I'm happy to be

able to call my friend. If I wasn't staying late into the night talking about some new project with Jeff, it was because I was instead staying late to chat about whatever was occupying our mind that week. Carl, you felt less like a doppelganger and more like my reflection in the mirror. I swear we worked on the same software (for better or for worse), and we clicked immediately. I've been enormously happy to have you and Carly as my friends. I arrived with Dr. Alec Rachkov for the same visitation weekend, we joined labs who worked closely together as friends and colleagues, and then we defended our dissertations within the same week. You've been a great friend throughout school; I think you're going to be a fantastic teacher. Things were always kept fresh with Dr. Jessica Geisenhoff and Dr. Liana Alves; I still insist to you respectively that chlorofluorocarbons are real and that board games are fun. I always enjoyed getting Dr. Linfeng Chen excited about his science, and I hope to be able to ever get close to his ability to just crank out results. Everyone else I've known in the Schimpf group has been an absolute joy to get to know, and you all made grad school a bit more bearable.

I couldn't possibly neglect how much the Figueroa group felt like an extension of our group as well. From when I arrived, the old guard of Dr. Mikey Neville, Dr. Myles Drance, Dr. Alejandra Arroyave, Dr. Kyle Mandla, and Dr. Joanne Chan showed me how you could put in the hard work and manage to stick together as a unit. Since their graduation, the new group has become an inseparable group that I can always look to for support. Whether I'm bouncing between crystallographic curiosities and dumb innuendos with Ritchie, catching up on life's latest events with Adam, pondering life with Sean, or just resorting to pure cynicism with Krista. I've also been happy to know people like Dr. Vincent and the many undergrads who came through, like Josh/Ritchie and Viet, who I know are going to blow us out of the water with what they will be accomplishing soon.

I haven't even finished talking about the friends I have in the same building, let alone at UCSD. I'll have to begin going a bit more rapid fire. Thank you to Eleanor who, on top of being an amazing friend with whom I could share a passion of memes, cats, and whatever random bit of internet culture came across my timeline that day, encouraged me to cause a few problems on purpose with the goal of making the world a better place. Thank you to the brilliant minds and warm hearts in the Kubiak lab, especially Dr. Nicole Torquato and Joe. I could always count on having a friendly face nearby with whom I could share whatever was on either of our minds. Plus, you helped me learn (somewhat unwillingly) a lot more about glove box construction and computational rabbit holes. I'll always hold a special place in my heart for Sam Kruse, who struggled with and supported me through the rolling earthquakes that were our first two years in grad school. I'm so happy that you've found joy in your life, and I'm grateful that you and your fuzzball Eddie could share it with me. Once the pandemic hit, I wouldn't have made it without the love and support of Dr. John Lopp. You kept me strong during lockdown; I'm just glad I was able to get stronger with you! Those park goers will never unsee us. I'm so happy you were able to break free and find your path. And to Dr. Ryan Holland – though we didn't get very long to get to know each other, I feel like we instantly acted as if known each other for a decade. Thanks for reassuring me I could make that final push.

So many other people outside have also welcomed me with open arms and stayed with me throughout my time here. I'm especially happy to have had my close friend Dr. Tucker Huffman since we first checked in to our Berkeley dorms ten years ago. You're a constant inspiration, and as much fortune as you've had in setting up roots and establishing a family with Danielle down here, you also bestow as much of a blessing on those who have the luck to know you. There's also Greg, who must be among the nicest people I've ever met by playing around

with cardboard rectangles. Please always stay the absolute joy of a person who emanates positivity in whatever space you are in. If no one was available nearby, I knew I could also count on my old Berkeley roommates, Shehan and Gabby, who were but a message away on Discord. It's amazing that through the years it doesn't feel like we've grown apart at all. The same could be said for my friends from all the way back in elementary in high school. My grade school playground best friend Jacob, for whom my oldest cat is named, ended up moving down to San Diego with me and riding through the wonderful chaotic mess that was our first year. I even had my home-away-from-home-but-still-at-home with my old high school clique managing to stay in contact; many late nights were spent musing with Cari, Kurt, and Josh, and I'm even still hitting them up as I'm writing this ode to them. I can't even count how many more people have been instrumental in my life, and I want each and every friend I've made over the years whom I haven't mentioned to know how much they've meant to me.

The many people in academia that I've had the pleasure to work with managed to let me do cool science while constantly fueling the fire of my excitement for it. There was no better community to get me into this than Prof. John Arnold's research group at UC Berkeley, with whom I was lucky to spend my undergraduate research days. Dr. Jessica Ziegler taught me the ropes of synthetic chemistry, and I credit her entirely for any success I have in it today. The rest of the group's members; Dr. Michael Boreen, Dr. Trevor Lohrey, Dr. Mark Straub, Prof. Alison Altman, Prof. Stephan Hohloch, Dr. Bernard Parker, Dr. Ben Kriegel, Dr. Mary Garner, and Dr. Nick Settineri, showed me the type of lab dynamic I should strive for and tried to build at UCSD. My two partners in chemical crime, Dr. Alexandra Brown and Angela Shiau, pulled me into the research world to start with, and for that I'll always be grateful. I can't speak of Berkeley chemistry without recognizing the rest of the amazing community that I called home,

including Dr. Stephen von Kulgelgen, Dr. Micah Ziegler, Dr. Alec Christian, and the rest of the grads who both taught me the wonders of their chemistry and served me way too much beer.

I'll try to wrap this up soon; I want to be able to give a brief shout out to those who helped me get here. Every teacher, every coach, every counselor and mentor shaped me and propelled me to where I am. I want to give particular thanks to Mrs. Eckert and Mrs. Bailey, who first tried to inspire me to reach a little further, to Mr. McVicker, who taught me that being a little weird makes life that much more fun (and to maybe let my head be quiet every now and then), Mrs. Tajima, who taught me to walk a mile in someone else's shoes, Mr. Jones, who's the entire reason I'm in chemistry to begin with (your pyrite pirate made it), Mrs. Curie (yeah, I know), who literally whipped us into shape for AP Chem (I kept those mothballs until I left for college), Mrs. Brucculeri and Mrs. Grimshaw, who went the extra mile to make sure I knew I was always loved and made school a little more like home, Mr. Kennedy and Mr. Hooper, who were happy to just talk about whatever my teenage mind thought was important (in either English or German), and of course Coaches Torres, Cadwallader, Fitzgibbons, and the rest of my wrestling team, who taught me what true grit really was and how I could use mine to push through anything that came in my way.

There are many groups that really made life worth living by just being fantastic spaces. My home Sigma chapter of Alpha Chi Sigma has given me many lifelong friends, one of whom is Jeff himself! The gaming community at Brute Force Games is honestly a model for how to have a good time in public while allowing everyone to be themselves. Thanks to them it was always an absolute blast to play games and never felt as though someone was unwelcome, which is probably why my bank account is a lot emptier than it would be if I wasn't addicted to your cardboard rectangles. Lastly, I have to thank the barista team at Twiggs, who serve an

amazing cup of coffee and honestly form the backbone of the University Heights community. Sunny days won't be quite as bright without a cup of their coffee in hand.

I want to close out this section with all those who kept the science flowing freely throughout my Ph.D. First, I must thank Dr. Milan Gembicky, without whom none of the many crystal structures you see in this dissertation would be able to exist. Whether I was setting up a difficult experiment, trying to figure out a particularly annoying disorder model, or dealing with more twins than a maternity ward, Milan acted as my crystallographic guru. But besides that, I always knew that I could come to him for some great stories, better conversations, and the best espresso on campus. With him is Dr. Jake Bailey, whom I've had the pleasure of shooting the breeze with while he was a student and now as our newest crystallographer. I also had the privilege of getting to know Dr. Han Nguyen, Dr. Curtis Moore, and Prof. Arnold Rheingold and could absorb some of their crystallographic expertise via osmosis. Dr. Anthony Mrse could simultaneously keep every NMR instrument running while managing to keep you engaged with whatever obscure hobby you found in life that he somehow also was an expert in. I thank our collaborators in Dr. Mykhaylo Ozerov, Prof. Michael Nippe, and Prof. Gregory Nocton for the fascinating science we could share. I must definitely thank Prof. Henry La Pierre, without whom I would be unemployed, for the fantastic opportunity to work as a postdoc after graduation. I was gifted with an extraordinary committee. I have already sung Prof. Schimpf's praises, but my committee members Prof. Mark Thiemens and Prof. Brian Maple always approached my science with such raw enthusiasm and genuine curiosity that I would leave my exams feeling more refreshed than when I went in. I also must thank Prof. Clifford Kubiak, who acted on my committee up until my defense. He has a zest for chemistry and his fellow scientists that's contagious, and his advice during my earlier examinations was appreciated and largely helped

guide me in that time. My love for teaching was fostered by Prof. Thomas Bussey, and since my first quarter where I had the pleasure of teaching for him, he has been an encouraging role model in effective and compassionate mentorship. Much the same could be said about Dr. Rudolphe Jazzar, whose enthusiasm for teaching was only matched by his incessant need to arrive at crystallography just before me to take the last available instrument. I couldn't possibly do justice to everyone, so I'll finish off by saying that the people I've met in the time I have been able to pursue science are what make it worth it. I'm happy to say I've surrounded myself with people who don't just make my life better but have also made *me* better.

Anyone who knows me would be shocked if I finished this section without gushing about my fuzzy partners in crime. The three closest people in the world to me aren't even people – my two kittens Latte and Chamomile and my old man Jake have stuck with me through thick and thin. My two little girls have only recently entered my life in summer 2022, but they've already made their home in my heart in between the hours rocketing around my apartment and curled up purring on my chest. The one who's been with me through it all, though, is the boy himself, Jake. This is a cat I've had with me since I was finishing elementary school, and as of writing he just celebrated his 17th birthday. This cat is old enough to be my brother, and, like I've shown off thousands of times to anyone within arms' reach, he's secured a permanent spot as part of my soul. I'm so blessed to have had him as part of my world, and he's given me the best gift possible by sticking with me throughout my entire journey.

With that, I wrap up my acknowledgements by thanking you for reading any of this. While I would of course be happy for you to find any joy or curiosity when reading my work, at the very least I am happy that the village that raised me to be who I am has been recognized, and that someone else now knows about the folks who got me here.

The material in Chapter 2 of this dissertation was adapted from: Bernbeck, M. G, Hilgar, J. D, Rinehart, J.D. "Probing axial anisotropy in dinuclear alkoxide-bridged Er–COT single-molecule magnets". *Polyhedron*., **2020**, *145*, 114206. The dissertation author is the primary author of this publication. Reproduced by permission of The Royal Society of Chemistry.

The material in Chapter 3 of this dissertation is currently in preparation: Bernbeck, M.B., Orlova, A.P., Gembicky, M., Hilgar, J. H. and Rinehart, J. D "Dipolar coupling as a mechanism for fine control of magnetic states in ErCOT-alkyl molecular magnets". The dissertation author was the primary author of this paper.

The material in Chapter 4 of this dissertation is currently in preparation: Bernbeck, M.B., Orlova, A.P., and Rinehart, J. D "Mapping long-timescale behavior in dinuclear halide-bridged ErCOT magnets". The dissertation author was the primary author of this paper.

2017   Bachelor of Science in Chemistry, University of California Berkeley

2017-2023   Teaching Assistant, University of California, San Diego

2023   Doctor of Philosophy in Chemistry, University of California San Diego

PUBLICATIONS

Intuitive Control of Low-Energy Magnetic Excitations via Directed Dipolar Interactions in a Series of Er(III)-Based Complexes
Orlova, A.P.; Hilgar, J.D.; Bernbeck, M.G.; Gembicky, M.; Rinehart, J.D. *J. Am. Chem. Soc.*, **2022**.

Probing axial anisotropy in dinuclear alkoxide-bridged Er–COT single molecule magnet
Bernbeck, M.B., Hilgar, J.D., Rinehart, J.D.; *Polyhedron*, **2020**.

Million-fold Relaxation Time Enhancement across a Series of Phosphino-Supported Erbium Single-Molecule Magnets
Hilgar, J.D., Bernbeck, M.B., Rinehart, J.D.; *J. Am. Chem. Soc.*, **2019**.

Metal-Ligand Pair Anisotropy in a series of mononuclear Er-COT complexes
Hilgar, J.D., Bernbeck, M.B., Flores, B.S., Rinehart, J.D.; *Chem. Sci*, **2018**.

FIELD OF STUDY

Inorganic Chemistry

ABSTRACT OF THE DISSERTATION

Enhancing anisotropy in ErCOT-based molecular magnets through dipolar coupling

by

Maximilian Gordon Bernbeck

Doctor of Philosophy in Chemistry

University of California San Diego, 2023

Professor Jeffrey Rinehart, Chair

An important focus in molecular magnetism is the delicate interplay of single-ion anisotropy and coupling between magnetic centers when designing the magnetic energy landscape to yield intended magnetic properties. Throughout this dissertation, we explore how these two perturbations interplay to create this environment and how dynamic behavior in magnetic systems are affected. In *Chapter 1*, we explore the current design principles dictating the state-of-the-art in molecular magnetic design and outline the parameter space we seek to

optimize. In *Chapter 2*, we explore the ability of highly charge-dense alkoxide bridging ligands to tightly bind highly anisotropic ErCOT units to couple them via the dipolar interaction and explore how this changes in asymmetric complexes. By introducing such a large perturbation, the beneficial aspects of coupling are tempered by increased mixing in states that are close in energy to each other. In *Chapter 3*, we describe the angular dependence of the dipolar interaction in a series of alkyl-bound ErCOT units by modulating the number of bridging ligands. By enforcing collinearity, we raise the energy separation within dipolar coupled states to increase the temperature dependence of relaxation mechanisms below the first excited state. In *Chapter 4*, we extend the model describing the dipolar interaction beyond the ground state to describe long-timescale relaxation in a series of halide-bridged ErCOT complexes. By using first-order perturbation theory, we can describe how magnetic states couple indpedently when well-separated and how magnetic relaxation is affected in turn.

CHAPTER 1: AN INTRODUCTION TO MOLECULAR MAGNETISM

1.1 The Road to Molecular Magnetism

Since lightning struck ancient magnetite, creating lodestone, magnetic materials have fascinated mankind. Our control of them and knowledge of their properties can be used as a trace of human history. At most points in history, however, such properties were attributed to the classically described bulk properties of a material. Macroscopic magnetic domains could be manipulated to align with an external magnetic field above a certain temperature. With miniaturization as the constant endeavor, however, the crossover from classical physics into quantum mechanics eventually came. The size domain pushed into the nanoscale, and the age of superparamagnetism dawned. Now, rather than the permanently magnetized multidomain samples of yore, single-domain magnetic particles with time- and temperature-dependent magnetization could be described as a system of spins overcoming a continuous double-well energy potential as described by Néel (which we will explore more later).[1,2]

Within this chapter, I hope to introduce magnetism at the molecular level so that the reader can have some intuition throughout the subsequent chapters. This will not be an exhaustive dissection of the field, as many have written fantastic reviews and textbooks that are far better suited to the task.[3–8] Instead, I hope that this is able to give a surface level survey of the field and serve as an introduction to one beginning to peruse molecular magnetism.

1.2 A Brief Description of Quantized Magnetization and Anisotropy
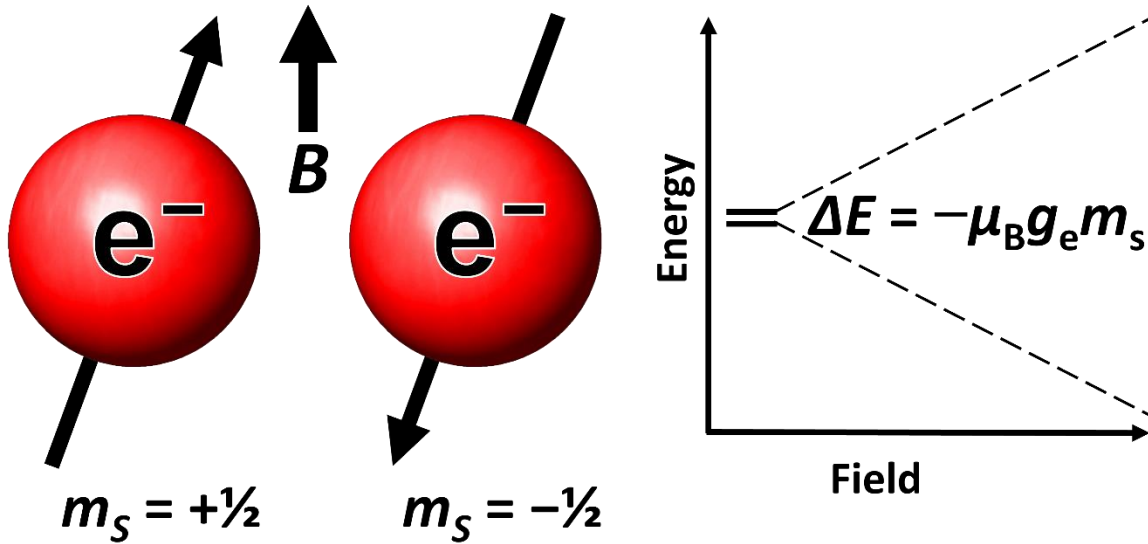
Figure 1.1: Energy change as a result of the Zeeman interaction of isotropic spin-½ particles under an applied directional field **B**

Let us take a step back and try to establish somewhat of an intuition on spin. While this dissertation chapter is not well-poised to give a thorough understanding of this topic, an introduction to the nature of quantum spin and how the change from isotropic to anisotropic spin manifests will be useful in contextualizing the concepts throughout this work. An electron's spin is an intrinsic property. As a point-like particle, it cannot rotate in the manner one would associate with a spin, yet it carries an inherent angular momentum. Coupled with the electron's negative charge, this results in an inherent magnetic moment. The spin state of a charged particle can thus be described by its tendency to align or anti-align with an applied field B (Figure 1.1). For example, a spin-½ particle like an electron is described as S = ½ consisting of two degenerate states with quantum number $m_s = \pm\frac{1}{2}$. Under an applied field, their energies evolve as the Zeeman interaction:

$$E = \mu_B g B m_s \quad \text{Eqn 1.2}$$

Here, μB is the Bohr magneton, a constant relating how a states' energy evolves under a magnetic field; g is the g-factor, a dimensionless ratio characterizing the magnetic moment and angular momentum of your magnetic center, and B is the applied field. This is expressed more generally as a Hamiltonian:

$$\widehat{H}_{zee} = \frac{\mu_B}{\hbar} gB\hat{S} \qquad \text{Eqn 1.3}$$

For a free electron, g_e is a constant very close to 2, only differing by a small anomalous correction that is known to very high precision. Its moment is *isotropic*, which is to say its spin angular momentum, and therefore its magnetic moment, is equally likely to be oriented in any direction. Upon applying a field, the moment is defined by the field direction (denoted as the z-axis in cartesian space by convention). When considering multiple possible field orientations, it can be useful to parameterize the field and spin operators into their x, y, and z components. Furthermore, as one might infer from our description thus far, many magnetic materials (such as those we will soon discuss) will have their states evolve in energy differently depending on the orientation of the magnetic field with respect to the main magnetic axes (Figure 1.2). The operator $\hat{S}$ can be described as a linear combination of operators $\hat{S}_x$, $\hat{S}_y$, and $\hat{S}_z$. These form a rank-3 tensor that can be more easily described as a 3×1 vector with $\hat{S}_i$ as its elements. Combined with a parameterized field and g-factor, these form the Zeeman Hamiltonian proper:

$$\widehat{H}_{zee} = \frac{\mu_B}{\hbar} [B_x \quad B_y \quad B_z] \begin{bmatrix} g_x & 0 & 0 \\ 0 & g_y & 0 \\ 0 & 0 & g_z \end{bmatrix} \begin{bmatrix} \hat{S}_x \\ \hat{S}_y \\ \hat{S}_z \end{bmatrix} \text{Eqn 1.4}$$

$$\Delta E_i = -\mu_B g_i m_s$$
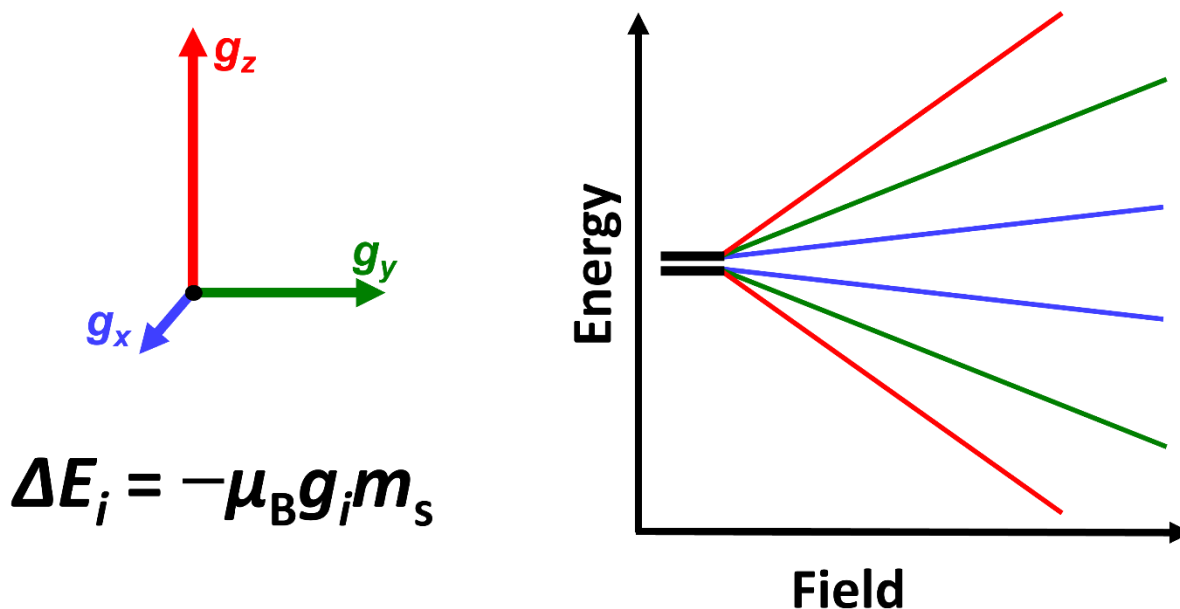
Figure 1.2: Qualitative representation of magnetic anisotropy. Pictured left is rhombic anisotropy, where all three axes differ in g. (Right) Zeeman diagram for cases when the field B is aligned along each anisotropy axis with each state color-coded to correspond to the axes on the left.

Now we are equipped to discuss *anisotropic* magnetic moments, wherein the energy of the system will evolve differently depending on the orientation of the external field. The axis along which the energy is maximally perturbed is described as the easy magnetic axis, and the axis along which the energy changes the least is the hard axis. Whereas an isotropic magnetic center has an equivalent energy upon application of a field along any axis, anisotropic centers have a field-orientation-dependent energy landscape. By increasing the moment along a particular axis, the ability for the spin to spontaneously flip decreases in turn (in the absence of any state mixing), as the energy required to do so increases proportionally. This is reflected in matrices describing the transition probability between states. Generally, larger moments perpendicular to the magnetization axes (transverse moment) increase these matrix elements, reflecting a more facile transition. Thus, we generally see more pronounced deviations from simple paramagnetic behavior arising from materials with increased anisotropy. This effect generally increases with the discrepancy between different axes. Several cases of anisotropy exist, and so one should

4

familiarize themselves with the appropriate terminology. We have already described the isotropic case where $g_x = g_y = g_z$. The most commonly sought after form of anisotropy is when the moment along one axis, typically set as the z axis, is much larger than g_x and g_y and the latter two can be considered equivalent ($g_x = g_y < g_z$). This case is termed uniaxial, easy-axis, or simply axial anisotropy. The opposite case – when g_x and g_y are equal and larger than g_z ($g_x = g_y > g_z$), is typically known as planar or easy-plane anisotropy (sometimes also denoted as axial, due to its symmetry about the z axis). Lastly, when all three g-factors differ, one is faced with rhombic anisotropy. Typically, one should assume in the rest of this manuscript that "highly anisotropic" refers to states resembling predominantly uniaxial magnetic anisotropy.

It is important to note that, despite ubiquitous and inevitable abuse of terminology, the intrinsic electron spin angular momentum does not alter its gyromagnetic ratio – it couples to orbital motion which introduces a spatial dependence. Therefore, when introducing anisotropic g values, it is vital to consider their underlying physical source as we will discuss in depth in later chapters. The use of g-factors as a representation of the increased orbital angular momentum is instead a useful simplification that allows us to treat our systems as pseudo-spin-only, and output states will be appropriately discussed as pseudospin states.

1.3 Early Single-Molecule Magnets

Within the past three decades, studies to understand the quantum mechanical nature of magnetic particles in the molecular realm have rapidly accelerated. Just before the discovery of single-molecule magnets (SMMs), low-dimensional materials, such as 1D magnetic chains, were developed to put to the test new theoretical models, such as the Heisenberg (isotropic limit) and Ising (axially anisotropic limit) descriptions of magnetic exchange.[9–13] In this time of growth, the first family of SMMs, $Mn_{12}OAc$, was born almost serendipitously (Figure 1.3, left).[14,15] This

molecule (with full formula $[Mn_{12}O_{12}(O_2CCH_3)_{16}(H_2O)_4]$) consists of two rings of Mn ions – an outer ring of eight Mn(III) and an inner ring of Mn(IV). Within each ring the dominant interaction is ferromagnetic coupling, or an additive effect of the constituent spins, leading to an S = 16 outer ring and S = 6 inner ring. These rings are then antiferromagnetically coupled to each other, leading to a subtractive effect of their spins. The resulting S = 10 ground state of the system is very well isolated from excited states with lower spin, allowing for this manifold to be described as a "giant spin" with microstates M_s = +10, +9….-9, -10. The degeneracy is then lifted by an axial magnetic anisotropy term resulting from orbital angular momentum generated by the delocalization across the cluster, leading to a progression of spin states with the highest moment states as the ground state, resembling the double-well potential in superparamagnetic particles (Figure 1.3, right). Such a double-well potential could describe magnetic relaxation, or reorientation of magnetic moment toward random equilibrium, via an Arrhenius equation:

$$\tau_N = \tau_0 e^{E/k_B T} \qquad \text{Eqn. 1.5}$$

wherein τ_N describes the characteristic relaxation time, τ_0 is an "attempt time" inherent to the material, E is the energy barrier of the well, and $k_B T$ describes the energy available to the system according to Boltzmann statistics.

When sweeping from positive to negative fields, $Mn_{12}OAc$ displayed nonzero magnetization when crossing through zero field, displaying remanence, and only transitioned to a negative magnetization at a large negative field, or its coercive field. If instead the sample was magnetized and the field was removed, the sample would initially retain a large percentage of its saturation magnetization. Such magnetization then decreased according to an exponential decay function, revealing the presence of slow relaxation dynamics. By measuring relaxation rates across several temperatures, the effective barrier, hereafter referred to as U_{eff}, could be found by fitting

to Eqn 1.5 to be 44 cm^{-1}, just below the predicted value of 52 cm^{-1}. Here was discovered the second defining trait of molecular magnets: quantum tunneling of the magnetization (QTM). In the molecular regime, the energy barrier could be undercut by quantum tunneling to spontaneously invert the spin of a particle. This process is temperature-independent, and is largely dependent on the planar, or transverse, terms of magnetic anisotropy, due to these terms allowing for mixing between states. This is further explored throughout this dissertation and in the Appendix.
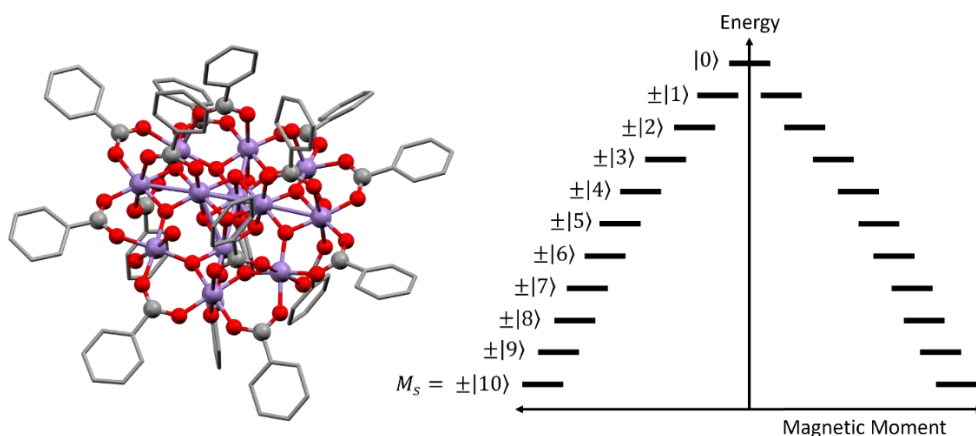
Figure 1.3: (Left) Representative structure of the Mn$_{12}$-OAc cluster (Mn$_{12}$O$_{12}$(O$_2$CPh)$_{16}$(H$_2$O)$_4$ pictured; Mn – purple, oxygen – red, carbon – grey) with hydrogens omitted and phenyl carbons represented as sticks for simplicity and clarity. (Right) Qualitative description of the zero-field splitting of the S = 10 ground state (not to scale).

Early design principles focused on the maximization of spin to consequently raise the spin-reversal barrier U_{eff}. Across metal systems incorporating such highly magnetic centers as iron and cobalt with nuclearities facilitating a spin value up to a staggering S = 83/2,[16] the state-of-the-art still lay with the Mn$_{12}$-OAc derivatives.[17] In analysis of these structures, it soon became apparent that maximization of the spin led to a drastic drop-off of axiality in the magnetic anisotropy due to the overlooked effect of mixing between microstates. Furthermore, in increasing nuclearities, clusters often became more isotropic in shape, removing the key role that the structure played in promoting magnetic anisotropy. Thus, the aim of building ever-larger clusters to facilitate high-performance molecular magnets pivoted to maximizing the magnetic anisotropy within a system.

1.4 Lanthanides and the Single-Ion Magnet

Here we turn our attention to the lanthanides – the oft overlooked metals that are not allowed to sit at the periodic table with the other elements. Following the isolation of a trivalent terbium bis-pthalocyanine complex in 2003,[18] they have overwhelmingly evolved into the elements of choice in the design of molecular magnets. In this pioneering work, trivalent lanthanides (Ln^{3+}) are sandwiched between two dianionic pthalocyanine ligands in a D_{4d} arrangement with an outer-sphere charge-balancing ligand (Figure 1.4). Only the Dy^{3+} and Tb^{3+} congeners displayed slow magnetic relaxation, but the latter had a record-shattering 230 cm^{-1} barrier. This corresponds reasonably with the calculated energy gap separating the magnetic ground state ($m_J = \pm6$) from the first and second excited states ($m_J = \pm5, 0$; $E \approx 400$ cm^{-1}). While the limitation of magnetic remanence to the two neighboring elements Dy^{3+} and Tb^{3+} invites further discussion into the design principles that have guided lanthanide-based molecular magnetism to the present day, it first requires a description of lanthanide microstructure to pinpoint the origin of such principles.
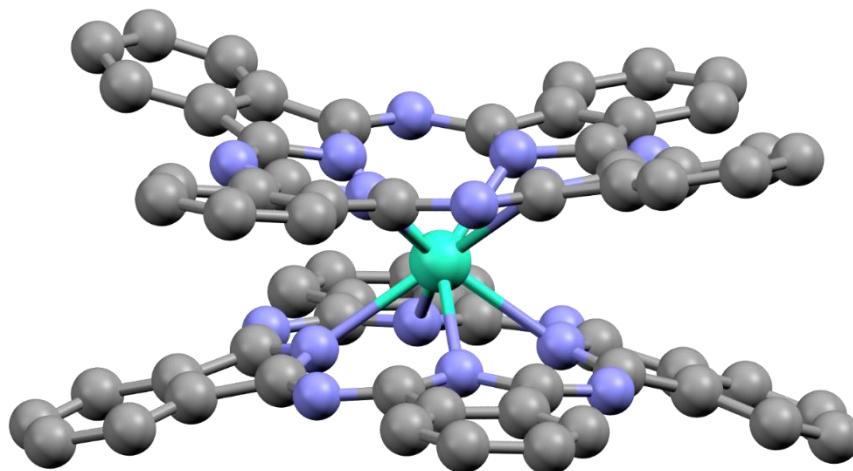
Figure 1.4: Representative structure of [Pc_2Ln]$^-$ (Carbon – gray; nitrogen – sky blue; terbium – greenish blue). Hydrogens and outer-sphere ions omitted for clarity.

First, a comment on the spin-orbit interaction as an origin of anisotropy is in order. This is more simply illustrated with the d orbitals of a transition metal ion. Beyond the relatively simpler description of a giant spin (though one would be foolish to describe spin as anything resembling simple), degeneracy in the spin-carrying d orbitals can promote a cooperative effect of the spin angular momentum of a single electron with the orbital angular momentum via spin-orbit coupling (SOC). To a first approximation, the presence of point charges near transition metal d orbitals will lift their degeneracy, splitting them according to the strength of the interaction and the symmetry of the crystal field environment.[19] In several such cases, the resulting orbital structure can promote anisotropy as long as several criteria are met.[5] First, an electron must be able to move between degenerate orbitals such that there is not a sizeable energy cost associated with doing so. Second, the degenerate orbitals must have an open state to which an unpaired electron can move freely following the Pauli exclusion principle. Last, the degenerate orbitals must be rotationally symmetric around the intended axis of anisotropy such that, when linearly combined, they form a spherical harmonic. While a classical description of electron motion does not reflect reality in this case, it is a useful shorthand for illustrating this origin of anisotropy. If an electron's spin is pictured as the moment generated by a spinning spherical shell of charge, the orbital angular momentum can be described as this charge revolving around the axis of anisotropy, generating a magnetic moment coincident with said axis. Such motion is only possible if the orbitals in question are rotationally symmetric, and the electron can only move if there is an available position for that electron to "hop" to. That is to say, existing in an orbital with nonzero m_L does not in and of itself impart orbital angular momentum; it is the motion between orbitals with different values of m_L that generates magnetic anisotropy.

In many coordination environments, the orbital angular momentum is considered quenched.[5] In most low symmetry coordination environments, the orbital degeneracy is lifted entirely, and no electron motion is allowed without external energy input. In cases where orbitals of opposite M_L are degenerate, such as d_{xz} and d_{yz} ($m_L = \pm 1$) or d_{x2-y2} and d_{xy} ($m_L = \pm 2$), spin-orbit coupling can be observed (Figure 1.5). If an unpaired electron is present in these orbitals (and the degeneracy is not lifted by structural distortions), anisotropy of the magnetic moment is expected to manifest around the z-axis.
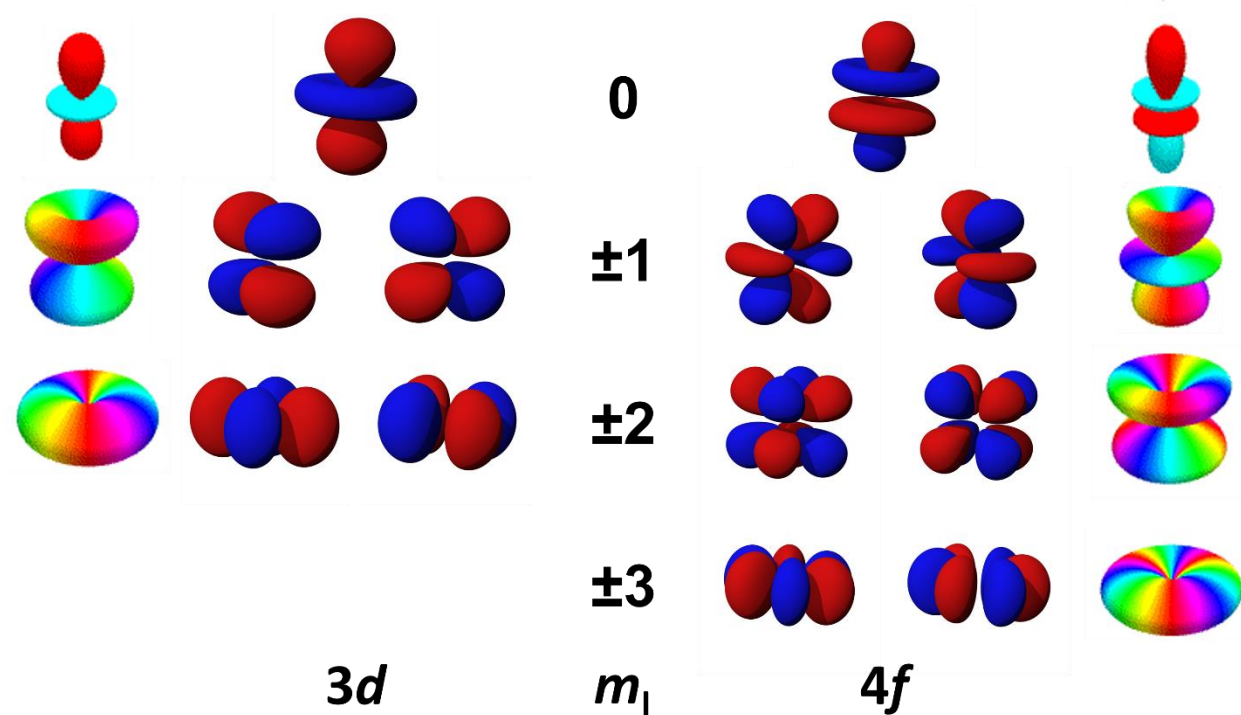
Figure 1.5: Spherical (outer, rainbow) and cubic (inner, red/blue) harmonics of the 3*d* and 4*f* orbitals. Color depicts phase of the eigenfunction; only one of two possible phases is shown for each spherical harmonic. Figure adapted from Wikipedia under Creative Commons[20–22]

Now, we return to the context of lanthanides. One important factor in the exceptional anisotropy of the trivalent lanthanide cations is the highly contracted nature of the 4*f* orbitals. Following the lanthanide contraction, electrons in the 4*f* subshell are buried beneath the core 5*s* and 5*p* orbitals, effectively shielding them from ligand interactions and drastically accelerating

their orbits.[19] Thus, whereas the description above illustrated SOC as a perturbation upon the crystal-field split states of a transition metal complex, the origin of anisotropy in lanthanide complexes can be described in much the opposite manner. While the spin-orbit coupling parameter is on the order of or smaller than the crystal field splitting parameter in transition metals, it is approximately an order of magnitude larger ($\sim$1000 cm^{-1})[7] for lanthanides. This means that the effect of the ligand environment (which for lanthanides is adequately described by the crystal field model to a first approximation) can be effectively described as a perturbation on the spin-orbit coupled energy levels. Consequently, S and L (and their constituent states m_S and m_L) are no longer good quantum numbers. Instead, the free ion is described by Russel-Saunders coupling, or LS coupling (Figure 1.6).[23] Here, J is a good quantum number, with a ground state consisting of $J = L + S$ (for more than half-filled 4f subshells) or $J = L - S$ (for less than half-filles subshells) according to Hund's rules.[19] Upon application of the crystal field, these states have their degeneracy lifted to produce the appropriate m_J sublevels.
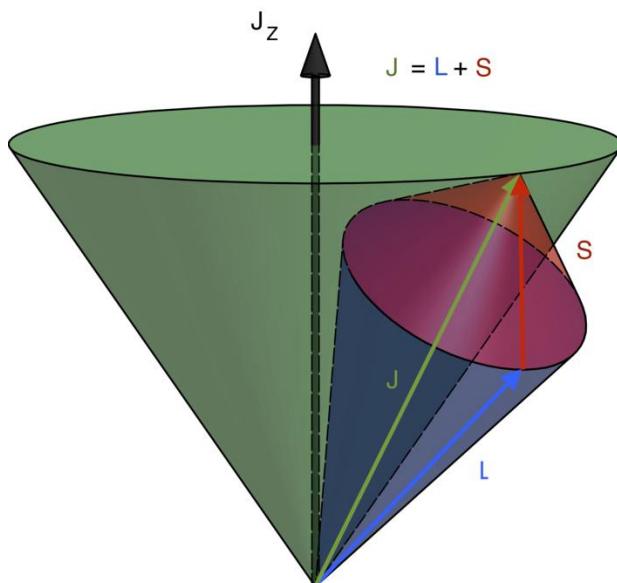
Figure 1.6: Pictorial representation of Russel-Saunders (LS) coupling. Adapted from Wikipedia under Creative Commons[24]

Here we can see the origins of anisotropy within the tricationic lanthanide series. For the late lanthanides, the magnetic ground state is that of the highest moment. Furthermore, due to spin-orbit coupling, the highest moment states have their magnetization oriented along the unique rotational axis. As we will soon see, these states can have large energy gaps, allowing for pure, well-separated spin-orbit coupled states. To reiterate: high, uniaxial anisotropy greatly reduced the possibility for QTM mechanisms. Additionally, well-separated pure states are less likely to mix to undercut the anisotropy. Consequently, through-barrier QTM can be suppressed (though not fully eliminated), making these ideal targets for SMMs.

1.5 Design Principles of Lanthanide Molecular Magnets

Finally, we are prepared to apply the theory we have discussed thus far to the synthetic design of lanthanide molecular magnets. We will focus specifically on Er^{3+} and Dy^{3+}, two of the most common lanthanides in SMM literature. Our focus and their ubiquity in literature follows from two main principles. First, the two ions have some of the largest ground-state moments among the lanthanide systems. Both Dy^{3+} ($4f^9$, $S = 5/2$, $L = 5$, Ground state term symbol $^6H_{15/2}$) and Er^{3+} ($4f^{11}$, $S = 3/2$, $L = 6$, Ground state term symbol $^4I_{15/2}$) have a $J = 15/2$ ground state, which are among the highest moment configurations among the lanthanide series. Furthermore, the two have a half-integer quantum number J, which indicates them as Kramers ions.[25] While the theory behind this is beyond the scope of this chapter, these states have inherent twofold symmetry at zero field, leading to a ladder of Kramers doublets as the energy landscape. For non-Kramers systems, i.e. integer quantum numbers S or J, states can more easily mix, removing this degeneracy and allowing for facile through-barrier relaxation processes.
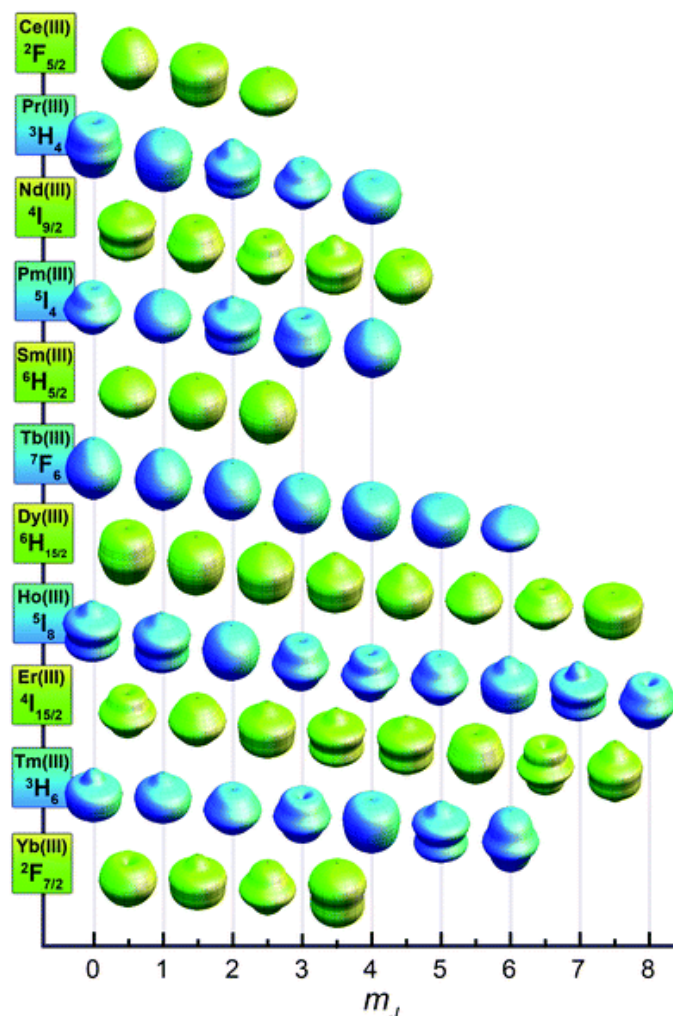
Figure 1.7: Approximate angular dependence of total $4f$ charge density for m_J states within the lowest-energy J manifold for each lanthanide. Figure reproduced from Rinehart et al.[26] with permission from the Royal Society of Chemistry.

When considering the charge density of the $4f$ orbitals, one can see a pattern when comparing the anisotropy of the subshells and the moment of their corresponding M_J states (Figure 1.7).[27] When considering the crystal field model, one may associate the shape of the charge cloud with the relative stability or instability of that state to exposure the charge density of a coordinated ligand. Such was the assertion of Rinehart and Long,[26] and this approachable empirical approach to synthetic design was followed by an explosion in research involving lanthanide molecular magnetism. When specifically considering Dy^{3+} and Er^{3+}, the two form an ironically

13

complementary pair (Figure 1.8). The high-moment microstates of Dy^{3+} have highly oblate, or disk-shaped, electron densities, whereas their low-moment microstates are mostly prolate, or cylindrical. Thus, the high moment states are most stabilized by a strictly axial coordination environment, while any equatorial contributions drive low-moment states down in energy and promote mixing of intermediate states. Contrarily, the high- and low-moment states of Er^{3+} are highly prolate and oblate, respectively, and SMM behavior is best promoted by equatorial crystal fields and impeded by axial ligand coordination. In more straightforward terms, binding ligands at axial positions 180° from each other should maximize SMM behavior in Dy^{3+}. The less-straightforward description of Er^{3+} describes that ligands should be bound such that they lie in the same plane, but they should not be in the same axial positions as were described for Dy^{3+}.
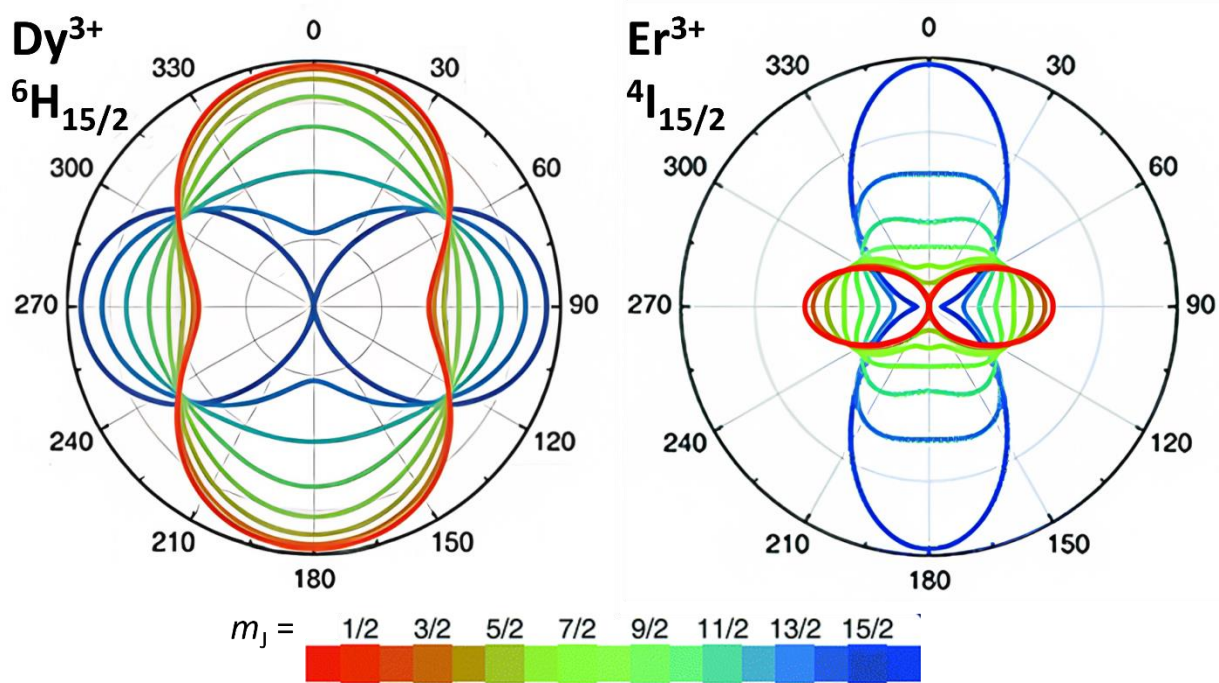
Figure 1.8: Calculated electrostatic potential of mJ states of lowest J manifold for Dy^{3+} (left) and Er^{3+} (right) in response to a point charge held 2.3 Å from the atom center. Scheme reproduced from Liu et al[28] with permission from the Royal Society of Chemistry.

Finally, we have enough context to confront the current state-of-the-art of our two chosen ions. Some final context is needed, however, in interpreting the data used to describe the relative

"quality" of different SMMs. Primarily, we must add somewhat to our description of relaxation (Figure 1.9). First we must adjust our definition for by far the most popular parameter in the field – U_{eff}. Whereas the description of a simple thermal barrier was sufficient in mesoscale superparamagnetic particles, the highly quantized nature of the single-ion magnet (SIM) combined with the nonzero propensity for equilibrium to be established by a QTM process requires an appropriate adjustment to model. This over-barrier mechanism, commonly known as the Orbach process, involves the excitation to and the subsequent relaxation from a magnetic excited state coupled with the simultaneous absorption and emission of two phonons.[29,30] Such a process displays similar Arrhenius behavior as described above, and the destination excited state can be thought of as the new energy barrier that is below the "top" of the well, hence the "effective" terminology of U_{eff}. Furthermore, at any point during relaxation, the moment can spontaneously flip in a quantum tunneling process dubbed quantum tunneling of the magnetization (QTM). While the probability of a QTM event decreases dramatically with the moment of the states, it is never fully quenched in single-ion magnets due to the non-negligible degree of mixing present in all but the highest-symmetry molecules. Last, while these two terms are sufficient for describing relaxation for myriad complexes, several show deviations from Arrhenius behavior far below the temperature associated with the QTM process becoming dominant. Thus, an additional phenomenological term was added to account for this – the Raman term.[30–33] This process involves a similar two-phonon process as in the Orbach mechanism, except this excitation involves virtual excited states not predicted by the static magnetic energy manifold. A fourth process, the Direct process, is a one-phonon mechanism involving the relaxation through the energy barrier to a lower energy state of opposite sign. As we will exclusively be dealing with Kramers ions, however, we will not explore this term.[34–36] Our completed relaxation equation is now:

$$\tau^{-1} = \tau_0^{-1} e^{-\frac{U_{eff}}{k_B T}} + CT^n + \tau_{QTM}^{-1} \qquad \text{Equation 1.6}$$

where τ is the characteristic relaxation time, τ_0 is the characteristic attempt time for the Orbach process, U_{eff} is now a phenomenological fit parameter (which is associated with the inter-state energy), CT^n represents the Raman term with C (units $s^{-1}K^{-n}$) and n (unitless) as variables, and τ_{QTM} is the characteristic QTM rate. One can note from the reciprocal form of the equation that the relaxation rate is limited by the fastest process – that is, the largest (or fastest) term in this reciprocal form of the equation dominates relaxation at that temperature.
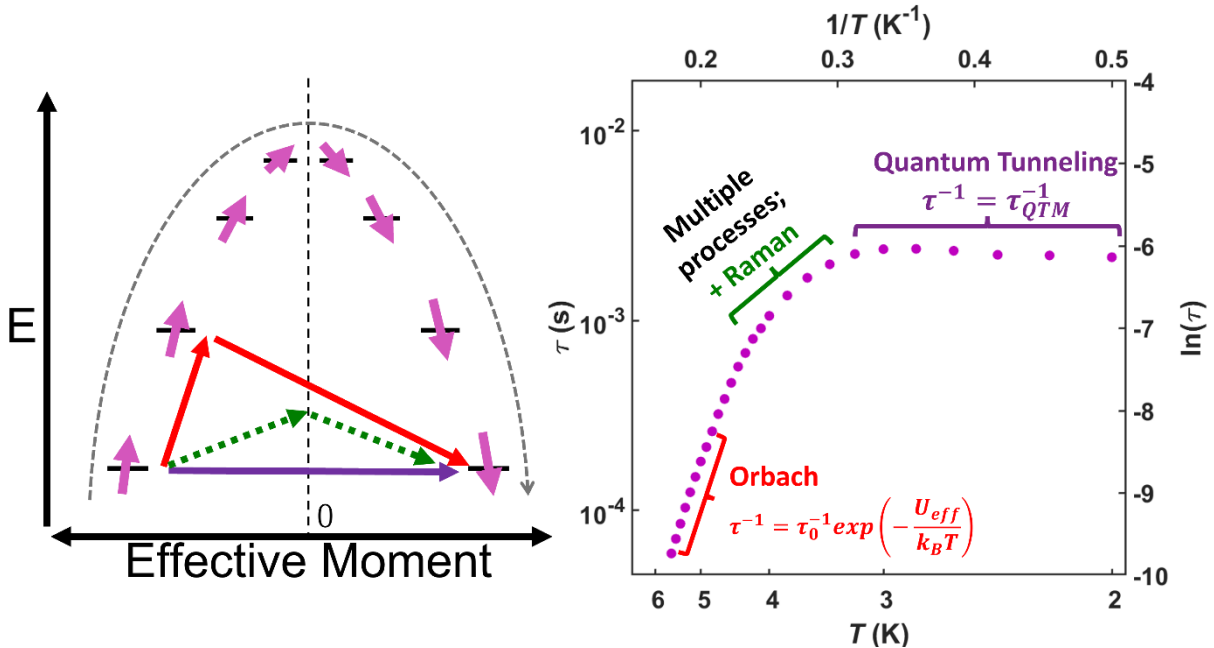
Figure 1.9: Generalized description of relaxation within molecular magnets. At high temperature, excitation from the ground state is expected to dominate relaxation, following an Arrhenius law in ln(t) vs 1/T. At intermediate temperatures, several processes can be observed to have similar rates, and Raman relaxation mechanisms to a virtual excited state can be observed. At the lowest temperatures, QTM is expected to dominate and effectively limit relaxation to a temperature-independent process. Relaxation date is of ErCOT(I)(THF)$_2$ (See section 1.6)

Other common forms of characterization include measuring magnetization as a function of field at a fixed temperature. The ability for the sample to resist demagnetization after saturation is a simple at-a-glance description of relaxation dynamics, and the opposing field at which magnetization finally vanishes, dubbed the coercive field, is most often presented as a description

of this quality (See figure 1.10, left). One must take caution, however, that this parameter is highly dependent on the field sweep rate of the experiment due to the dynamic nature of magnetic relaxation. Another common point of note is the so-called "blocking temperature," or the point at which the rate of demagnetization is so slow that one could describe the moment as effectively pinned like in a permanent magnet. Many definitions exist, including the highest temperature at which open hysteresis – or coercive magnetization – is observed and the temperature at which the characteristic relaxation rate is over 100 s.[6] While we shall not consider the blocking temperature a point of note within this chapter, the latter definition is recommended for the reader's own benefit due to the susceptibility to experimental nuance in coercivity measurements.
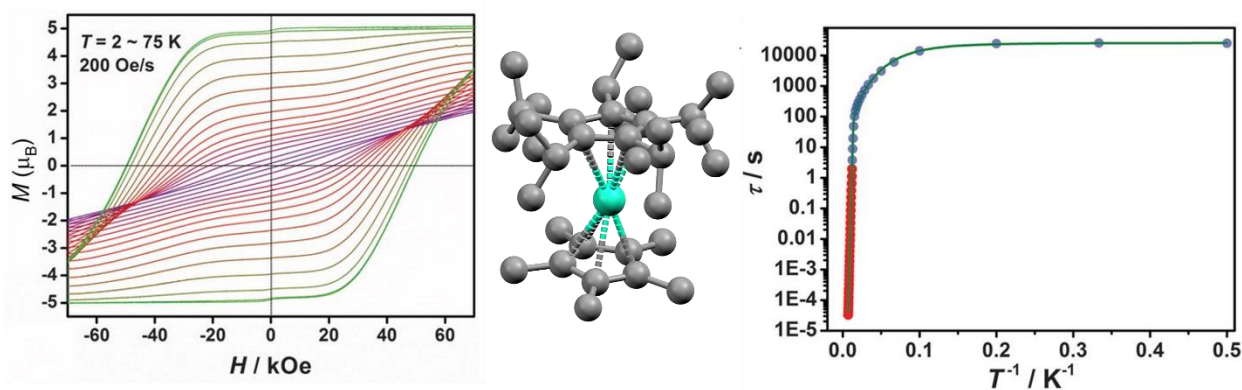
Figure 1.10: The $[Cp^*Cp^{iP5}Dy]^+$ fragment (Center; C – grey, Dy – blue/green), representing the current state-of-the-art for single ion magnet design. (Left) Hysteretic behavior of the magnetization, showing large magnetic remanence at zero field and large coercive fields. (Right) Relaxation behavior, showing an extremely large barrier, relaxation to 10^4 seconds, and a persistent QTM region. Figure adapted with permission from Science[37] with permission from AAAS.

We must of course start with the current state-of-the-art for monometallic SMMs and the realization of this design strategy. The family of SMMs with the general formula $[Cp'_2Dy]^+$ has, at least until recently, stood as the bar to which molecular magnets are measured (Figure 1.10).[38] The cyclopentadienyl anion coordinates in an η-5 fashion, essentially acting as a nearly uniform planar electron density that caps the Dy^{3+} ion at the axial coordination sites. While early attempts were somewhat stymied by distortions in the geometry to allow coordination of residual solvent

or stray ions, the eventual use of bulky cyclopentadienyl derivatives enforced a nearly linear geometry upon the system.[37,39] Now, the Dy^{3+} ion was flanked by a nearly perfect axial coordination environment with minimal equatorial contributions to the crystal field. Consequently, the magnetic behavior of the system is remarkably robust. Coercivity can be observed up to liquid nitrogen temperatures, and U_{eff} is well above 1000 cm^{-1}. At low temperatures, relaxation times were above 10^4 s, but below 10 K this rate is limited by QTM.
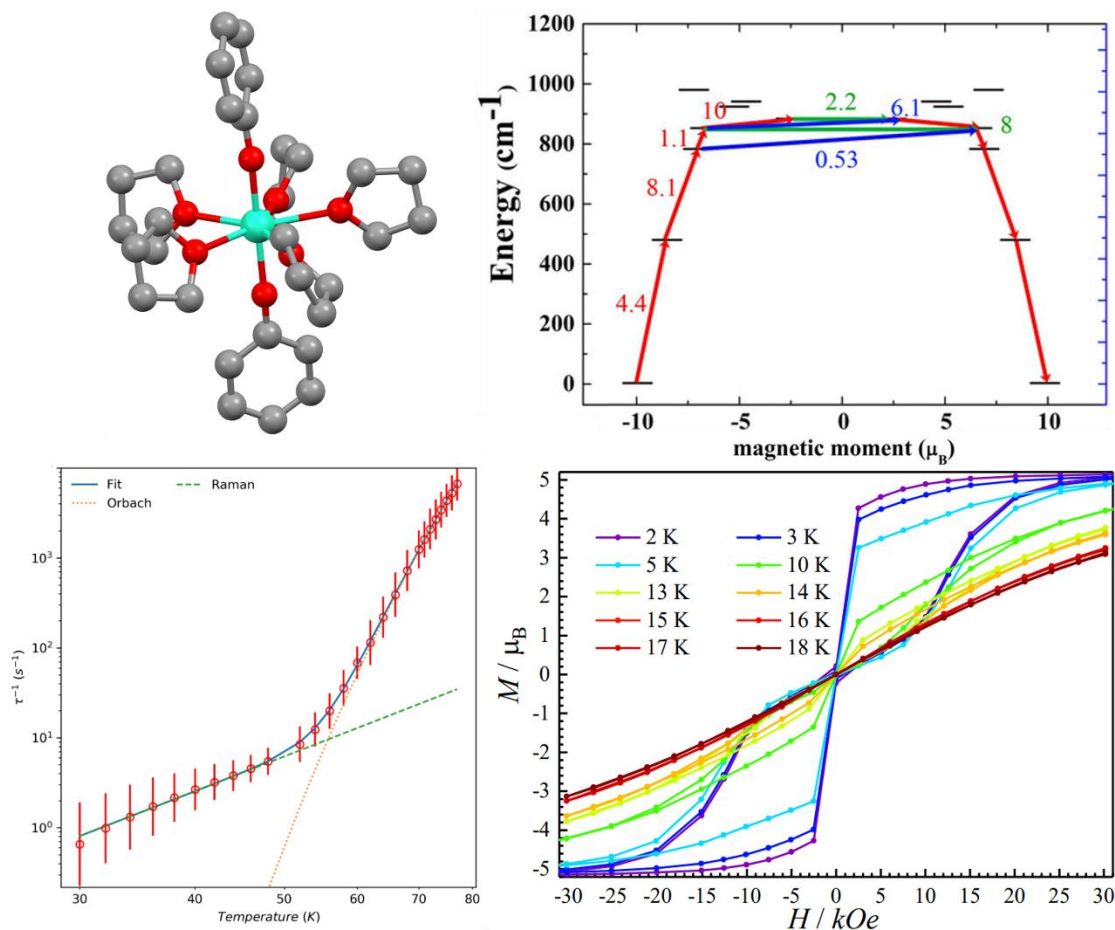
Figure 1.11: Representative structure for D_{5h}-symmetric bis(alkoxide)-dysprosium SIMs. (Top left) Fragment containing $[Dy(OPh)_2(THF)_5]^+$ (C – grey; O – red; Dy – blue/green) (Top right) Calculated magnetic energy landscape for Dy^{3+}; (Bottom left) Relaxation behavior plotted as τ^{-1} vs T; (Bottom right) Magnetic hysteresis measurements at a range of temperatures showing large remanence and waist-restricted coercivity. Adapted From Ding et al[40] with permission by Wiley publishing.

Relatively recently, a new family of Dy^{3+}-based SMMs has shown similarly robust SMM properties.[38,40–44] Complexes of the general formula $[L_5Dy(OR)_2]$, with L representing neutral L-

type ligands and OR representing various anionic alkoxides and siloxide ligands, displayed similarly high U_{eff} as in the dysprosocenium series (Figure 1.11). This might seem surprising at first, as while the near-linear coordination of the $^-$OR ligands should promote high magnetic anisotropy, the five equatorially coordinated solvent ligands would be expected to promote state mixing and undercut the barrier significantly. Hysteretic measurements confirm this to be true in ensemble behavior. All measured compounds with this motif displayed waist-restricted hysteresis with comparatively low coercivities (though they are still quite large among SMMs as a whole). Furthermore, it was noted that, for some species, the barriers were somewhat undercut by active Raman processes. This was more pronounced in compounds with flexible equatorially coordinated THF ligands than in those with rigid pyridine ligands, implying that the more dynamic crystal field environment facilitates faster relaxation behavior.

In contrast to Dy^{3+}, far fewer examples of high-performance SMMs exist for Er^{3+}. Following the same design philosophy described above, a perfectly equatorial field would be expected to promote magnetic anisotropy in these complexes. In a series of homoleptic C_3-symmetric Er^{3+} complexes, bulky trimethylsilyl- and aryl-functionalized groups were used to enforce a strict 3-coordinate structure.[45,46] Small distortions in the coordination plane were observed and used as a focus to describe the varying magnetic properties that were observed. In stark contrast to Dy^{3+}, all three of these complexes were found to have U_{eff} below 100 cm^{-1}. This was attributed to distortions in the equatorial plane promoting mixing between low-lying M_J states making QTM more facile. However, this remained a trend for Er^{3+}-based SIMs. In a thorough computational study by Zhang et al,[47] the energy gap between the ground and first excited states was found to be limited to below ~212 cm^{-1}. This is far lower than the typical inter-KD separation for Dy^{3+}, but since the first excited state can also be the potentially anisotropic $M_J = 13/2$ state, this

would not in and of itself promote fast relaxation. In fact, most high-performance Dy^{3+} SMMs have relaxation processes that can proceed through the second excited state or beyond. Thus, the real limitation of Er^{3+} systems is the spin-orbit and crystal field perturbations being more similar in scale. In the systems surveyed, the strong crystal fields employed promoted mixing within the first excited state, increasing the transverse moment and accelerating QTM processes. Furthermore, in many other systems, the low-moment $M_J = \frac{1}{2}$ doublet looms close to the ground state, often providing an upper limit on the barrier as the second or even first excited state. Such a discrepancy reveals the caution necessary when employing the simplified design principles outlined above. Unlike Dy^{3+}, which follows a smooth progression from oblate electron density to prolate electron density as the moment of the spin-orbit state decreases, the corresponding doublets in Er^{3+} follow the opposite trend less closely. Such a progression of charge density shapes from approximately prolate to approximately oblate invites a more robust synthetic description to stabilize anisotropy. For the sake of simplicity in this discussion, however, the approximation of the optimal coordination environment will be taken as a valid assumption.
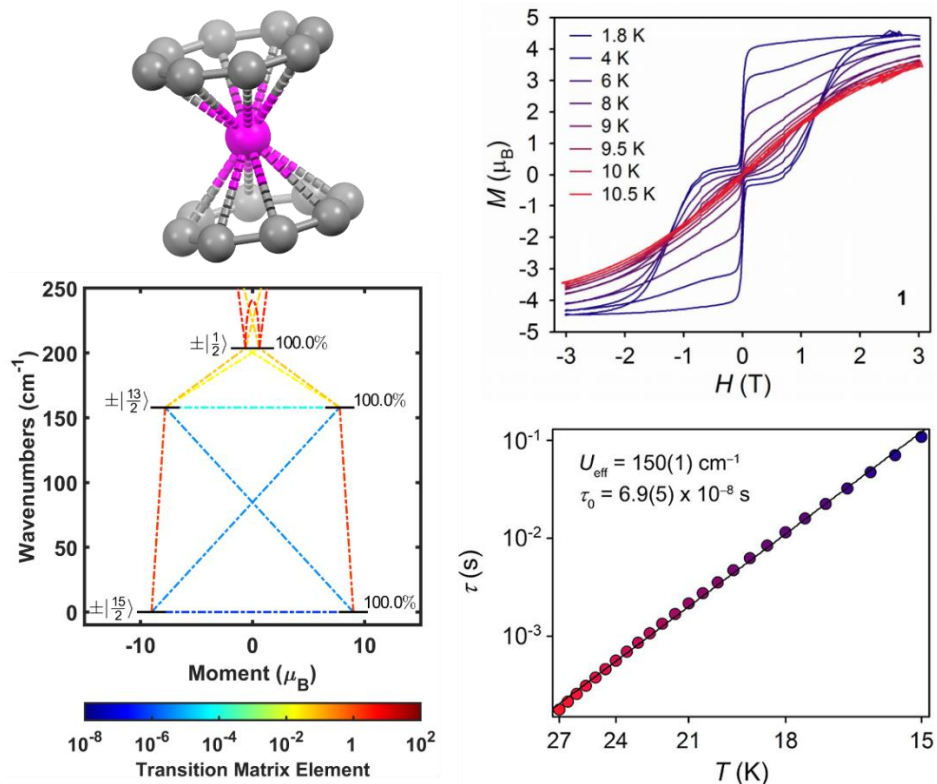
Figure 1.12: The $[ErCOT_2]^-$ fragment (Upper left); C – grey, Er – pink), representing the state-of-the-art for Er-based SIMs. (Bottom Left) Calculated single-ion Kramers doublets for the $[ErCOT_2]^-$ fragment, with largest m_J state contributions labeled and transition matrix elements between states color coded on a logarithmic scale (Upper Right) Hysteretic behavior of the magnetization, showing large magnetic remanence and waist-restricted coercivity, attributed to a magnetic avalanche induced by dipolar fields produced by neighboring spins. (Bottom Right) Relaxation behavior, focusing on the Orbach regime where relaxation is predicted to occur via the second excited Kramers doublet. Figure adapted with permission from Meihaus et al.[48] Copyright 2013 American Chemical Society

The supposed inability for Er^{3+} SIMs to be designed as cleanly those with Dy^{3+} may have been a death knell were it not for a rather unique class of Er^{3+} structures. In probing a series of asymmetric lanthanide sandwich compounds bearing cyclopentadienyl and the dianionic cyclooctatetraene ligand (COT^{2-}), single-molecule magnetic behavior was surprisingly absent for the Dy^{3+} congener and robust for Er^{3+}.[49,50] This behavior was found to be consistent across several other ErCOT (shorthand for Er^{3+} bound to a COT^{2-} derivative) complexes,[51–55] and soon the family of $[ErCOT_2]^-$ complexes represented the longest zero-field relaxation and highest coercivity among Er^{3+}-based SIMs with exceptionally pure m_J states (Figure 1.12).[48,56–60] This, initially, is unintuitive; why would an axially-coordinated planar COT^{2-} ligand stabilize anisotropy in a

prolate ion? In practice, the ~370 pm ring diameter provides a sufficiently large central pocket for the lanthanide ion to bind closely. Thus, in essence, the π-electron HOMO in COT^{2-} HOMO rises in a barrel-shaped charge density surrounding the Er^{3+} ion. This can be thought of in essence as an equatorial crystal field environment. Simultaneously, the tight binding environment causes the ring to sterically crowd any other ligands from binding within the same half of the coordination sphere, effectively protecting that half of the coordination sphere from adverse crystal field environments. However, the looming M_J = ½ state discussed earlier persists at approximately 200 cm^{-1}, effectively locking thermal relaxation to within this region.[47] Within the $[ErCOT_2]^-$ series, this is further limited to within the first excited state at approximately 150 cm^{-1}, which is still highly anisotropic. I will briefly draw attention again to the ability of the COT^{2-} ligand to stabilize anisotropy in the presence of an axially coordinated ligand such as cyclopentadiene. This is attributed to the dianionic, tightly bound electron density overpowering the effect of any neutral or monoanionic ligands within the rest of the coordination sphere. We will discuss this in further depth in the following section.

1.6 Coupling, the Bottom-Up Approach, and Outlook

The inevitable barrier to useful application is scalability and control in a system. For molecular magnets to be a viable technology, spins must be able to be read, written, and/or stored; such application requires controllable magnetic coupling within the system.[30,61–63] Furthermore, coupling is expected to enhance relaxation behavior by drastically decreasing the transition probability connecting states with opposite moments within the ferromagnetically and antiferromagnetically coupled energy levels.[4,7] This poses a serious challenge for lanthanide-based spin systems. The highly contracted nature of the 4f subshell here is revealed to be a double-edged sword. While protection from the majority of the ligand field environment helps enforce

22

anisotropy, it also shields the system from meaningfully coupling to neighboring spins via orbitally-promoted exchange mechanisms. Transition metals can communicate their spin state via spin polarization of a bridging ligand's orbitals due to good overlap, but lanthanides have orbital overlap on the order of 2%.[6] Thus, outside of secondary mechanisms like $4f$-$5d$ mixing, diamagnetic bridges are generally a poor mechanism of introducing coupling to a multinuclear lanthanide system.

One solution to such a challenge is to employ bridging ligands bearing an unpaired electron. Radical-bearing ligands, either conjugated π-electron systems or small radical bridges stabilized by the lanthanide metals, can penetrate deeper into the $4f$ subshell and promote coupling via a mutual interaction with the ligand rather than relying on significant direct communication between the metal centers.[7] Such complexes bear impressively large derived coupling constants above 10 cm^{-1}, and open coercive hysteresis can be observed for many Dy^{3+}- and Tb^{3+}-derived radically-bridged SMMs. Additionally, the current state-of-the-art in coupled systems lies with a reduced linear Dy$_2$ complex with an electron trapped within the overlapping $5d_{z2}$ orbitals which displays unmeasurably large coercivity at even 60 K.[64] However, such a design approach comes with its own challenges. The highly penetrating radical ligand orbitals imply that the description of the crystal field as an effective perturbation on the spin-orbit coupled states is no longer valid. Furthermore, many current examples consist of two lanthanide subunits optimized for single-ion behavior, such as [Cp*$_2$Dy]$^+$ fragments, connected by an equatorially-bound radical bridging ligand.[65–70] In these structures, the electron density of the radical ligand acts to essentially destroy the anisotropy that was so carefully designed into the lanthanide subunits. This can be observed in the substantially lowered barriers in many such examples, emblematic of increased mixing within the excited states. This also follows from the last main challenge introduced by strong coupling;

while strong coupling is desired to effectively quench QTM processes, such large perturbations cause significant mixing between magnetic states that are close in energy as coupling approaches the same magnitude as the crystal field splitting. Thus, while radical ligands present an exciting avenue toward realizing operant SMMs, informing their design requires more thorough investigation and refinement of synthetic principles.

Another intriguing approach toward extending to larger systems and more robust magnetism is a bottom-up approach to design.[28,56,71,72] In such an approach, a magnetic subunit with an unsaturated coordination sphere is used as a building block of sorts. This subunit should represent a dependable source of anisotropy that is robust in the face of the crystal field environment imposed by other ligands. This would allow for the rational extension of a single unit into polynuclear clusters and extended materials through careful choice in bridging ligands. However, such a subunit seems elusive. Most SIMs we have discussed thus far have their anisotropy severely affected or destroyed upon coordination of a bridging ligand, such as with $[Cp'_2Dy]^+$, or have their coordination spheres entirely saturated, such as with $[ErCOT_2]^-$. Ideally, such a unit would bear a tricationic lanthanide with a directing ligand that could stabilize anisotropy whilst preserving the rest of the coordination sphere for synthetic modification.

From our previous discussions, we can identify one such candidate in the $[ErCOT]^+$ subunit. The COT^{2-} ligand can stabilize SIM behavior despite the presence of an axially coordinated ligand. As we previously saw, the highly charge-dense dianion and barrel-shaped pi-electron density promotes anisotropy more so than other coordinated ligands. Thus, this subunit seems ideal as a magnetic fragment with conserved anisotropy and synthetic tunability. To better support this approach and confirm the ability of COT^{2-} to direct anisotropy in Er^{3+}, we isolated a series of half-sandwich complexes of the general formula $Er(COT)(I)(L)_2$, where L included

tetrahydrofuran (THF), pyridine (py), and acetonitrile (ACN).[73] All complexes in the series had well-isolated pure ground states, predominantly $M_J = 13/2$ excited states, and barriers above 90 cm^{-1}. Furthermore, we also demonstrated that a chloride-bridged dinuclear complex bearing ErCOT subunits displayed ferromagnetic coupling, maintained its magnetic anisotropy, and had suppressed QTM.[74] This confirmed for us that the ErCOT motif seemed to be an ideal candidate for developing a bottom-up approach to molecular magnets.

The other main challenge of the building block approach to increase dimensionality is the introduction of a coupling perturbation significant enough to effectively quench QTM pathways that undercut magnetic relaxation without fundamentally destroying the anisotropy we have carefully cultivated with significant M_J mixing. Whilst orbital exchange mechanisms can effectively remove QTM as a viable pathway entirely, they are difficult to implement due to the extreme charge densities and unpredictable coupling strength as discussed above. A different approach, then, relies on the use of weaker coupling interactions that fulfil two criteria. First, the energy perturbation introduced by this coupling should be fairly small so as to minimize mixing of the input single-ion levels. Second, the composition and anisotropy of the output coupled states should be synthetically directable using synthetically implemented structural design criteria. This invites the use of a much smaller and easily controlled mechanism – the dipolar interaction.[7,4,3] This equation can be approximately expressed in its classical form:

$$E_{dip} = \frac{\mu_0}{r^3}\left(\mu_1 \cdot \mu_2 - 3\frac{(\mu_1 \cdot \vec{r})(\mu_2 \cdot \vec{r})}{r^2}\right) \text{ Equation 1.7}$$

where μ_i represents the moment vector of the individual metal centers, $\vec{r}$ is the internuclear vector with length r, and μ_0 is the permittivity of free space. This classical approximation is appropriate, as the highly anisotropic nature of the $M_J = 15/2$ and $M_J = 13/2$ spin-orbit microstates allow them to be treated as magnetic point dipoles. Such an interaction is usually on the order of ~1 cm^{-1},

which is approximately one to two orders of magnitude smaller than the inter-Kramers doublet energy separation. Thus, this small perturbation avoids the significant state mixing that is often present in other coupling mechanisms.

As for the second criterion – the ability to easily control states via the coupling mechanism – dipolar coupling is again ideally poised to fulfill this role. Rather than as a dot product, let us rewrite the dipolar equation in terms of structural parameters:

$$E_{dip} = \frac{|\mu_1||\mu_2|\mu_0}{r^3}\left(3\cos(\theta_1)\cos(\theta_2) - \cos(\Delta\theta)\right) \qquad \text{Equation 1.8}$$

Here, μ_i is the magnitude of the magnetic moment for center i, and θ_1, θ_2, and $\Delta\theta$ represent the angles between the moment on center i and the internuclear vector and the angle between the two moments, respectively. Now it is apparent that, if the anisotropy axis is able to be predictably directed within the structure, the dipolar interaction can be very finely controlled by varying only two parameters – the distance between metal centers and the orientation of their moments. Here, again, the ErCOT unit is an ideal choice. In addition to stabilizing the pure $M_J = 15/2$ ground state, the COT^{2-} ligand consistently pins the magnetic anisotropy axis to lie along the vector connecting the Er^{3+} ion to the COT^{2-} ring centroid ($\vec{r}_{ErCOT}$). The other half of the coordination sphere is available to install bridging or scaffolding ligands to direct $\vec{r}_{ErCOT}$.
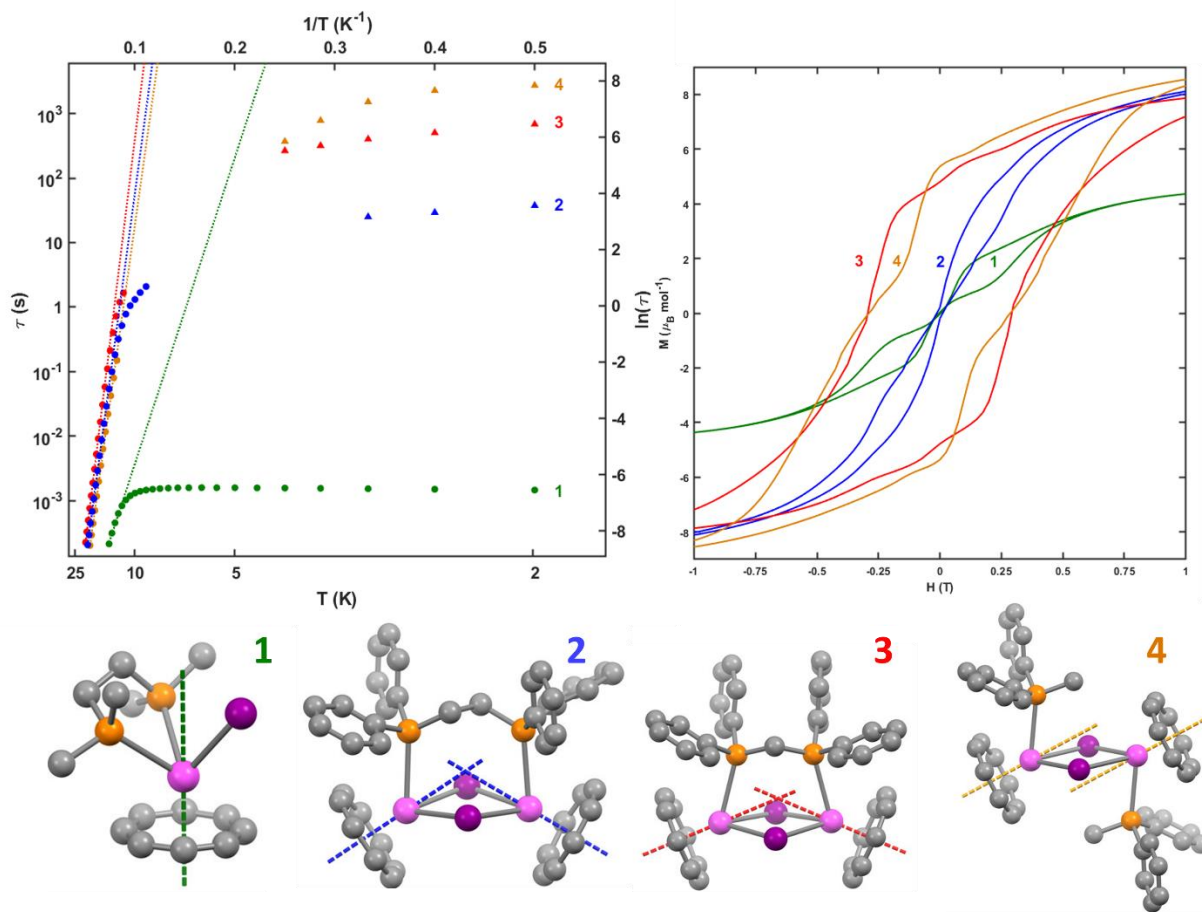
Figure 1.13: AC susceptibility and magnetic hysteresis measurements for a series of phosphine-scaffolded ErCOT dinuclear SMMs. The introduction of coupling is observed to lengthen relaxation by four orders of magnitude, and moving from an orthogonal to a parallel arrangement of anisotropy axes lengthens relaxation by another hundredfold, yielding a total millionfold increase in relaxation time. Figure adapted with permission from Hilgar et al.[75] Copyright 2019 American Chemical Society

Even control over such a small energy regime can yield dramatic changes in magnetic behavior. As a proof of concept, a series of phosphine-ligated ErCOT(I) complexes was synthesized wherein one complex was mononuclear, and the remaining three dinuclear complexes had their bridging angle varied between near orthogonality and parallel alignment by modifying the scaffolding phosphine (Figure 1.13).[75] In their low temperature regime, zero-field ac relaxation and dc magnetization decay experiments revealed a clear temperature dependence for τ even down to 2 K – the lowest temperature relaxation data could be reasonable measured. This represented a decrease of four orders of magnitude from the mononuclear complex to the fastest relaxing

dinuclear complex, and the rate slowed an additional two orders of magnitude to the inversion symmetric complex. Its 2520 s relaxation time is among the longest measured for an Er^{3+} SMM. Thus, control over this small perturbation can lead to dramatic changes in magnetic properties of interest, as will be discussed throughout the rest of this body of work.

Within the body of this dissertation, I will describe the advances we have managed to make in designing dipolar coupled ErCOT systems and the fine level of control we are able to exert on the magnetic landscape. From this position, however, there is still incredible potential for growth in the field of molecular magnetism. Beyond further refinement of the synthetic guidelines we will explore, many other approaches are still rapidly developing. Radical coupling still holds great promise, new frontiers are being opened in transition metal molecular magnetism, and forays into crystal engineering to control bulk magnetic properties are just some of the myriad directions into which the young field is expanding. Even within intramolecular dipolar coupling, a relatively specific focus, there is much space for growth in modeling interactions beyond the ground state, optimization of the interaction, exploration on the effect of state mixing on the dipolar interaction, and myriad other directions. Herein, though, we take some early steps in establishing synthetic guidelines toward implementing the dipolar interaction for fine magnetic control. In Chapter 2, I explore the balance between the balance of stronger coupling with increased state mixing when using charge-dense $2p$ bridging alkoxide ligands from the perspective of single-ion states. In Chapter 3, we explore this concept further using the higher symmetry methyl anion as a bridge. Through use of various numbers of bridging ligands, the bonding angle was able to be optimized in addition to the effect of the ligand identity on the internuclear distance. Finally, in Chapter 4, we explore the energy landscape of a series of halide bridged $Er^{TMS}COT$ complexes ($^{TMS}COT =$ 1,4-bis(trimethylsilyl)cyclooctatetraene) to determine the origin of dramatically different

relaxation behaviors by taking into consideration interactions between ground states and excited

states as simplified perturbations that do not mutually mix.

2.1 Introduction

The design of discrete molecules exhibiting superparamagnetic relaxation behavior has accelerated over the past two decades.[76,77] Instead of a classical rotation of a magnetization vector traversing an energy barrier, magnetic relaxation in these single-molecule magnets (SMMs) is best described by transition probabilities between quantized states with different orientations of the molecular electron angular momentum. The energies and transition probabilities of these states are controlled by the ligand field interaction, allowing for the development of synthetic design principles toward the optimization of these properties on a molecular level. Such methods have been successfully applied to design transition metal[71,78,79] and lanthanide[26,27,80,81] based SMMs. Lanthanide-based SMMs, in particular, offer highly anisotropic spin-orbit coupled ground states with large moments that can be stabilized by enforcing a particular crystal field environment.[82,83] Adherence to these principles has yielded extraordinary results that outperform other SMMs in their single-ion anisotropy.[37,84,85]

To expand diversity and introduce collective behavior to SMMs, considerable current work is focused on synthesizing well-coupled molecular magnetic systems. This coupling can curtail the low-temperature quantum tunneling of the magnetization (QTM) mechanism of magnetic relaxation by increasing the total effective moment of the ground state in a molecular magnetic system. However, coupling in SMMs has proven incompatible with the retention of magnetic anisotropy, largely because both phenomena are generally facilitated by the same orbitals. It is difficult to construct a ligand scaffold that introduces coupling without disturbing the crystal field environment responsible for generating single-ion anisotropy within individual magnetic centers.

To add further synthetic complexity, the molecular scaffold must orient the individual ions'
anisotropy axes such that the net effect is non-zero and axial. While current research in using well-
oriented diamagnetic bridges[86] and radical-based bridging ligands[65,87–90] in lanthanide systems has
demonstrated that weak coupling need not be a limiting factor for multinuclear magnets, a unified
set of synthetic design principles accounting for both coupling and anisotropy remain a collective
challenge for the field.

One approach to directly targeting well-coupled multinuclear magnetic clusters and
materials is through the bottom-up assembly of highly anisotropic synthetic building blocks.[71,72,91]
Ideally, by incorporating metal centers with large inherent single-ion anisotropy into larger
molecular frameworks, anisotropy in the resultant material would be conserved and enhanced *via*
suitably strong ferromagnetic coupling. Inspired by examples of robust anisotropy in Er^{3+}
stabilized by the strong equatorial crystal field provided by the cyclooctatetraenide dianion
(COT^{2-}) described over the last decade,[48,50,54,57–59,72,91–93] we have displayed the conserved
anisotropy of Er^{3+} coordinated to a single COT^{2-} ligand.[73] We employed the resultant Metal-
Ligand-Pair Anisotropy (MLPA) to measure the effect of anisotropy axis collinearity on magnetic
relaxation inhibition.[75] Herein we enact a more drastic modification by introducing strongly Lewis
basic alkoxide bridging ligands. While the changes to the electronic structure are dramatic and
complex, we can interpret them in terms of perturbations from the known electronic structure of
the individual units and from the observed properties of our previously described $Er(COT)I(THF)_2$
and $[Er(COT)I(MDPP)]_2$.

Magnetic analyses are presented here for a centrosymmetric and non-centrosymmetric
dinuclear Er^{3+} system bridged by simple alkoxide ligands. As they commonly form multitopic
bridging interactions stabilized by charge and hard Lewis acid/base interactions, the library of

multinuclear alkoxide-bridged lanthanide systems with known magnetic properties is rich.[94–103] However, most of these systems exhibit poor relaxation dynamics and often have negligible axial anisotropy, either due to strong mixing of the ground spin-orbit coupled states or the weak exchange coupling provided by the alkoxide ligands. Some systems have overcome this by using scaffolds to enforce alignment of the principle anisotropic axes to promote ferromagnetic dinuclear coupling.[104] Here we observed consequential perturbations by hard Lewis basic alkoxide ligands to the anisotropy in two dinuclear Er^{3+} species. Despite observed ferromagnetic coupling, fast through-barrier relaxation mechanisms are still operant, limiting long-timescale relaxation.

2.2 General Methods and Procedures

Physical Measurements

Single crystal X-ray data were collected at 100 K on a Bruker κ Diffractometer with a Mo Kα radiation source and an Apex II Area Detector. The structures were solved using direct methods via the SHELXT routine and refined using full-matrix least-squares procedures with the SHELXL[105] routine. Olex2 was used as a graphical front-end.[106] Hydrogens were modelled using a riding model for all positions. Magnetic analyses were conducted with a Quantum Design MPMS3 SQUID Magnetometer running in DC scan mode. All samples were loaded in custom quartz tubes (D & G Glassblowing Inc.) and sealed under static vacuum. Eicosane wax was added to each sample. After sealing, the eicosane was melted to minimize torqueing and ensure good thermal conductivity during measurements. All static susceptibility data were corrected for diamagnetic contributions from eicosane and the samples themselves using Pascal's constants.[107] DC susceptibility measurements were collected with $H_{DC} = 1000$ Oe. Isothermal magnetization data was collected at a sweep rate of $H_{dc} = 30$ Oe/s. AC susceptibility studies for both compounds were conducted between 1–1000 Hz ($H_{dc} = 0$ Oe, $H_{AC} = 2$ Oe). Optimized DC fields for AC

susceptibility studies under an applied field were found by finding the field under which the complex exhibited the maximum relaxation time at a given temperature. AC susceptibility studies were then conducted between 1-1000 Hz (H_{dc} varies, H_{AC} = 2-8 Oe).

Experimental Procedure

All manipulations were carried out under anaerobic, anhydrous conditions under an atmosphere of nitrogen gas using standard Schlenk line and glovebox techniques. Pentane and tetrahydrofuran (THF) were dried on activated alumina columns and stored over a 1:1 mixture of 3 and 4 Å molecular sieves for at least two days before use. ErI_3 powder was purchased from Alfa Aesar and Strem Chemicals and potassium *tert*-butoxide, potassium ethoxide, and cyclooctatetraene (COT) were purchased from Aldrich; all were used as received. Dipotassium cyclooctatetraenide[48] and (η^8-cyclooctatetraenyl)-iodo-bis-tetrahydrofuran-erbium[73] were prepared via previously reported methods. Elemental analyses were conducted by Midwest Microlab, Indianapolis, IN.

Synthesis of [Er(COT)(OEt)(THF)]$_2$ (**1**)

A solution of ErCOTI(THF)$_2$ (293.5 mg, 0.5410 mmol) in THF was added to a mixture of KOEt (46.3 mg, 0.550 mmol) at room temperature and stirred overnight. The resulting peach suspension was centrifuged at 3000 rpm for 10 min. and the mother liquor separated. The peach solution was dried *in vacuo*; the pinkish-peach solids were re-dissolved in THF at 50 ˚C to form an orange-pink solution that was then centrifuged to remove residual solids. Crystallographically-uniform Pink hexagonal blocks were grown at −50 ˚C. Yield: 95.1 mg, 44.8%. CHN analysis (calc., found) for $Er_2O_4C_{28}H_{42}$: (43.25, 42.30); H (5.45, 5.26); N (0.00, 0.00).

Synthesis of [Er(COT)]$_2$(μ-O^{t}Bu)$_2$(THF) (**2**)

A solution of ErCOTI(THF)$_2$ (215.0 mg, 0.3963 mmol) in THF was added to a mixture of KO^{t}Bu (44.47 mg, 0.3963 mmol) at room temperature and stirred overnight. The resulting light pink suspension was centrifuged at 3000 rpm for 10 min. and the mother liquor separated. The pink-peach solution was dried *in vacuo*; the pink-peach solids were re-dissolved in THF and centrifuged. Crystallographically-uniform pink rectangular blocks were grown at ambient temperature by diffusion of pentane into THF. Yield: 111.6 mg, 74.0%. CHN analysis (calc., found) for Er$_2$O$_3$C$_{28}$H$_{42}$: C (44.16, 43.97); H (5.56, 5.59); N (0.00, 0.00).

Computational Information

All calculations were performed using the SEWARD/RASSCF/RASSI/SINGLE_ANISO modules of MOLCAS 8.2. Input atom coordinates were taken from X-ray crystal structures and were not geometry optimized. Solvent molecules were not included in the calculations. Basis sets of the ANO-RCC type were used and the quality of the specific basis function was selected based on the proximity of the atom to the metal (**Er:** ANO-RCC-VTZP; **atoms bound to Er:** ANO-RCC-VDZP; **all other atoms:** ANO-RCC-VDZ). Two-electron integrals were Cholesky decomposed (10^{-6} cutoff) to speed up calculations and save disk space. A CAS(11,7) was selected for the complete active space self-consistent field (CASSCF) procedure and in this space we included 35 CI roots of spin multiplicity 4 and 112 CI roots of spin multiplicity 2. All RASSCF module output wavefunctions were used to compute the spin-orbit matrix elements by the RASSI module. The RASSI module output was directed to SINGLE_ANISO for magnetic properties calculations; outputs from SINGLE_ANISO were used as is. The POLY_ANISO module was run using input files extracted from SINGLE_ANISO.

2.3 Results and Discussion

Complexes **1** and **2** were synthesized using standard air- and water-free techniques by adding potassium ethoxide (KOEt) or potassium tert-butoxide (KOtBu), respectively, to [Er(COT)I(THF)2] in tetrahydrofuran (THF). After removing KI, complex **1** was crystallized from concentrated THF at −50 ˚C; complex **2** was crystallized via the slow diffusion of pentane into a concentrated THF solution at ambient temperature. No monomeric side products have been observed. Both compounds are thermodynamically stable at ambient temperatures under inert atmospheric conditions.

Solid state structures of **1** and **2** (Figure 2.1) were determined by single crystal X-ray crystallographic methods using a Mo K(α) source. Compound **1** crystallizes in the orthorhombic *P*bca space group, while compound **2** crystallizes in the orthorhombic *P*nma space group. An isomorphous structure to **1** exists for Nd,[108] while no structural analog exists for **2**.

Compound **1** has two THF-bound [Er(COT)]$^+$ units doubly bridged by μ_2-ethoxide ligands related by a crystallographically imposed inversion center. Previous investigations into the magnetism of [Er(COT)]$^+$ complexes have identified the axis containing the Er^{3+} ion and the COT^{2-} centroid ($\vec{r}_{ErCOT}$) to correlate closely to the magnetic anisotropy,[73] making it a useful crystallographic parameter to describe the crystal field environment. The COT^{2-} ligand is bound relatively far from the Er^{3+} ion at $|\vec{r}_{ErCOT,\mathbf{1}}|$ = 1.82 Å, which is expected to weaken its ability to stabilize single-ion anisotropy of Er^{3+}.[109] To describe the axial or equatorial coordination of each non-COT ligand, coordination angles with respect to $\vec{r}_{ErCOT}$, defined as φ_{ligand}, were measured. In **1**, ligands are all bound above the magic angle, with φ_{OEt} = 43.45˚ and 45.56˚ and φ_{THF} = 54.71˚, suggesting a net destabilization of the $m_J = \pm15/2$ doublet.[27,82] The distance between Er^{3+} centers ($|\vec{r}_{Er-Er\prime}|$), 3.543 Å, is shorter than observed in iodide-bridged dinuclear [Er(COT)]$^+$ systems. As

dipolar coupling strength scales proportional to $1/_{r^3}$, we expect a stronger ferromagnetic dipolar interaction between $[Er(COT)]^+$ units. The angle between $\vec{r}_{ErCOT}$ and the Er–Er′ internuclear vector ($\vec{r}_{Er-Er'}$) was found to be $\theta_{ErCOT,1-r} = 26.01°$ and is equivalent by symmetry for each erbium center.

Table 2.1: Selected crystallographic and magnetic parameters from **1**, **2**, and previously described $[Er(COT)]^+$ species.

	Er-1	**Er-2a**	**Er-2b**	**Er(COT)I-THF₂**	**[Er(COT)I-(MDPP)]₂**
ΔKD_{1-0}	53.7 cm^{-1}	48.6 cm^{-1}	34.5 cm^{-1}	99.8 cm^{-1}	96.4 cm^{-1}
g_x	0.0289	0.239	0.0033	0.007	0.0006
g_y	0.0834	0.1184	0.2678	0.011	0.0009
g_z	17.4396	17.2907	17.093	17.82	17.9051
θ_{cant}	2.60°	3.81°	9.46°	1.49°	1.48°
θ_{gz-r}	29.42°	57.74°	13.21°	–	25.99°
$\theta_{gz-gz'}$	180°	109.1°	109.1°	–	180°
r_{ErCOT}	1.82 Å	1.84 Å	1.79 Å	1.77 Å	1.745 Å
Φ_{OR}	43.45°	49.04°	37.19°	49.71° (I)	46.62° (I)
$\Phi_{OR'}$	45.56°	49.04°	37.19°	55.00° (THF)	47.21° (I)
Φ_{SOLV}	54.71° (THF)	50.00° (THF)	–	48.64° (THF)	55.65° (MDPP)

Compound **2** has crystallographically imposed C_s symmetry and is comprised of two $[Er(COT)]^+$ units bridged by two μ_2-*tert*-butoxide ligands. Two distinct Er^{3+} coordination environments exist, Er-**2a** and Er-**2b**. Er-**2a** has $\varphi_{OtBu} = 49.04°$ and $\varphi_{THF} = 50.00°$ with $|\vec{r}_{ErCOT,2a}|$ = 1.84 Å, while Er-**2b** has $\varphi_{OtBu} = 37.19°$ with $|\vec{r}_{ErCOT,2b}|$ = 1.79 Å; both centers are expected to display relatively poor $m_J = 15/2$ stabilization due to their long $\vec{r}_{ErCOT}$ distances and off-equatorial alkoxide and THF binding motif. The Er^{3+} centers are significantly closer together in **2** than in **1** with $|\vec{r}_{Er-Er}|$ = 3.439 Å. The two independent $\vec{r}_{ErCOT}$ vectors are also positioned significantly differently, with $\theta_{ErCOT,2a-r} = 22.52°$, $\theta_{ErCOT,2b-r} = 53.81°$, and $\theta_{ErCOT-ErCOT} = 103.7°$.

From our previous work, we expect several of these structural parameters to be of great importance to the magnetic analysis; in particular, contrasting **1** and **2** to our previously studied dinuclear species containing the [Er(COT)]⁺ unit illustrates key differences. First, the relative $\vec{r}_{ErCOT}$ angle ($\theta_{\text{ErCOT-ErCOT}}$) shifts from parallel in **1** to nearly perpendicular in **2** (103.71˚). Our previous study on iodide-bridged materials found a marked slowing of the magnetization dynamics for more parallel angles, culminating in a 100-fold increase in the relaxation time at 2 K when changing the angle from 113˚ in [Er(COT)I]₂(DPPM) to 180˚ in [Er(COT)I(MDPP)]₂. Similar trends can be noted for $|\vec{r}_{Er-Er}|$ and $\theta_{\text{ErCOT-r}}$. The second factor of interest is of the coordination environment, specifically the hard, anionic alkoxides and $|\vec{r}_{ErCOT}|$. The [Er(COT)]⁺ unit has demonstrated stability of its single-ion anisotropy in low-symmetry environments with soft Lewis basic ligands, yet the alkoxides represent a significant, localized perturbation to the Er^{3+} free ion spin-orbit ground state. Thus, while in all previous [Er(COT)]⁺ structures φ_{ligand} has been smaller than the magic angle, the marked increase in Lewis basicity of the alkoxide ligands is expected to more drastically perturb the Er^{3+} $J = 15/2$ manifold than the weakly Lewis basic iodide ligand. Similarly, $|\vec{r}_{ErCOT}|$ is dramatically shorter at all Er^{3+} centers in **1** and **2** than in complexes we have previously described. We have justified [Er(COT)]⁺ as a suitable magnetic building block because a single COT^{2-} ligand can reliably stabilize the ground state anisotropy of Er^{3+}. This stabilization decreases as $|\vec{r}_{ErCOT}|$ increases;[109] as we have previously discussed; we therefore expect the single-ion anisotropy of **1** and **2** to weaken compared to our previously described complexes.
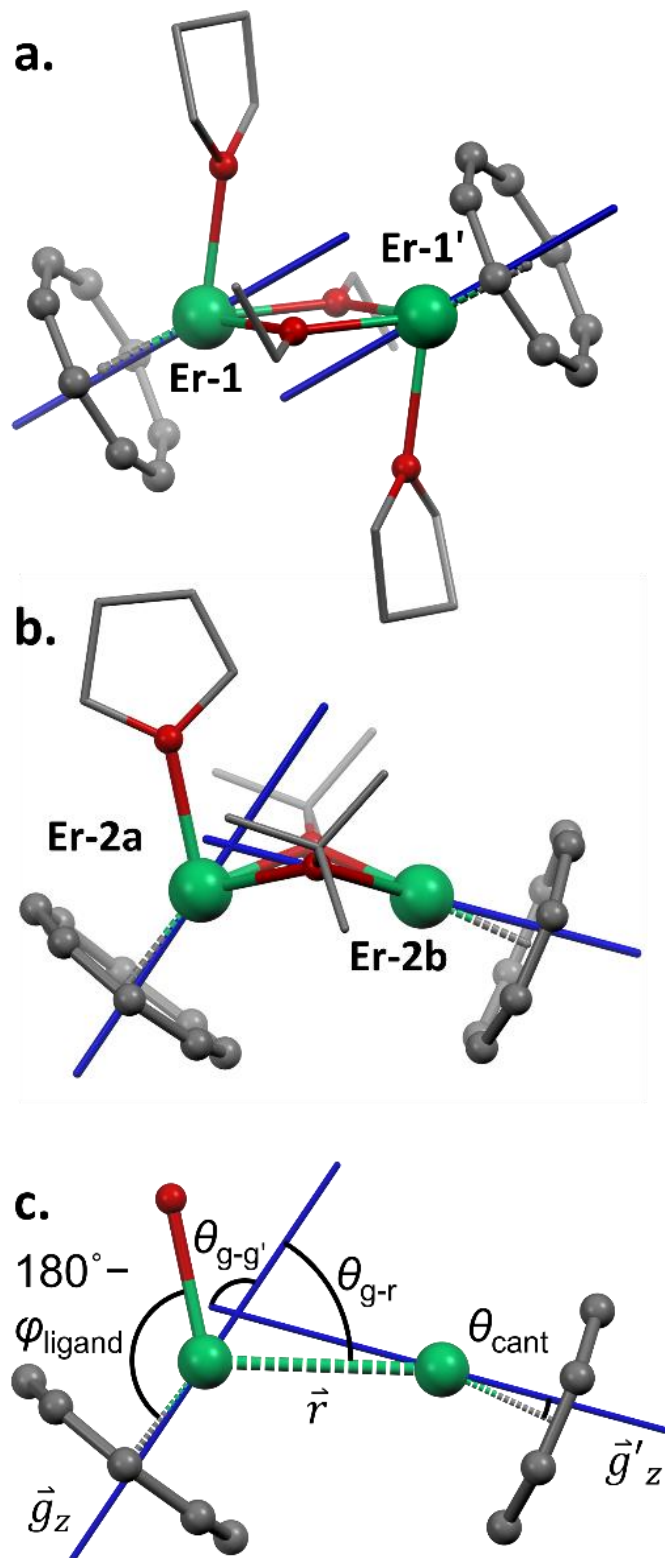
Figure 2.1: Solid-state structures for **1** (a) and **2** (b). Principle anisotropic axes (g_z) are shown in blue. Full structures for **1** and **2** have hydrogens omitted and non-COT carbons depicted as capped sticks for clarity. Angles and vectors are illustrated in the structure for **2**, omitting extraneous atoms for clarity (c).

We also wish to bring attention to the effect of steric bulk in anionic ligands on the coordination behavior of half-sandwich complexes. As observed with bridging halides, the small ethoxide ligand allows for the formation of an inversion symmetric dinuclear structure. With the increase in bulk in alkoxide bridges comes a large steric demand in the coordination environment. The steric crowding enforces a bent bridging motif, even preventing THF coordination on one Er^{3+} center. In an extreme case of steric bulk, Meng *et al* have used a terphenyl-oxide to isolate a mononuclear $[Er(COT)]^+$ structure.[110]

2.4 Computational Analysis of Magnetic Anisotropy

A series of ab initio calculations were performed to obtain insight into the crystal field perturbations on and differences between the single-ion magnetism of Er^{3+} in Er-**1**, Er-**2a**, and Er-**2b**. Electronic structures for **1** and **2** were modelled with the SINGLE_ANISO and POLY_ANISO modules in MOLCAS 8.2[111] using complete active space self-consistent field (CASSCF) techniques (Tables 2.1, 2.2). Input atom coordinates were taken from crystallographic data without further geometrical optimization. To investigate the single-ion anisotropy of the individual Er^{3+} center, each unique Er^{3+} ion was modelled as the lone magnetic ion by substituting the other erbium center with diamagnetic Y^{3+}, chosen for its similar ionic radius.

The alkoxide bridging motif in **1** and **2** show deviations from previously described $[Er(COT)]^+$ crystal fields in several notable ways. Each center still displays clear ground-state *g*-factor anisotropy, as expected for an Er^{3+} center bound to COT^{2-} ion; however, the transverse elements (g_x, g_y) for each center are larger than have been previously described, indicating the predicted weakened anisotropy. The first excited Kramers doublet (KD_1) for Er-**1**, **2a**, and **2b** lie 54, 49, and 35 cm^{-1} above the ground state (KD_0), respectively. These splitting are notably smaller than those calculated for previous halide-bound mononuclear and dinuclear $[Er(COT)]^+$ species

($U_{\text{eff}} > 90$ cm^{-1}), indicating that the alkoxides significantly destabilize the single-ion anisotropy in comparison. The barriers are consistent, however, with computed barriers for a recently reported mononuclear phenoxide-bound [Er(COT)]$^+$ complex ($\Delta KD_{1\text{-}0} = 55$ cm^{-1}).[110] The THF-complexed Er^{3+} centers (Er-**1** and Er-**2a**) display a larger $\Delta KD_{1\text{-}0}$ than Er-**2b**, though only on the order of 10 cm^{-1}. Angles between the principal anisotropy axis (g_z) and $\vec{r}_{ErCOT}$, θ_{cant}, have been calculated, and for all three unique Er^{3+} centers the magnetic axis retains a relationship with $\vec{r}_{ErCOT}$, though deviations are larger than previously observed. For comparatively soft Lewis-basic ligands, the COT^{2-} ligand overwhelmingly directs local anisotropy in Er^{3+} half-sandwich coordination environments by stabilizing the prolate high-moment ground spin-orbit state.[73,75] Er-**1** and Er-**2a** display deviations of $\theta_{\text{cant}} = 2.6°$ and $3.8°$, while Er-**2b** deviates significantly more with $\theta_{\text{cant}} = 9.5°$. This large θ_{cant} for Er-**2b** deviates more dramatically from $\vec{r}_{ErCOT}$ than any mononuclear or dinuclear [Er(COT)]$^+$ species we have previously reported, and those for Er-**1** and Er-**2a** are also comparatively large. Evidently, the [Er(COT)]$^+$ stabilization is heavily strained by the charge density distribution provided by alkoxide ligands at Er^{3+} centers with low symmetry.
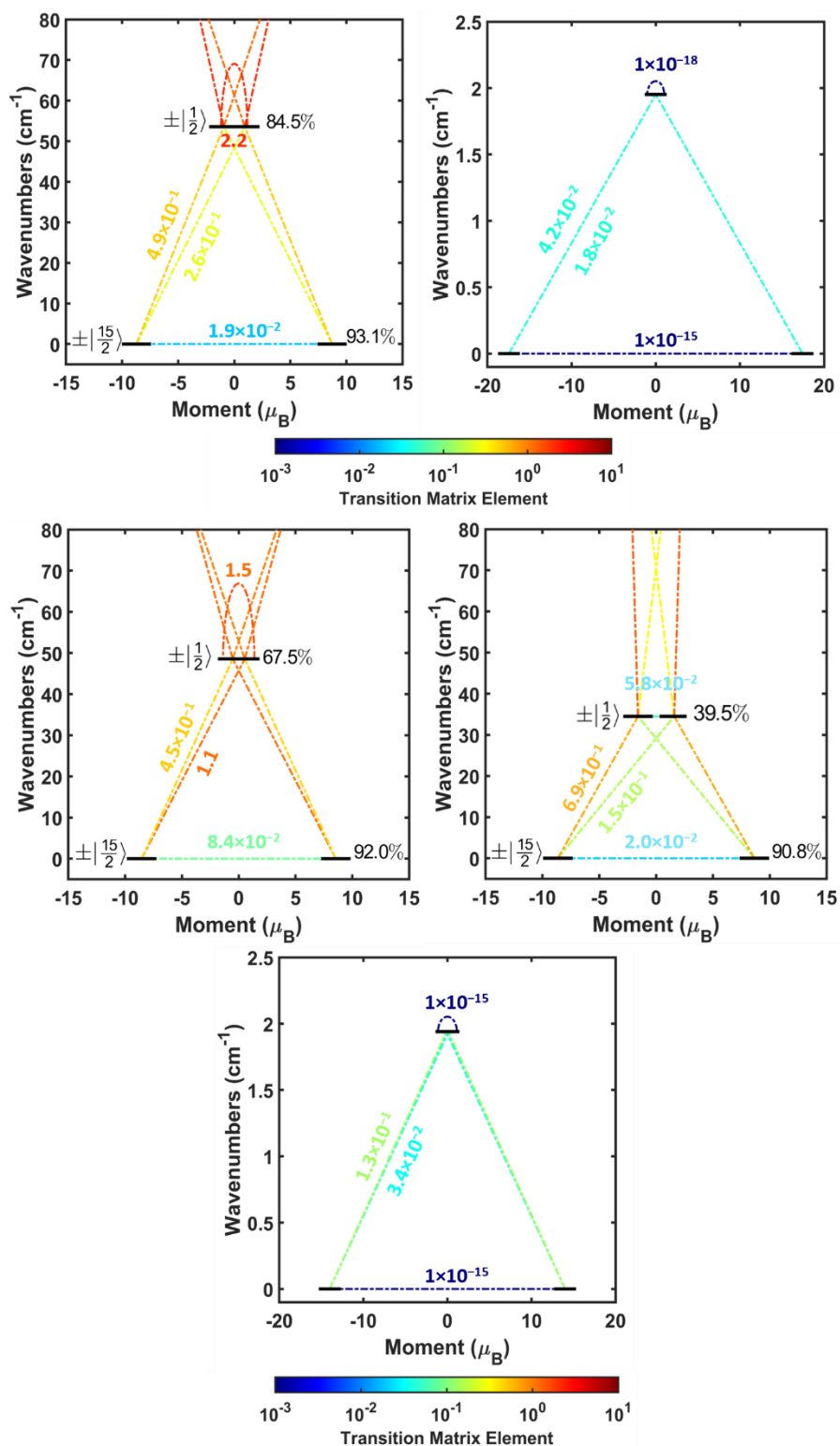
Figure 2.2: Ab initio calculated magnetic energies for **1** (top) and **2** (bottom). Only KD0 and KD1 are shown from SINGE_ANISO calculations (left for **1**, top for **2**). POLY_ANISO outputs include only contributions from KD0 for both complexes. Transition matrix elements are labeled and color-coded, and largest state contributions from SINGLE_ANISO are labeled.

41

Transverse matrix elements connecting the m_J states in the $J = 15/2$ manifold have been calculated and plotted for the lowest four m_J states manifold and the dipolar-coupled ground state (Figure 2.2). The magnitude of these elements are roughly proportional to their respective transition rates.[112] The rate of excitation to KD_1 is at least ten times faster than the through-barrier relaxation for all centers, indicating that the primary thermally-activated relaxation pathway will involve KD_1 in both **1** and **2**. While the ground spin-orbit states of all three centers display primarily $m_J = \pm 15/2$ character (93.1% Er-**1**, 92.0% Er-**2a**, 90.8% Er-**2b**), significant mixing with lower moment states is present. This justifies the relatively large matrix elements between them and indicates a large contribution of QTM mechanisms to relaxation dynamics in the uncoupled case. The first excited state also displays unfavorable mixing, with $m_J = \pm 1/2$ (84.5% Er-**1**, 67.5% Er-**2a**, 39.5% Er-**2b** being the primary contributor for each center. Consequently, matrix elements between the first excited states are on the same order of magnitude as those for excitation to the second excited state for all centers besides Er-**2b**, which displays the smallest degree of $m_J = \pm 1/2$ contribution to KD_1. The mixing of states in KD_0 is consistent with the non-optimal geometry of [Er(COT)]$^+$ half-sandwich complexes, though the degree of mixing in KD_0 and KD_1 is likely more pronounced due to the stronger crystal field perturbation afforded by the extremely charge-dense alkoxide ligands.

Lastly, the angle between g_z and $\vec{r}_{Er-Er\prime}$ ($\theta_{\text{g-r}}$) and the angle between principal anisotropy axes ($\theta_{\text{gz-gz}\prime}$) were determined as a comparison to the crystallographic parameters described above. For Er**1**, $\theta_{\text{g-r}} = 29.4°$ for both Er^{3+}, related by the crystallographic inversion center, and $\theta_{\text{gz-gz}\prime} = 180°$. The principle anisotropy axes are parallel, but noncolinear. These match well with other inversion symmetric [Er(COT)]$^+$ dinuclear structures we have investigated. Complex **2** deviates significantly from previously observed trends, with $\theta_{\text{g-r}} = 57.7°$ for Er-**2a** and $\theta_{\text{g-r}} = 13.21°$ for Er-

2b, and $\theta_{gz\text{-}gz'} = 109.1°$. The orientations of the anisotropy axes in **1** suggest that ferromagnetic dipolar interactions may be favorable, whereas in **2**, the angle between the anisotropy axes makes this far less likely.

Table 2.2: Energies and g-tensor components for doublets arising from dipolar-coupled ground states of **1** and **2**

	1	**2**
ΔE_{coup}	1.952 cm^{-1}	1.940 cm^{-1}
$g_{x,F}$	1×10^{-12}	1×10^{-12}
$g_{y,F}$	2.6×10^{-7}	1.8×10^{-9}
$g_{z,F}$	34.8776	28.0024
$g_{x,AF}$	3.8×10^{-12}	1×10^{-12}
$g_{y,AF}$	0	19.9474
$g_{z,AF}$	1×10^{-12}	2.4×10^{-7}

To model this coupling, outputs from SINGLE_ANISO were used as inputs for POLY_ANISO. For **1**, crystallographic symmetry allows the use of an inversion center to create a second magnetic center using the coordinates for the first; for **2**, the two unique centers were calculated and positioned using crystallographic coordinates. Only dipolar contributions were considered. For both complexes, this resulted in two sets of doublets corresponding to the ferromagnetic and antiferromagnetic arrangements of the anisotropy axes of the ground states described by SINGLE_ANISO (Figure 2.2). While both **1** and **2** have a ground and excited doublet corresponding to their ferromagnetic and antiferromagnetic arrangements, respectively, the makeup of these states differs considerably (Table). The ground state of **1** is predictably highly anisotropic, as the crystallographically enforced symmetry imparting a moment along the principal axis double that of the single-ion. Similarly, the cancellation of moments in the excited state leads to an essentially diamagnetic doublet. The severely canted axes in **2** contrarily lead to a ground state with a smaller moment than in **1** and an excited state with significant anisotropy nearly perpendicular to the principal axis in the ground state. The resulting transition matrix elements

reflect this somewhat. Excitation from the ferromagnetically coupled ground state to the antiferromagnetically coupled excited state is expected to be approximately three times faster in **2** than in **1**, while QTM is expected to be quenched in each. A major assumption of this description, however, is that KD_0 and KD_1 have a large enough energy separation and do not appreciably mix such that the dipolar coupling interaction can be treated as a perturbation only on KD_0. Lastly, the barrier is surprisingly almost identical between **1** and **2**. While the angle between anisotropy axes implies that dipolar coupling should be weaker in **2**. However, this can be accounted for by the closer distance between Er-**2a** and Er-**2b** relative to the internuclear distance in **1**.
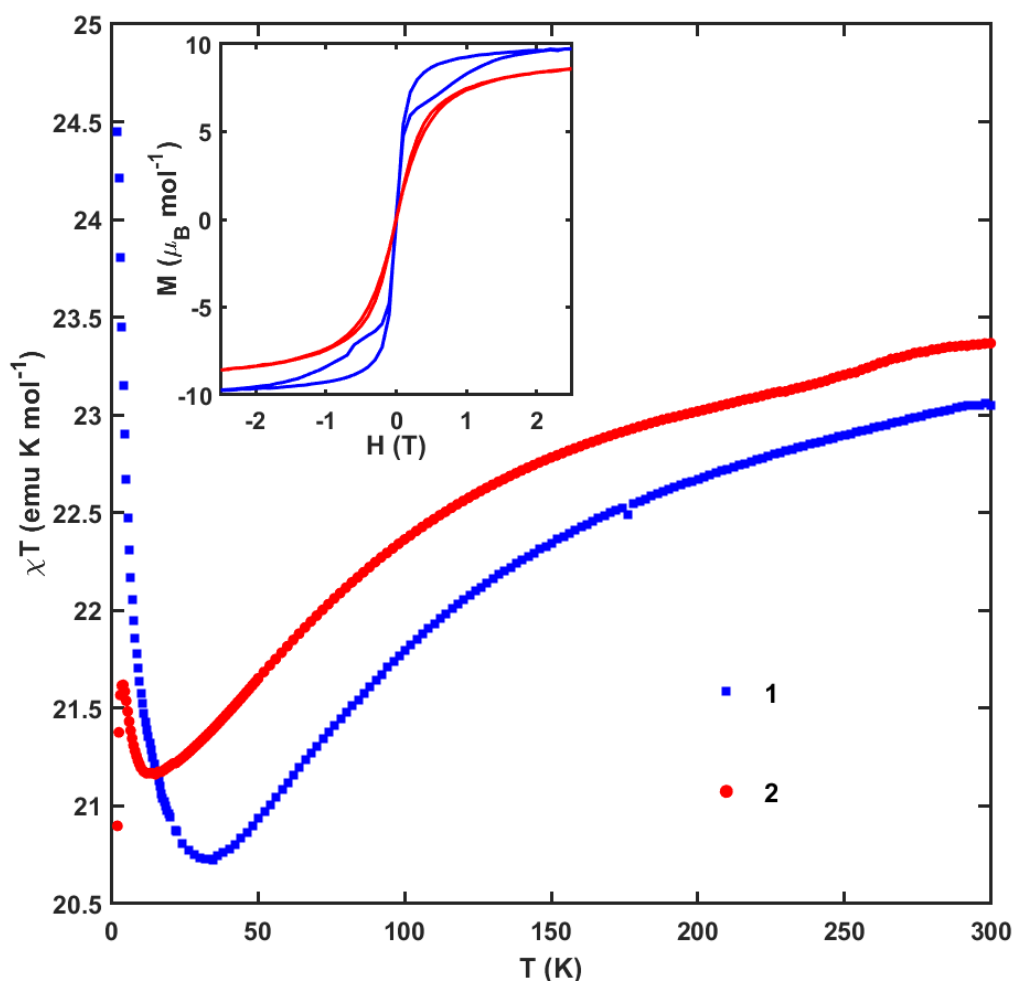
Figure 2.3: $\chi_M T$ vs. T measurements from 2 to 300 K for **1** (blue squares) and **2** (red circles). (Inset) Isothermal magnetization between -2.5 T and 2.5 T at 2 K for **1** (blue) and **2** (red)

2.5 Static Magnetic Properties

Zero-field cooled magnetic susceptibilities for each compound were collected between 2 and 300 K under a 1000 Oe applied field (Figure 2.3). At 300 K, experimental $\chi_M T$ values for **1** (23.05 cm^3 K mol$^-$1) and **2** (23.37 cm^3 K mol^{-1}) agree reasonably well with the theoretical value of 22.96 cm^3 K mol^{-1} for two uncoupled Er^{3+} ions ($J = 15/2$, $g = 6/5$). Upon cooling, both **1** and **2** display a steady decline in $\chi_M T$, consistent with higher energy m_J states becoming depopulated, before reaching minima of 20.73 cm^3 K mol^{-1} and 21.17 cm^3 K mol^{-1} at 34 K and 12 K respectively. Compound **1** then shows a sharp rise in $\chi_M T$ to 24.45 cm^3 K mol^{-1} at 2 K, while **2** undergoes a similar rise to 21.62 cm^3 K mol^{-1} at 4 K before dropping again to 20.90 cm^3 K mol^{-1} at 2 K. These sharp rises of $\chi_M T$ at low temperature indicate a predominantly ferromagnetic interaction between the Er^{3+} center in each molecule. While uncommon in lanthanide systems overall, this ferromagnetic interaction is consistent with the coupling observed in other [Er(COT)]$^+$ dinuclear magnetic molecules we have previously described.[74,75] Similarly, this coupling is more pronounced in **1**, which has its anisotropy axes oriented parallel to each other.

Isothermal magnetization studies were conducted between 2 and 300 K under DC fields within the range ±7 T. (Figure 2.3 inset, 30 Oe s^{-1}, VSM). At 2 K, both complexes show typical saturation behavior in the high-field limit for two Er^{3+} centers (M$_{sat}$ = 9.9 and 9.2 μ_B mol^{-1} for **1** and **2**, respectively). As the field is swept between 7 and −7 T, waist-restricted magnetic hysteresis is observed in both complexes, with neither showing any remnant magnetization on the timescale of this measurement. This "butterfly hysteresis" is commonly attributed to a QTM relaxation pathway, where transitions within the ground Kramers doublet are faster than the measurement timescale. This is consistent with most other mono- and dinuclear [Er(COT)]$^+$ species we have reported, and is indicative that the ferromagnetic coupling between the [Er(COT)]$^+$ units in both

complexes is too weak to totally suppress QTM relaxation pathways in Er^{3+} centers with significantly perturbed anisotropy.

2.6 Dynamic Magnetic Properties
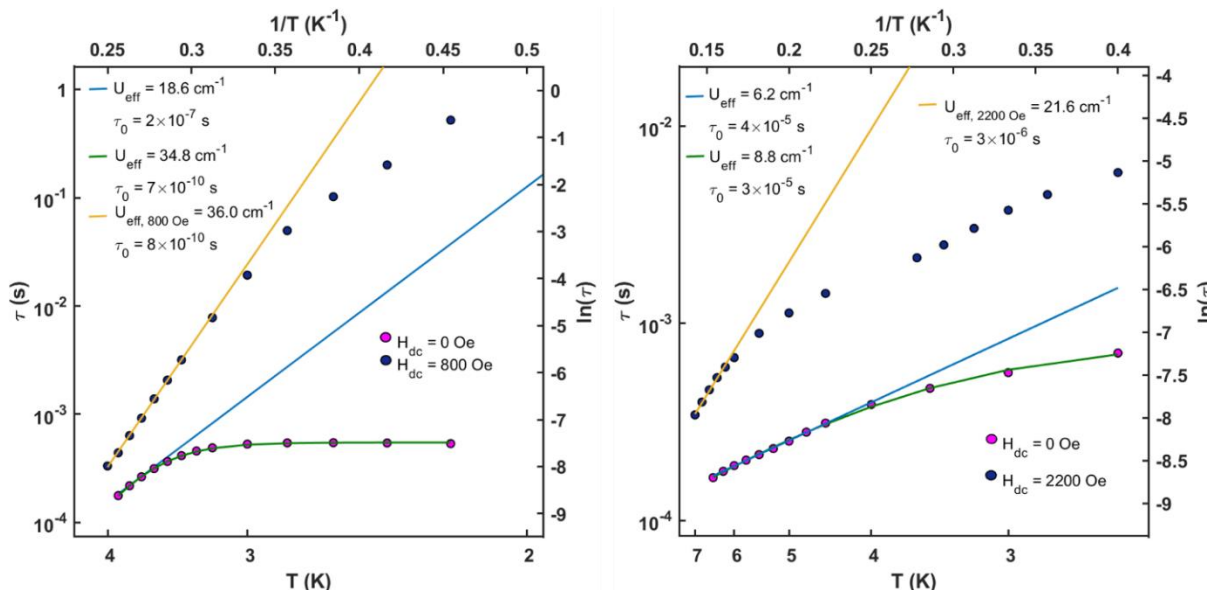
Figure 2.4: Arrhenius plots of AC magnetometry data for **1** (left) and **2** (right). Zero field data (pink dots) were fit to both an Arrhenius equation at high temperatures (blue lines) and to a combination of Orbach and QTM processes at all temperatures (green curves). Applied field AC susceptibility measurements (navy dots) performed at 800 Oe for **1** and at 2200 Oe for **2** were fit only to an Arrhenius equation at high temperatures (yellow lines).

The relaxation dynamics of **1** and **2** were studied using AC susceptibility measurement techniques (Figure 2.4). Relaxation times (τ) for both compounds were calculated from frequency dependent AC susceptibilities at different temperatures (H_{DC} = 0 Oe, ν = 1-1000 Hz) by simultaneously fitting the in-phase (χ') and out-of-phase (χ'') components to a generalized Debye equation.[4] Cole-Cole plots of these fitted data form low-eccentricity semicircles, indicating only a single relaxation time for both compounds at each temperature. For AC relaxation data collected under an applied field, optimized fields at 2K were determined by finding the minimum frequency at which χ'' shows a maximum, and noise was minimized by varying the AC drive field between 2 to 8 Oe from high to low frequencies, respectively.

Plotting $\ln(\tau)$ against $1/T$ for **1** reveals two distinct regimes: a roughly linear region corresponding to a temperature-dependent relaxation process at higher temperatures (3.5-4 K) and a temperature-independent plateau corresponding to a QTM process below 2.8 K. Fitting these points to a combination of Orbach and QTM mechanisms yielded an effective barrier (U_{eff}) of 34.8 cm^{-1} and an attempt time (τ_0) of $7 \cdot 10^{-10}$ s, consistent with single-molecule relaxation behavior. The U_{eff} value is significantly lower than the predicted ΔKD_{1-0}; this discrepancy can be accounted for by the lack of dynamic correlation in the performed calculations and higher degree of covalency between Er^{3+} and COT^{2-} relative to other ligands. A pure Arrhenius linear fitting based on data with $T \geq 3.6$ K yields $U_{\text{eff}} = 18.6$ cm^{-1} and $\tau_0 = 2 \cdot 10^{-7}$ s. This behavior is significantly different from dinuclear [Er(COT)]$^+$ species previously described, as under-barrier pathways at even high temperatures are not effectively suppressed. The dinuclear [Er(COT)I(MDPP)]$_2$ exhibited long-timescale relaxation, a barrier consistent with excitation above KD$_1$, and a computationally pure ground spin-orbit state; we attributed this to parallel alignment of the Er^{3+} anisotropy axes and weak crystal field perturbations imposed by the soft Lewis basic bridging and ancillary ligands. Contrarily, **1** exhibits fast relaxation, a small barrier below KD$_1$ as calculated for each center, and a heavily first excited state. The apparent lack of temperature dependence at low temperatures is also surprising in light of the predicted high-anisotropy dipolar-coupled states predicted from POLY_ANISO.[113]

The large value for τ_0 measured from the supposed Arrhenius region in **1** indicates that the relaxation mechanism does not proceed predominantly *via* an Orbach mechanism within this temperature range. Thus, to gain further insight into this energy separation, AC susceptibility measurements were performed under an optimized 800 Oe applied field to gain a better insight into the Orbach mechanism. The temperature-independent QTM region is no longer apparent

above 2 K, and a clear linear region corresponding to a thermally-activated Orbach process in $\ln(\tau)$ vs $1/T$ exists above 3.4 K; fitting an Arrhenius equation to these data yields $U_{\text{eff}} = 36.0$ cm^{-1} and $\tau_0 = 8 \cdot 10^{-10}$ s. This barrier corresponds reasonably well with the results obtained from fitting the zero-field AC susceptibility measurements to a combination or Orbach and QTM processes, and the attempt time agrees well with a pure Orbach relaxation mechanism for a lanthanide SMM. However, this is still significantly below the predicted barrier from ΔKD_{1-0}. Below 3.4 K, the temperature dependence weakens, and relaxation via QTM pathways has been suppressed. Fitting to additional relaxation processes was not performed to avoid overparameterization.

Surprisingly, the relaxation measurements for **2** revealed a much wider measurable temperature range of relaxation times between 2 and 6.5 K. While $\ln(\tau)$ vs $1/T$ does not clearly level off at low temperatures, indicating that a pure QTM relaxation process is not apparent in the measured temperature range, fitting the data to a combined Orbach and QTM mechanism yields $U_{\text{eff}} = 8.8$ cm^{-1} and $\tau_0 = 3 \cdot 10^{-5}$ s. A roughly linear region in $\ln(\tau)$ vs $1/T$ is seen above 4.5 K; an Arrhenius fit of these data gives $U_{\text{eff}} = 6.2$ cm^{-1} and $\tau_0 = 4 \cdot 10^{-5}$ s. While this barrier is far smaller than was determined for **1**, relaxation behavior is both seen at higher temperatures and is observed to be slower at 2 K. If we attribute this to the computed single-ion properties, this is consistent with the lower transition probabilities for QTM described for Er-**2b** relative to Er-**1**. However, upon comparison with outputs from POLY_ANISO, this barrier more closely resembles the energy difference between the ferromagnetic and antiferromagnetic doublets arising from coupling the $m_J = \pm15/2$ ground states of Er-**2a** and Er-**2b**.

As the observed relaxation behavior does not correspond well to either computed ΔKD_{1-0}, AC relaxation measurements were performed under an optimized 2200 Oe applied field to suppress under-barrier processes. A roughly linear region appears in $\ln(\tau)$ vs $1/T$ above 6.2 K.

Fitting this high-temperature linear region to an Arrhenius function between 6.2 K and 7 K yields $U_{\mathrm{eff}} = 21.6$ cm^{-1} and $\tau_0 = 2 \cdot 10^{-6}$ s. At lower temperatures, a weaker temperature dependence is observed. This barrier is closer to what is expected computationally, though still deviates significantly. Again, the high τ_0 indicates a poor fit to an Orbach mechanism in the high-temperature regime. As larger applied fields than 2200 Oe do not appreciably change relaxation times for **2**, we were not able to locate a region in which the Orbach mechanism is the dominant relaxation pathway. Therefore, we present $U_{\mathrm{eff}} = 21.6$ cm^{-1} as the lower bound for the effective relaxation barrier and $\tau_0 = 2 \cdot 10^{-6}$ as the upper bound for the attempt time. Fitting additional relaxation processes was not performed to avoid overparameterization.

When comparing relaxation data to the ab initio calculated magnetic state structure, some discrepancies in our description arise. For **1**, the slightly lower barrier than expected is not an uncommon difference; ab initio calculated state separations often need to be scaled. However, the persistence of what appears to be a fast QTM process despite the presence of dipolar coupling is puzzling. According to POLY_ANISO, transition rates between dipolar-coupled doublets are on the same order as QTM was predicted to be in SINGLE_ANISO. It could be that a fast attempt time for this transition limits its effect at low temperatures. Furthermore, these calculations are based on a static structure; molecular dynamics can introduce new pathways for relaxation not reflected by this model. For **2**, this interpretation is taken to the extreme. Without the application of an external field, the observed barrier is an order of magnitude smaller than the calculated one, and it more closely resembles the separation between states after dipolar coupling. However, while the perturbation model used in SINGLE_ANISO holds due to the relative scales of the spin-orbit coupling parameter and crystal field strengths, the expected dipolar coupling strength is only an order of magnitude smaller than $\Delta\mathrm{KD}_{1\text{-}0}$. Treating it as a simple perturbation may no longer be an

49

appropriate assumption; contributions of the excited state should be accounted for in such cases to accurately model the energy landscape. Alternatively, the decreased anisotropy in the ground states may make the Lines model insufficient to describe interactions between them. To avoid this mixing, more charge-diffuse ligands should be employed as bridges.

While calculations show that anisotropy is conserved at each erbium center, both dinuclear complexes were observed to have far lower barriers than were computationally predicted for the single-ion centers and slightly lower barriers than reported for a mononuclear species with one phenoxide ligand (U_{eff} = 44.1 cm^{-1}, H_{DC} = 2500 Oe).[110] While the [Er(COT)]$^+$ units in **1** are oriented parallel to each other, **2** relaxes almost ten times slower than **1** at 2 K under zero applied field, contrary to the trend we have previously reported for a phosphine-scaffolded iodide-bridged system. This is indicative of a common problem among coupled lanthanide SMMs, wherein it is difficult to balance a favorable coordination environment, suitably strong coupling, and anisotropic alignment of subunits within a cluster. Furthermore, the small barrier and non-negligible degree of mixing within the lowest two Kramers doublets brings into question the legitimacy of modeling dipolar coupling as a perturbation upon the ground state without considering contributions from KD_1.

2.7 Conclusions

We have synthesized two dinuclear alkoxide bridged single-molecule magnets and described their magnetic properties through comparison of their coordination environment, *ab initio* calculated electronic structure, and static and dynamic magnetic behavior. Both compounds' relaxation behaviors deviate significantly from those previously described for dinuclear [Er(COT)]$^+$ compounds, illustrating the effects of a much stronger crystal field contributed by the hard Lewis basic alkoxide ligands. While the symmetry and angle between the calculated

anisotropy axes differ greatly between **1** and **2**, their effective barriers differ very little. Despite the parallel alignment of both metal centers' anisotropy axes, **1** displays a larger QTM contribution to relaxation than **2** and relaxes much more quickly. However, at high temperatures a nearly pure Orbach mechanism can be observed to dictate relaxation under an applied field in **1**, whereas **2** displays multiple operant relaxation processes at all measured temperatures consistent with heavy mixing. Softer ligands should be employed as bridges to avoid stabilization of low-moment states. Though ferromagnetic coupling interactions are clearly present in both systems, single-ion crystal field effects appear to dominate contributions to relaxation behavior at all measured temperatures. From these data, we can refine the design principles toward incorporating the $[Er(COT)]^+$ unit into larger structures. First and foremost, ligands must be judiciously chosen to avoid dramatic perturbation of the anisotropy by hard Lewis basic interactions in an unoptimized geometry. Furthermore, while the orientation of anisotropy axes can enhance coupling between highly anisotropic centers, it is not in and of itself able to overcome poor anisotropy and weak single-ion magnetism. We anticipate that the magnetostructural and synthetic principles gleaned from this study will further facilitate the rational incorporation of anisotropic structural units into complex molecule-based magnets.

3.1 Introduction

Synthesis and study of electron spin materials at the molecular level, or molecular magnetism, has flourished since the discovery of quantum tunneling of the magnetization metal clusters such as Mn_{12}[14]. These sparked a flurry of research activity, continually honing the ability to predict and synthesize molecules with more complex magnetic structures and unprecedented relaxation behavior of these new quantized superparamagnets, known as single-molecule magnets (SMMs).[7,28,114–119] Soon, focus shifted from a "giant spin" approach to SMMs based on isolated single-ions, usually lanthanides or low coordinate transition metals, with giant anisotropies and much smaller spin vectors. These SMMs, dubbed single-ion magnets (SIMs) to indicate their magnetization in isolation from interactions with other magnetic centers, have relaxation dynamics controlled by facile wavefunction mixing due to the small spin. To control their spin dynamics, researchers are continuously refining an array of synthetic design principles to suppress mixing through static[37,39,45,58,100,120–122] and dynamic[123–125] elements of the crystal field environment around the magnetic ion, and suppressing quantum tunneling of the magnetization (QTM) pathways with highly symmetric ligand scaffolds.[44,119,121,122] Another approach is to suppress the strength of low-symmetry and fast timescale relaxation through strong exchange coupling other spin centers, fusing the giant spin behavior of the original SMMs with the large anisotropy of the SIM approach. While strongly-coupled systems displayed the most striking behavior, methods for isolating and controlling the ground state via this strategy have been an ongoing synthetic challenge that has forced numerous revisions to ideas of electronic structure and bonding in coordination complexes.[64,70,126–130] However, preceding their discovery, it was noted that in certain

instances, very weakly coupled molecular clusters displayed magnetic relaxation times consistent with thermal excitation of the local SIM as if it had far purer wavefunction than the local symmetry would seem to indicate.[131–133] In such instances, the highly anisotropic magnetic dipole moment of the component SIMs induces local field perturbations on its neighbors, providing an internal magnetic bias that offsets the energy of the quantum-tunneling of magnetization (QTM).[8,59] This mechanism was recognized as a powerful way to expand the fundamental scope of the field to include a nuanced control of the spin wavefunction symmetry and potentially allow the generation and study of systems that can leverage the QTM in exciting ways and generate unique non-equilibrium behavior. The unique challenge presented by this method is that the transformation of the angular momentum representation in "spin space" should be well-defined and ideally independent of bridging ligands. Such a description is possible by assigning a pseudospin approximation that allows projection of the spin anisotropy tensor, g, into cartesian space. Given modern computation methods, this is a generally accessible method. An inherent goal of molecular magnetism, however, is model-driven synthetic design of spin behavior, and this is a far greater challenge. It is tempting but dangerous to assume that SIMs in the presence of weak coupling can be modeled by additive behavior of the SIM anisotropy combined with the magnetic dipolar interaction. Even subtle changes in the local crystal field can alter SIM behavior drastically. To be able to achieve systems where this assumption is valid and a magnetic building block is accessible, care must be taken in the angular dependencies of the local wavefunction to guard it against drastic shifts upon coordination. The success of this approach means that the ligands involved in coordination must have little effect on the coupling, which is then almost solely determined by the magnetic dipolar interaction.[113] (Figure 3.1) Moreover, with QTM gated by the internal bias field, transitions within the ground state in the zero-applied-field, low temperature regime are limited by

the low probability of two phonon processes with energy of the dipole-coupling gap (usually on the order of 1 cm^{-1}). Thus, the real power of this method is that the precise control of spin-orbit and crystal field interactions offered by the lanthanides can be extended to another order of magnitude in energy and another dimension of tunability through incorporation of the magnetic dipolar coupling perturbation. Furthermore, if the magnetic dipole can be predictably associated with an internal coordinate of the core anisotropy determining unit, the orbital-agnostic nature of the magnetic dipolar interaction makes a zeroth order prediction of the behavior under any symmetry or cluster size computationally trivial.
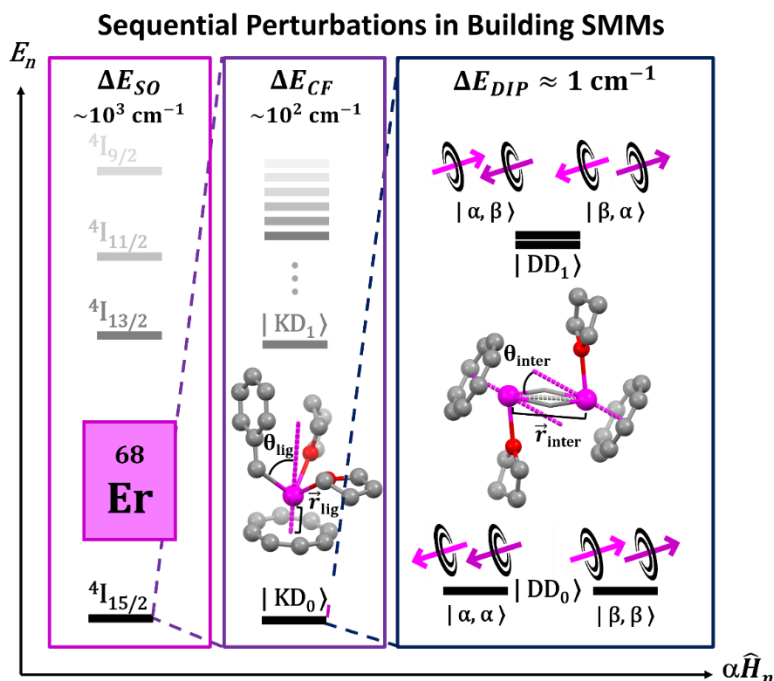
Figure 3.1: Illustrative progression of molecular magnetic perturbations. (Left) Spin-orbit coupling is principally governed by choice in lanthanide. (Middle) Splitting of spin-orbit states into m_J levels is determined by the crystal fields strength as enforced by the local ligand environment ($\vec{r}_{lig}$, θ_{lig}). (Right) Energy and moment of dipolar coupled states depends on intermetal interactions described by $\vec{r}_{inter}$, θ_{inter}.

In its general form, the magnetic dipolar exchange Hamiltonian can be written as:

$$\hat{H}_{dip} = \frac{\mu_B^2 \mu_0}{r^3}\left(\mu_1 \otimes \mu_2 - 3\frac{(\hat{\mu}_1 \cdot \vec{r}) \otimes (\hat{\mu}_2 \cdot \vec{r})}{r^2}\right) \qquad \text{Eqn. 3.1}$$

where μ_B is the Bohr magneton, r the internuclear vector and μ_0 the permittivity of free space. Moments of the magnetic centers, μ_1 and μ_2, are treated as pseudospin-½ operators, $\tilde{S} = g \cdot \hat{S}$ where $\hat{S}$ is the spin-½ operator and g maps the magnitude and anisotropy of the true ground state onto the vector space $g = \{g_x, g_y, g_z\}$. If the true spin ground state is composed solely of the highest magnitude angular momenta from the individual spins (e.g. for Er^{3+}, $m_J = \pm15/2$) then we can simplify $g = \{0, 0, g_z\}$, and Eqn 1 simplifies to the classical magnetic dipole equation:

$$E_{dip} = \frac{\mu_0}{r^3}\left(\mu_1 \cdot \mu_2 - 3\frac{(\mu_1 \cdot \vec{r})(\mu_2 \cdot \vec{r})}{r^2}\right) \qquad \text{Eqn. 3.2}$$

where μ_1 and μ_2 have been simplified as classical dipole magnetic moments, $\mu_i = \frac{1}{2}g_z\mu_B$.

The $[ErCOT]^+$ (COT = cyclooctatetraenide dianion, COT^{2-}; hereafter referred to as ErCOT) half-sandwich unit acts as a synthetic building unit with predictable anisotropy pinned to easily modifiable structural parameters. Therefore, it is an ideal candidate for exploring and describing the ability of carefully directed dipolar interactions to enhance desirable magnetic properties. Furthermore, the unit lends itself to isolating nearly identical first coordination spheres across a variety of nuclearities, allowing for a description of the resulting magnetic properties accounting for properties arising from single-ion behavior and coupling.[113,73,75,134] We present herein three alkyl-bound ErCOT complexes that highlight the level of fine-control over coupling between isolated spin-orbit coupled states offered by the dipolar interaction. Evidence and further insight are brought by the combined picture from ab initio calculations, static and dynamic magnetism, and the direct imaging of magnetic transitions and their interaction with the lattice through far-infrared magnetospectroscopy (FIRMS).
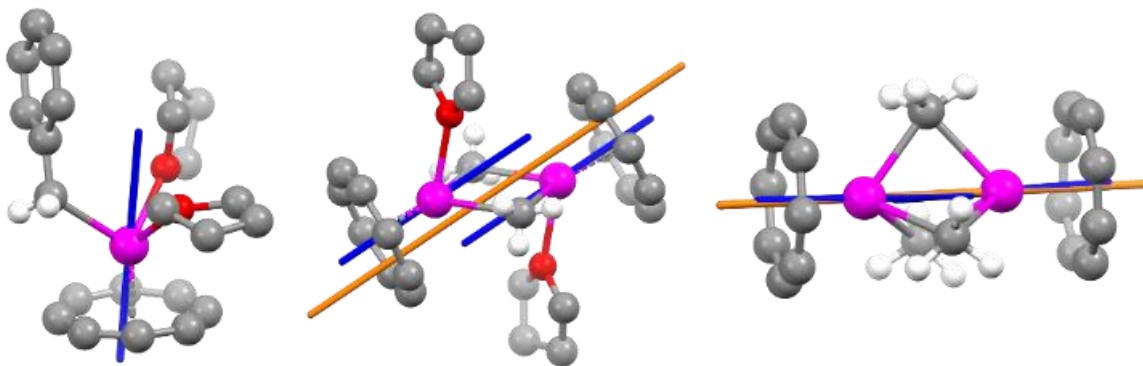
Figure 3.2: Crystallographically determined structures of **1** (left), **2** (middle), and **3** (right) with ab initio calculated ground state single-ion (blue) and dipolar-coupled easy axes (orange). Non-alkyl hydrogens are omitted for clarity. Alkyl hydrogens were located explicitly for **1** and **2**; hydrogens positions on bridging methyl ligands in **3** were optimized with DFT using the ORCA package.

3.2 Materials and Methods

<u>Synthetic Procedure</u>

All manipulations were carried out under anaerobic, anhydrous conditions under an atmosphere of nitrogen gas using standard Schlenk line and glovebox techniques. Pentane, toluene, diethyl ether, dimethoxyethane (DME), and tetrahydrofuran (THF) were dried on activated alumina columns or sodium/potassium amalgam (Na_2K) and stored over a 1:1 mixture of 3 and 4 Å molecular sieves for at least two days before use. ErI_3, and YI_3 powders were purchased from Alfa Aesar and Strem Chemicals, and methyllithium solution, potassium *tert*-butoxide, and neutral cyclooctatetraene (COT) were purchased from Aldrich; all were used as received. Dipotassium cyclooctatetraenide,[48] (η^8-cyclooctatetraenyl)-iodo-bis-tetrahydrofuran-erbium (and the yttrium analog),[73] benzyl potassium[135], and methyl potassium[136] were prepared via previously reported methods. Elemental analyses were conducted by Midwest Microlab, Indianapolis, IN. Following reviews of the practicality of elemental analysis in air sensitive complexes and of the consistency of common commercial elemental analysis providers, coupled with the extreme instability of our reported compounds compounds, elemental analyses were not pursued to rigorous percentages.[137] Best analyses are reported, and the corresponding samples were used for magnetic analyses.

Synthesis of Benzyl-(η^8-cyclooctatetraenyl)-bis-tetrahydrofuran-erbium (**1**)

To a solution of (η^8-cyclooctatetraenyl)-iodo-bis-tetrahydrofuran-erbium (432.4 mg, 0.797 mmol) in THF was added benzyl potassium (103.8 mg, 0.797 mmol) in THF at −50 °C. A white precipitate rapidly formed to yield a lighter pink mixture than the starting solution. The resultant suspension was allowed to stir for one hour, after which it was centrifuged at 3000 rpm for 10 minutes. The pink supernatant was removed from the white pellet and dried under vacuum, and the resulting solid (or wax) was redissolved in THF. Large, pink, crystallographically pure crystals of **1** were obtained *via* vapor diffusion of pentane into THF at room temperature. Yield: 344.4 mg (0.680 mmol, 85.3 %). Best CHN analysis (calc., found) for $ErO_2C_{23}H_{31}$: C (54.51, 52.31), H (6.17, 5.92), N (0, 0). The solid product is extremely sensitive, and it can be observed to decompose into an orange wax, then a white powder at ambient temperature if the atmosphere has >1 ppm O_2, making elemental analysis largely fruitless. Removal from oxygen-free environments leads to near-instant degradation. Bulk purity is confirmed by PXRD (matching single-crystal calculated patterns well), 2 K saturation magnetization, and room temperature susceptibility.

Synthesis of the yttrium congener (**1-Y**) was performed by the same method.

Synthesis of Bis[(η^8-cyclooctatetraenyl)-μ-methyl-tetrahydrofuran-erbium] (**2**)

A solution of (η^8-cyclooctatetraenyl)-iodo-bis-tetrahydrofuran-erbium (452.4 mg, 0.834 mmol) in THF was added to solid methyl potassium at −50 °C (45.1 mg, 0.834 mmol). The resultant suspension rapidly changes from yellow-orange to pink. The suspension was allowed to stir for one hour, after which it was centrifuged at 3000 rpm for 10 minutes. The pink supernatant was removed from the white pellet, dried under vacuum, and the solid was redissolved in THF at 35 °C. Large, pink, crystallographically pure crystals of **2** were obtained *via* vapor diffusion of pentane into THF at room temperature, and increased yield can be achieved by moving the vial to

a −45 °C freezer. Yield: 136.9 mg (0.192 mmol, 23.1 %) Best CHN analysis (calc., found) for $Er_2O_2C_{26}H_{38}$: C (43.65, 42.20), H (5.34, 5.33), N (0, 0). The solid product is extremely sensitive, and it can be observed to decompose into a peach powder at ambient temperature if the atmosphere has >2 ppm O_2, making elemental analysis largely fruitless. Removal from oxygen-free environments leads to near-instant degradation. Bulk purity is confirmed by a combination of PXRD, 2 K magnetization, and room temperature susceptibility.

Synthesis of the yttrium congener (**2-Y**) was performed by the same method.

Synthesis of Lithium tris(μ-methyl)-bis[(η^8-cyclooctatetraenyl)-erbium] (**3**)

To a solution of (η^8-cyclooctatetraenyl)-iodo-bis-tetrahydrofuran-erbium (470.5 mg, 0.867 mmol) in THF was added 1.6 M methyl lithium (921 µL, 1.474 mmol, 1.7 eq) in diethyl ether at −50 °C. The solution quickly lightened to a transparent pale pink solution. The resultant mixture was allowed to stir for one hour, after which it was filtered through a glass fiber filter topped with celite. The light pink solution was dried under vacuum to a vibrant pink oil which was then triturated with pentane. The resultant light pink solid was washed twice with diethyl ether. Large, light pink, crystallographically pure needle-like crystals of **3** were grown *via* vapor diffusion of pentane into a 2:1 mixture of THF and DME at room temperature. Yield: 229.6 mg (0.265 mmol, 30.6 %). The Li(THF)$_4$ analogue can be isolated *via* diffusion of pentane into THF. CHN analysis (calc., found) for $LiEr_2O_6C_{31}H_{55}$ (**3-DME**): C (43.03, 42.08); H (6.41, 6.73); N (0.00, 0.00).

Physical Measurements

Single crystal X-ray data for all compounds, unless otherwise noted, were collected at 100 K on a Bruker κ(α) Diffractometer with a Mo Kα radiation source and an Apex II Area Detector. Single crystals were removed from solvent, covered in paratone oil, and mounted on a loupe and immediately transferred to the instrument's nitrogen stream. The structures were solved using

direct methods via the SHELXT routine and refined using full-matrix least-squares procedures with the SHELXL[105] routine. Olex2 was used as a graphical front-end.[106] Hydrogens were modelled using a riding model for non-bridging carbon positions. Methyl hydrogens were located crystallographically and restrained to their locations with allowed bond length and angle refinement for all versions of **1-Ln** and **2-Ln** and for **3-THF** and **3-Y**. For **3-DME**, hydrogens were placed with a riding model after connecting their corresponding carbons to a dummy atom at the centroid of the structure, after which the centroid was deleted and the hydrogens were constrained to their positions before refinement. Powder crystal X-ray data for all compounds were collected at 100 K on a Bruker $\kappa(\alpha)$ Diffractometer with a Mo or Cu Kα radiation source and an Apex II CCD Area Detector. Dried samples were ground, covered in paratone oil, and mounted onto a standard loupe and immediately moved under a cold nitrogen stream to freeze. Powdered diffraction patterns were compared to calculated patterns from the Mercury visualization software. PXRD patterns confirmed phase purity for all paramagnetic species; yttrium-based compounds have bulk purity determined by nuclear magnetic resonance instead.

Magnetic analyses were conducted with a Quantum Design MPMS3 SQUID Magnetometer running in DC scan and Vibrating Sample Magnetometer (VSM) mode. All ground microcrystalline samples were loaded in custom quartz tubes (D & G Glassblowing Inc.), covered in eicosane wax, and sealed under static vacuum below 300 mTorr. After sealing, the eicosane was melted to minimize torquing and ensure good thermal conductivity during measurements. All static susceptibility data were corrected for diamagnetic contributions from eicosane and the samples themselves using Pascal's constants.[107] DC susceptibility measurements were collected with H_{DC} = 1000 Oe. Isothermal magnetization data was either collected by allowing the sample to equilibriate at steps at an average sweep rate of H_{DC} = 10 Oe/s or by sweeping the field in VSM

mode at a rate of H_{DC} = 20 Oe/s (when the DC free center signal could not be completed due to a measurement reset at extrema with high moment samples). Zero-field AC susceptibility studies for all compounds were conducted between 0.1–1000 Hz (H_{dc} = 0 Oe, H_{AC} = 2 Oe). Optimized DC fields for AC susceptibility studies under an applied field were found by finding the field under which the complex exhibited the maximum relaxation time at a given temperature. AC susceptibility studies were then conducted between 1-1000 Hz (H_{DC} = 800 Oe [**2**, **3**], 1050 Oe, H_{AC} = 3 Oe [800 Oe applied, all frequencies]; 2 Oe [1000-100 Hz], 4 Oe [100-0.1 Hz] [1050 Oe, **1**]).

For **3**, comparison between magnetic samples suggested an inconsistent structure upon exposure to vacuum, likely due to desolvation of the lithium-THF moiety. The structure bearing the lithium-DME solvate displayed data consistent with the crystallographically-derived molar mass and was consistently reproducible and was thus chosen for measurement.

For FIRMS measurements, samples were prepared on-site at the National High Magnetic Field Lab in Tallahassee, Florida. In an air- and water-free glove box, all samples were loaded as ground crystalline powders into a specialized brass sample holder (pictured below) with holes covered with clear tape. Eicosane (which does not absorb IR within the FIR range) was loaded with the samples which were then melted together. The frozen pellets were covered with clear tape to ensure isolation from the atmosphere; the tray was loaded into a capped centrifuge tube which was sealed with electrical tape during transfer. Samples were then loaded onto the probe in SCM3, which was evacuated and cooled to 4.2 K. FTIR transmission measurements were performed with a customized Bruker spectrometer at single field stabilized fields between 0 and 17 T. To obtain a background, the measurements at 0 and 17 T were averaged. This background, which contains all field-independent peaks, was subtracted from each other spectrum to obtain the 3D intensity difference plots that represent magnetically-dependent FIR absorptions. Points were picked at

maxima when available, and at the center of broad peaks when clear maxima were not apparent. Overlapping peaks were fit with a pseudo-Voigt function. These points were fit to functions describing a simplified vibronic coupling Hamiltonian.[138]

<u>Computational Methods</u>

All DFT reference structures were calculated with the ORCA 4.2.1[139,140] program package. Input atom coordinates were taken from crystallographic diffraction data. The PBE0 exchange-correlation hybrid density functional was applied with the D3 dispersion correction.[141] The Ahlrichs def2 family[142] of basis sets were employed, with the def2-QZVPP basis set applied to lanthanides, def2-TZVPP basis set applied to all atoms in direct contact with the lanthanides, and def2-SVP applied to all other atoms to lower computational time. VeryTightSCF parameters were used for SCF iterations, with Grid5 being used for integration at each step besides the last, which employed a FinalGrid6. Final geometries and vibrations were visualized in ChemCraft.[143]

All single-ion calculations were performed using the SEWARD / RASSCF / RASSI / SINGLE_ANISO modules of OPENMOLCAS. Input atom coordinates were taken from molecular geometries from crystallographic data (**1**, **2**) or optimized in ORCA with each lanthanide position replaced with yttrium (**3**), as this geometry most closely matched crystallographically determined structures. In dinuclear structures, one erbium center was replaced with closed-shell yttrium. Solvent molecules and counterions were not included in the calculations to lower computation time. Basis sets of the ANO-RCC type were used and the quality of the specific basis function was selected based on the proximity of the atom to the metal (**Er:** ANO-RCC-VTZP; **atoms bound to Er:** ANO-RCC-VDZP; **all other atoms:** ANO-RCC-VDZ). Two-electron integrals were Cholesky decomposed (10^{-6} cutoff) to speed up calculations and save disk space. A CAS(11,7) was selected for the complete active space self-consistent f ield (CASSCF) procedure

and in this space we included 35 CI roots of spin multiplicity 4 and 112 CI roots of spin multiplicity

2. All RASSCF module output wavefunctions were used to compute the spin-orbit matrix elements

by the RASSI module. The RASSI module output was directed to SINGLE_ANISO for magnetic

properties calculations. Outputs from SINGLE_ANISO were used as is for single-ion descriptions,

and were used with POLY_ANISO to describe coupling.

All coupling calculations for **2** and **3** were performed using the POLY_ANISO module of

OPENMOLCAS. Each magnetic center was approximated as an Ising spin, and computations were

performed employing the Lines model for anisotropic exchange coupling. Input files called upon

by the module were obtained as outputs from the SINGLE_ANISO calculations performed above.

For unoptimized **2**, only a single input was used, and the second metal center was generated by

inversion symmetry. A**s** each compound has two distinct magnetic centers after geometry

optimization, no symmetry-generated centers were used in such cases. Only the lowest energy

doublet for each center was considered, and thus four states representing two pseudospin-½

doublets were computed. Dipolar interactions were calculated explicitly using *g* tensors obtained

from SINGLE_ANISO.
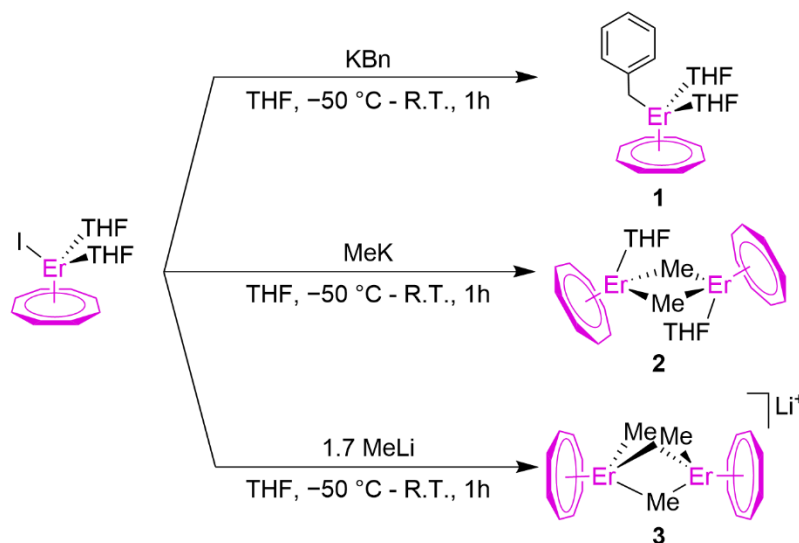
Scheme 3.1: Synthetic overview for **1**, **2**, and **3**.

3.3 Synthesis and structure

All reported complexes were synthesized using standard air-and water-free synthetic techniques. Three complexes were isolated: mononuclear ErCOT(Bn)(THF)$_2$ (**1**), and dinuclear [ErCOT(Me)(THF)]$_2$ (**2**) and Li[(ErCOT)$_2$(Me)$_3$] (**3**) (Bn = benzyl anion, $^-$CH$_2$C$_6$H$_6$; Me = methyl anion, $^-$CH$_3$; THF = tetrahydrofuran) (Scheme 3.1). All were obtained through salt metathesis via the addition of an alkali metal salt of the appropriate anion to the ErCOT halide salt, ErCOT(I)(THF)$_2$. Solid-state molecular structures of all compounds were determined by single crystal x-ray diffraction (Figure 3.2), and bulk purity is supported by powder XRD. Mononuclear **1** has a piano stool geometry with the benzyl anion and two THF ligands bound opposite to the COT^{2-} ring with approximate C_s symmetry. Complex **2** is an inversion symmetric combination of two pseudo-C_s symmetric molecules of **1** – a common motif among dinuclear LnCOT complexes.[75,134,144–152,74] Complex **3** has three identical bridging ligands and, with an approximated C_∞-symmetric COT^{2-}, can be approximated to an overall pseudo-D$_{3h}$ symmetry with local C$_{3v}$ symmetry at each metal center. Both **2** and **3** have small internuclear distances ($|\vec{r}_{Er-Er}|$ = 3.5 Å and 3.2 Å, respectively). The $\vec{r}_{ErCOT}$ vectors in **2** are strictly parallel, as enforced by crystallographic symmetry, but are oriented off-axis from the internuclear vector. In **3**, all three vectors are nearly colinear, but slight distortions break the parallel arrangement. As we have previously explored, we can predict the relative strength of the dipolar interaction from structural parameters (See ESI section 2). By assuming that the moment is pinned to $\vec{r}_{ErCOT}$, structural parameters can be used to give a preliminary model for the dipolar interaction. Using Eqn. 1, both **2** and **3** are predicted to have a ferromagnetically coupled ground state and antiferromagnetically coupled excited state. Assuming the systems are pairs of Ising-type pseudospin-½ states, the coupled doublets are expected to be separated by 0.0078·(g$_z$)^2 cm^{-1} for **2** and 0.0128·(g$_z$)^2 cm^{-1} for

3. If the two complexes have similar ground state anisotropy, then enforcing collinearity increased the barrier by a factor of 1.64.

3.4 Ab initio calculations

Table 3.1: Ab initio calculated magnetic parameters

	1	**2**	**3 (Optimized)**
$\Delta E_{KD0\rightarrow 1}$	58.5 cm^{-1}	65.5 cm^{-1}	66(3) cm^{-1}
$g_{x,\ KD0}$	0.01	0.01	0.007(6)
$g_{y,\ KD0}$	0.05	0.03	0.03(2)
$g_{z,\ KD0}$	17.61	17.56	15.502(2)
$g_{x,\ KD1}$	0.11	12.45	11.6(2)
$g_{y,\ KD1}$	1.32	6.08	7.2(2)
$g_{z,\ KD1}$	14.6	1.24	1.15(4)
$\Delta E_{DD0\rightarrow 1}$	*N/A*	2.055 cm^{-1}	3.904 cm^{-1}
$g_{x,\ DD0}$	*N/A*	0	0
$g_{y,\ DD0}$	*N/A*	$3\cdot10^{-7}$	0
$g_{z,\ DD0}$	*N/A*	35.12	35.00
$g_{x,\ DD1}$	*N/A*	0	0
$g_{y,\ DD1}$	*N/A*	0	$1\cdot10^{-8}$
$g_{z,DD1}$	*N/A*	0	0.705

To confirm our magnetostructurally-derived predictions, magnetic energy manifolds for **1-3** were modeled with the SINGLE_ANISO and POLY_ANISO modules of OpenMolcas (Figure 3.3, Table 3.1).[153] Typically, lanthanide-based SMMs can be modeled using crystallographically determined atom coordinates as inputs without further geometry optimization. However, alkyl ligands' electron density is strongly directional, and thus the magnetic states of the ligated metal are strongly affected by the orientation of the bonded carbon. Additionally, though hydrogens could be explicitly located from the crystallographic electron density map in **2**, they were heavily disordered in **3**, precluding assignment. Therefore, optimized hydrogen positions for **3** were calculated with the ORCA computational package.[139,140] The open-shelled Er^{3+} was replaced with Y^{3+} due to its similar ionic radius, and non-hydrogen atoms were frozen. The output had significantly increased energy separations between output Kramers doublets and decreased state

mixing relative to the unoptimized structure. This optimized output was also more consistent with experimental results and was therefore chosen to describe the energy landscape of **3**.

First, the uncoupled $J = \frac{15}{2}$ manifold was computed for each unique Er^{3+} center; to describe the uncoupled single-ion environment in **2** and **3**, a model complex was computed wherein one metal center was replaced with diamagnetic Y^{3+} to limit the calculation to only one open-shell ion. All Er^{3+} centers displayed Kramers doublets ground states (KD_0) predominantly composed of the $M_J = \pm\frac{15}{2}$ eigenstate; the largest mixing component are less than 6% $M_J = \pm\frac{9}{2}$. Their principal magnetic axes lie nearly coincident with $\vec{r}_{ErCOT}$ (Figure 3.2). The consequences of the different crystal fields are much clearer in their first excited states (KD_1). These excited states lie within an energy regime typical of ErCOT complexes bound to charge-dense ligands.[55,134] The percentage of $M_J = \pm\frac{1}{2}$ character in the first excited states increases across the series, where in **3** it almost entirely accounts for the excited state composition. Thus, sans coupling, the first excitation in **3** represents a transition from the most axial Kramers configuration to the most rhombic one.
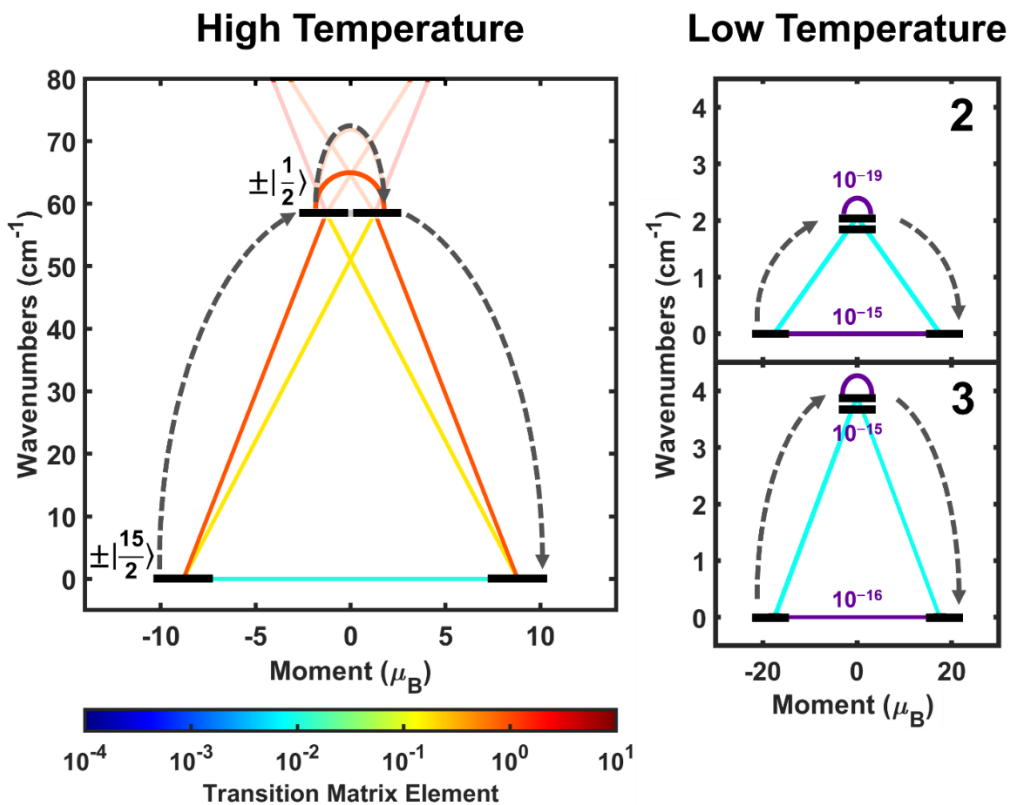
Figure 3.3: Predicted primary relaxation pathways as described by SINGLE_ANISO and POLY_ANISO. (a) In the high-temperature regime, relaxation proceeds primarily via excitation to the KD_1 manifold for **1**-**3**. In the low-temperature regime, only the KD_0 manifold is significantly populated leading to QTM in **1**. (b) Low energy excitations in the KD_0 manifolds of **2**-**3** due to exchange bias from dipolar coupling.

Both **2** and **3** bear closely spaced lanthanide ions with parallel oriented highly anisotropic ground states. Magnetostructurally, this implies a significant dipolar interaction. Thus, we consider the interactions between the ground states in **2** and **3** as modeled using the POLY_ANISO package in OpenMolcas (Figure 3.3).[154–156] To focus on the most important interactions, dipolar coupling was modeled only between members of KD_0, with inter-KD coupling with KD_1 considered minimal due to the large energy separation and state purity. Both **2** and **3** are predicted to exhibit a coupling of KD_0 states to give new ferromagnetically coupled dipole doublet ground state (DD_0) and antiferromagnetically coupled first excited state (DD_1), consistent with all other dinuclear ErCOT complexes we have reported. The energy separation between these states is 2.055 cm^{-1} in **2** and 3.904 cm^{-1} in **3**. The degree of control afforded by the dipolar interaction is immediately

apparent. First, the interaction is small compared to the energy gap between KD_0 and KD_1, allowing the coupled states to be treated as a first-order perturbation on the single-ion manifold while keeping the overall energy landscape intact. Furthermore, the energy separation between DD_0 and DD_1 conforms to magnetostructural predictions, with the coupled energy splitting in **3** being approximately 1.9 as large as in **2**.

With both sets of calculations in hand, we can predict relaxation behavior under the lens of transition probabilities. Transition matrix elements between states are proportional to the probability of that transition and, consequently, can be used to roughly describe the relative rates of those transitions.[112] For all three complexes, relaxation is clearly limited to the ground and first excited doublets. Relaxation via QTM in KD_0 (for **1**) is moderately fast, with an average transition matrix element of 0.01. Excitation to KD_1 in all three complexes via a thermally activated direct process is approximately ten times faster, and QTM within KD_1 is again ten times faster than that. Thermally assisted QTM and through-barrier direct processes from KD_1 are fast enough that, at high temperatures, over-barrier relaxation through the first excited state should be the favored relaxation pathway. At low temperatures, when there is insufficient energy to meaningfully populate the KD_1, QTM should be rapid for **1**. However, in **2** and **3**, through-barrier transition probabilities within DD_0 and DD_1 decrease by approximately ten orders of magnitude compared to those of uncoupled KD_0, and QTM can therefore be considered effectively quenched. Meanwhile, thermally-dependent excitations between DD_0 and DD_1 have approximately the same probability as the uncoupled QTM mechanism. The comparatively extremely slow QTM mechanism is therefore effectively suppressed, and thus transitions are limited to these thermal transitions between DD_0 and DD_1. The control of this new secondary barrier is then another useful tool toward tuning SMM behavior.

3.5 Static magnetization properties
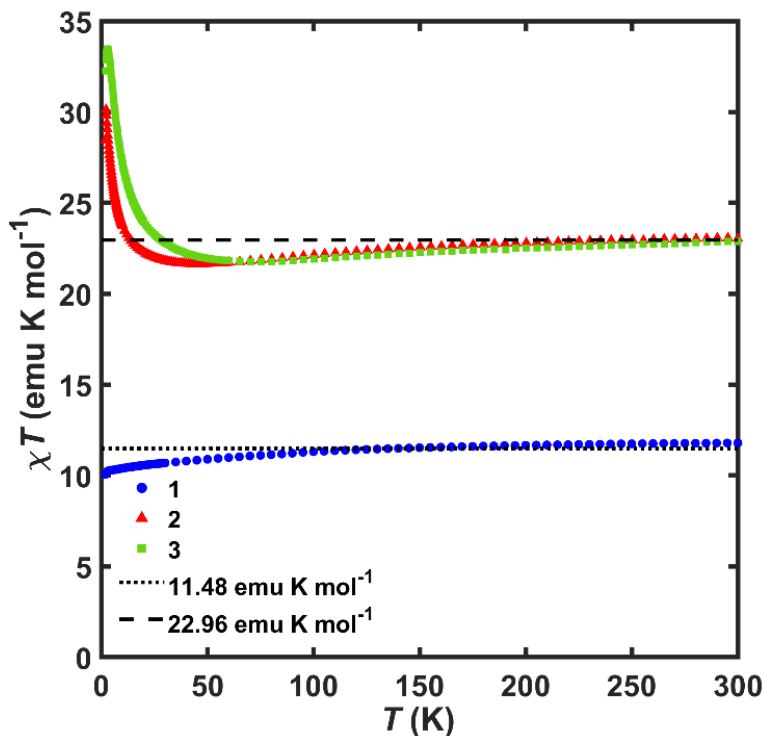
Figure 3.4: Temperature-dependent $\chi_M T$ measurements for **1** (blue circles), **2** (red triangles), and **3** (green squares) collected at 1000 Oe. Dashed lines are plotted for theoretical $\chi_M T$ values of compounds with one and two uncoupled Er^{3+} centers at 300 K.

Static and dynamic magnetic properties of **1, 2**, and **3** were measured in a Quantum Design MPMS3 SQUID magnetometer to probe the effect of tuning the dipolar interactions. First, temperature-dependent susceptibility measurements were performed to extract state information from the bulk response (Figure 3.4). The 300 K experimental $\chi_M T$ measured under a 1000 Oe applied field agree well to theoretical values for the appropriate number of uncoupled Er^{3+} ions (11.78, 23.03 and 22.86 emu K mol^{-1} for **1, 2**, and **3**, respectively; $J = 15/2$, $g = 6/5$ per ion; 11.48 emu K mol^{-1} per Er^{3+}).[3] At lower temperatures, $\chi_M T$ for **1** gradually decreases before dropping more rapidly near 2K, consistent with a typical depopulation of states in an SIM with low-lying excited states. For both **2** and **3**, $\chi_M T$ slightly decreases before rapidly increasing at lower temperatures, confirming the presence of ferromagnetic coupling. In **3**, this increase begins at

higher temperatures and continues to a higher maximum value than in **2**, which coincides with the larger energy gap between DD_0 and DD_1 in **3**. This comparison holds under the assumption that the corresponding states have the same moment in both complexes, as corroborated by the output from POLY_ANISO.

3.6 Dynamic magnetization properties

Relaxation times (τ) were extracted from frequency-dependent AC susceptibility measurements by simultaneously fitting the in-phase (χ') and out-of-phase (χ'') components to a generalized Debye equation (Figure 3.5).[4] Cole-Cole plots of these fitted data form semicircles, and χ'' curves display one peak each. Thus, only a single relaxation time is described at each temperature for each compound. The fitted τ values were fit to a combination of relaxation terms in equation 3.3:

$$\tau^{-1} = \tau_0^{-1} e^{-\frac{U_{eff}}{k_B T}} + CT^n + \tau_{QTM}^{-1} + \tau_D^{-1} e^{-\frac{D_{eff}}{k_B T}} \quad \text{Eqn. 3.3}$$

with the first term representing an Orbach process, or a thermally activated pathway involving excited states, and the second term representing Raman, or vibronically coupled, processes. The third term in equation 2 represents quantum tunneling of the magnetization, whereas the fourth describes thermal relaxation within the energy regime of KD_0 via excitation from the ferromagnetically coupled ground state (DD_0) to the antiferromagnetically coupled excited state (DD_1) over an energy barrier D_{eff}.[8,113] Both QTM and inter-DD thermal relaxation are expected to occur at very low temperatures, where sufficient thermal energy is not available for Orbach or Raman mechanisms to be comparatively efficient. QTM is expected to be prevalent in SIMs, and thermal relaxation through D_{eff} is expected to dominate in coupled SMMs. Therefore, only one of these terms is included in fits to extracted τ values (Table 3.2).
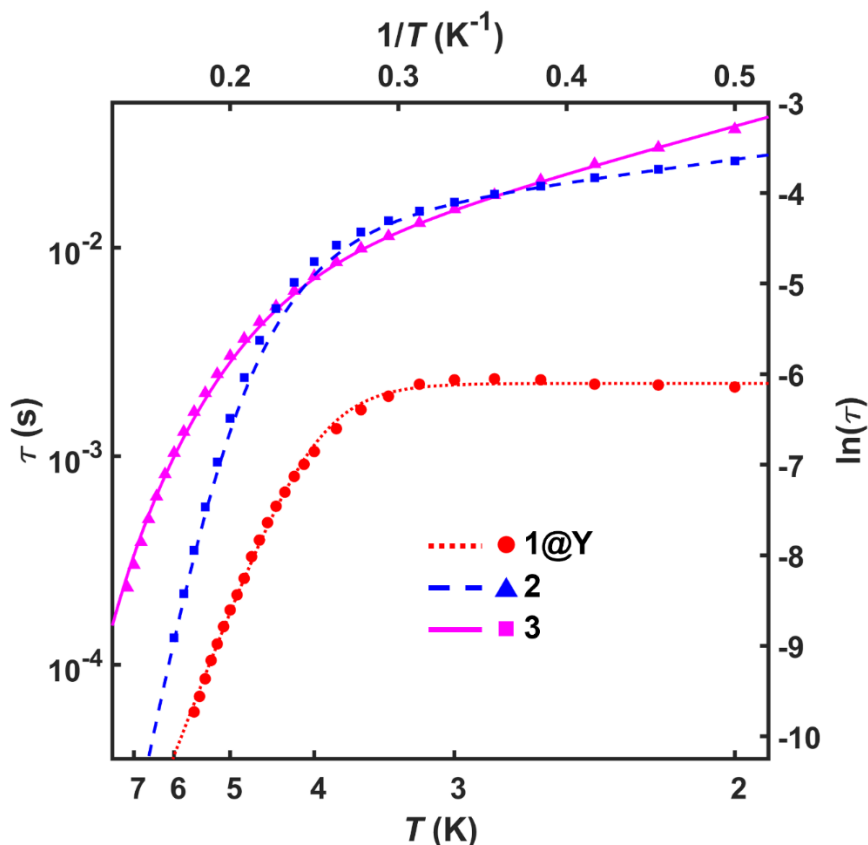
Figure 3.5: Relaxation behavior for **1@Y** (red circles), **2** (blue triangles), and **3** (pink squares) as extracted from AC susceptibility vs frequency measurements. Extracted τ values are represented with points, and fits to Eqn 3.3 are plotted as curves of their respective colors

Under zero applied field, only **2** and **3** display full peaks in χ'' vs v within the measurable window of 0.1 to 1000 Hz. Curves for **1** only display stacked tails of peaks at frequencies above 1000 Hz. At 2 K, a tentative fit places τ at 1.2×10^{-4} s. Such rapid relaxation is consistent with fast QTM mechanisms typical for SIMs – especially those with significantly mixed ground states. Dilution into an isostructural diamagnetic Y^{3+} lattice significantly reduces the effect of transient fields caused by nearest-neighbor intermolecular interactions. Thus, a 95:5 molar equivalent Y:Er mixture of **1** (**1@Y**) was prepared, and full peaks were observable in χ'', allowing the extraction of relaxation times below 6 K. Though fast relaxation processes facilitated by nearest-neighbor interactions are suppressed upon dilution, the fast QTM associated with uncoupled magnetic centers persists.

Table 3.2: Fit relaxation parameters for **1@Y**, **2,** and **3**

	1@Y	**2**	**3**
U_{eff}	34.3(7) cm^{-1}	66(3) cm^{-1}	79(6) cm^{-1}
τ_0	1(2) × 10^{-9} s	2(2) × 10^{-11} s	2(7) × 10^{-10} s
C		1(5) × 10^{-3}	3(2) × 10^{-3}
n		8.7(9)	6.9(2)
D_{eff}		1.6(3) cm^{-1}	3.4(1) cm^{-1}
τ_{QTM} / τ_D	2.23(5) × 10^{-3} s	8(2) × 10^{-3} s	3.2(3) × 10^{-3} s
τ_{max}	2.35(14) × 10^{-3} s	2.61(6) × 10^{-2} s	3.7(1) × 10^{-2} s

Both **2** and **3** show SMM behavior at zero field below 6 K and 7 K, respectively. When plotting $\ln(\tau)$ vs $1/T$, both complexes show Arrhenius behavior at their highest temperatures, followed by an attenuation of the temperature dependence of relaxation, culminating in a weakly temperature-dependent region near 2 K. Notably, neither complex displays a temperature-independent region consistent with QTM being the dominant process. All fit parameters are consistent with ab initio calculations, and the D_{eff} for **3** is expectedly larger than that for **2**. Some notable features when comparing the evolution of τ can be explained using D_{eff} and τ_D. Notably, **3** has a slightly larger barrier and τ_0 than **2**, and D_{eff} is twice as large. However, τ_D is smaller in **3** than in **2**, and thus there is an intermediate region wherein **2** relaxes slower than **3**. Fit parameters for **2** and **3** were corroborated by measurements under an applied field of 800 Oe as well as for diluted samples. Both **2@Y** and **3@Y** were prepared by co-crystallization of pre-prepared Er^{3+} and Y^{3+} samples of **2** and **3**; the presence of a large fraction of coupled Er^{3+} pairs was confirmed by low-temperature peaks in $\chi_M T$ and the ability to fit D_{eff}. Relaxation is changed very little upon dilution for both **2** and **3**, supporting the notion that the internal dipolar fields from coupling act to stabilize relaxation pathways from much smaller fields from neighboring magnetic centers, and thus these SMMs can be considered more effectively decoupled from their environment. An applied field similarly imparts almost no change to **3**. Relaxation in **2** is lengthened by about an order of magnitude at the lowest temperatures, manifesting in fits as an increased τ_D.

71

The relaxation of **1** can be juxtaposed against that of **2** and **3** to illustrate the degree of control afforded by dipolar coupling and the resulting consequences on magnetic properties. Primarily, the uncoupled, comparatively weaker anisotropy of **1** is highly susceptible to the complex, low symmetry dipolar environment which acts to enhance the available QTM processes within individual ions. This same sensitivity to QTM and neighboring spins is not present in **2** or **3**. Following the predictions afforded by POLY_ANISO, low-temperature relaxation in these complexes is dominated by the small thermal barrier imparted by the intramolecular dipolar coupling, which is directed to enhance the local anisotropy. The outcome of this effect is a lowering of the QTM probability by over ten orders of in the case of specific levels determined by the orientation of the anisotropy vector. Importantly, this mechanism is not a result of achieving a well-isolated coupling state, but instead it is more akin to a targeted exchange bias of the states responsible for magnetic relaxation. While the dipole-dipole interaction between the two ions is weak, it is important to note that it is far larger than the intermolecular dipolar fields between neighboring molecules, making both **2** and **3** relatively inert to fluctuations caused by their nearest neighbors. This is made clear by the lack of significant change in the relaxation dynamics of **2@Y** and **3@Y**.

3.7 Far-Infrared Magnetospectroscopy

To complement the description of the local magnetic landscape we have crafted, far-infrared magnetospectroscopy (FIRMS) was employed to probe the discreet vibrational modes involved with vibronically coupled magnetic transitions. While this technique is most often employed in surveying extended magnetic solids and qubit candidates,[30,125,157–162] recent work has employed FIRMS alongside single-crystal Raman magnetospectroscopy and inelastic neutron scattering experiments to probe zero-field splitting parameters in transition metal complexes[138,163]

and Kramers doublet separations in lanthanide SMMs[124,164,165] with energy separations too large to feasibly be observed in EPR ($>\sim 100$ cm^{-1}). While magnetic transitions are often IR-allowed, either by following magnetic/electric dipole selection rules or by relaxing these rules via $4f$-$5d$ orbital mixing, these transitions are very weak compared to vibrational modes and phonons.[166] The high difference in magnetic moments make these transitions far less allowed than pure vibronic transitions. Thus, magnetic transitions are isolated in field-independent-subtracted spectra, and the resulting 3D contour plot then shows the transitions' field dependence. While these spectra cannot be deconvoluted into crystal lattice vibration modes (phonons) and local molecular vibrational modes, tentative assignments of these transitions can be made to local vibrations modeled by DFT calculations performed on the optimized structures described earlier. However, due to the density of vibrational modes within this region and the limitations of modeling lanthanide complexes with DFT, these assignments are extremely tentative. They should not be used as a strict handle, but rather a suggestion of modes that are similar in energy and would be expected to have large consequences on the magnetic energy manifold.

FIRMS measurements at 4.5 K were performed from 0 to 17 T for **1**, **2**, and **3** (Figure 3.6). Weak, magnetically-dependent peaks are visible between 30 and 700 cm^{-1} for all three, and these transitions' intensities dramatically increase when in close proximity to a coupled vibrational mode. On approach, the magnetic and vibration transition mix in an observable avoided crossing. Since only states involving KD$_0$ are expected to be meaningfully populated for all three species at 4.5 K, the magnetic transitions are all assumed to be excitations from KD$_0$ (or the relevant dipolar splitting manifold for **2** and **3**). Given the low resolution of the FIRMS data, we do not model the dipolar manifolds individually, leading to an energy landscape described by a simplified spin-phonon coupling Hamiltonian:

$$\hat{H}_{coup} = \begin{bmatrix} \Delta_{KD} + B\mu_B(\Delta\mu_{KD}) & \Lambda \\ \Lambda & \Delta_{vib} \end{bmatrix} \qquad \textbf{Eqn. 3.4}$$

Δ_{KD} here is the unperturbed energy gap between the final state and KD_0; $B\mu_B(\Delta\mu_{KD})$ models the linear change in energy due to the Zeeman interaction, with $\Delta\mu_{KD}$ equal to the difference in magnetic moment between the final state and KD_0; Δ_{vib} is the energy of the uncoupled vibrational mode; and Λ is the vibronic coupling constant. The eigenvalues describing the energy shift of magnetic and vibrational modes due to coupling are extracted from the determinant:

$$0 = \begin{vmatrix} \Delta_{KD} + B\mu_B(\Delta\mu_{KD}) - \Delta_{\pm} & \Lambda \\ \Lambda & \Delta_{vib} - \Delta_{\pm} \end{vmatrix} \qquad \textbf{Eqn. 3.5}$$

where $\Delta_{\pm}$ describes the energies measured via FIRMS, representing the shifted energies of states after coupling and the corresponding eigenvalues. Additional vibrational modes can be accounted for by simplifying them as being coupled to the magnetic transition and uncoupled from each other using an extended Hamiltonian, but this is not necessary for our system.

Since relaxation is predominantly measured to occur within KD_0 and KD_1, we focus on transitions below 100 cm^{-1}. Furthermore, as KD_0 and KD_1 are relatively close together in all three complexes, mixing between them is expected in the high fields in the experiment. Thus, for simplicity, magnetovibronic transitions can be described in terms of single-ion states. Within the low energy landscape, two separate instances of one magnetic transition coupled to one vibrational mode were observed for **1**, a single magnetic transition coupled to one vibrational mode was observed for **2**, and only a weak magnetically dependent transition without any visibly coupled vibrational modes are discernable for **3**. The lowest transition for **1** appears at 57(1) cm^{-1}, consistent with our calculated and experimentally observed barriers. Assuming that the transition originates from the $M_J = +\frac{15}{2}$ state, this is also consistent with a transition to the $M_J = -\frac{1}{2}$ state ($\mu_{KD1,fit} = -1.4(8)$ μ_B, $\mu_{KD1,calc} = \pm 1.3$ μ_B). The coupled vibrational mode at 59.8(1) cm^{-1} mostly

closely resembles a computed mode at 60.9 cm^{-1} where twisting modes of the THF ligands and rocking of the COT^{2-} dominate. The fit magnetic transition for **2** at 62(1) cm^{-1} also corresponds well to the ab initio value of 65.5 cm^{-1}. The moment of KD$_1$ is similarly consistent ($\mu_{\text{fit}} = -0.9(9)$ μ_{B}, $\mu_{\text{calc}} = \pm0.93$ μ_{B}). As in **1**, the corresponding DFT calculated vibrational mode at 72.1 cm^{-1} involves both THF ligands with moderate twisting and wagging motions. Interestingly, only one of the two COT ligands has a large displacement within a rocking mode. Lastly, the bridging methyl ligands twist about the axis connecting both ligands' atoms.

In stark contrast to the other two complexes, the lowest magnetic transition visible in FIRMS for **3** does not appear to couple to any nearby vibrational modes. There is slight upward curvature below 1T near 80 cm^{-1} and above 4 T near 100 cm^{-1}, but the weak signal and experimental artifacts preclude meaningful discussion of vibronic coupling in this region without introducing significant error associated with fitting. The weak linearly magnetically dependent transition can be fit to the simple Zeeman equation:

$$\Delta_{KD} + B\mu_B(\Delta\mu_{KD}) = \Delta_{obs} \quad \text{Eqn. 3.6}$$

to extract Δ_{KD} and $\Delta\mu_{KD}$. Here, Δ_{KD} is 78.7(3) cm^{-1}, and the transition corresponds to an excitation to a state with moment $-0.3(6)$ μ_{B}. The fit barrier is higher than calculated, matching most closely to the first excited state ($\Delta_{1,calc} = 66.3$ cm^{-1}). The moment of the excited state likewise resembles the first excited state ($\mu_{KD} = \pm0.56$ μ_{B}). The closest vibrational modes calculated by DFT lie at 68.29 cm^{-1} and 69.69 cm^{-1}, corresponding to twisting modes of the bridging methyl ligands and slight rocking of the COT rings. Above the range in which the first transition is resolvable, the first available mode to couple to is at 108.03 cm^{-1}, which corresponds almost exclusively to twisting motions in the methyl ligands.

While the assignment of local molecular vibrational modes as mediators of the spin-lattice interaction is qualitiative, these tentative assignments allow for testable hypotheses regarding incremental molecular design. Specifically, both **1** and **2** display significant motion within the THF ligands. Considering both the large degree of freedom in movement within the ligand and the charge-dense nature of the coordinated oxygen atom, such a motion should perturb magnetic states so as to allow for thermally-assisted QTM. Thus, more rigid ligands or, in the case of **3,** a lack of hard Lewis basic solvent ligands may suppress coupling, as has been noted in other discussions.[42,44] The other major contributor to motion – the rocking of the COT^{2-} ligand – cannot be so easily suppressed. However, introducing bulky substituents, such as the silyl groups that have achieved much synthetic success,[28,52,113,152,167] could limit the degree of motion available to the scaffold. However, caution must be taken not to introduce additional modes of freedom within the added functional groups as well. Additionally, while the increased pseudosymmetry in **3** limits the number of IR active modes, the possibility of Raman-active modes prevents us from drawing clear conclusions relating to it.
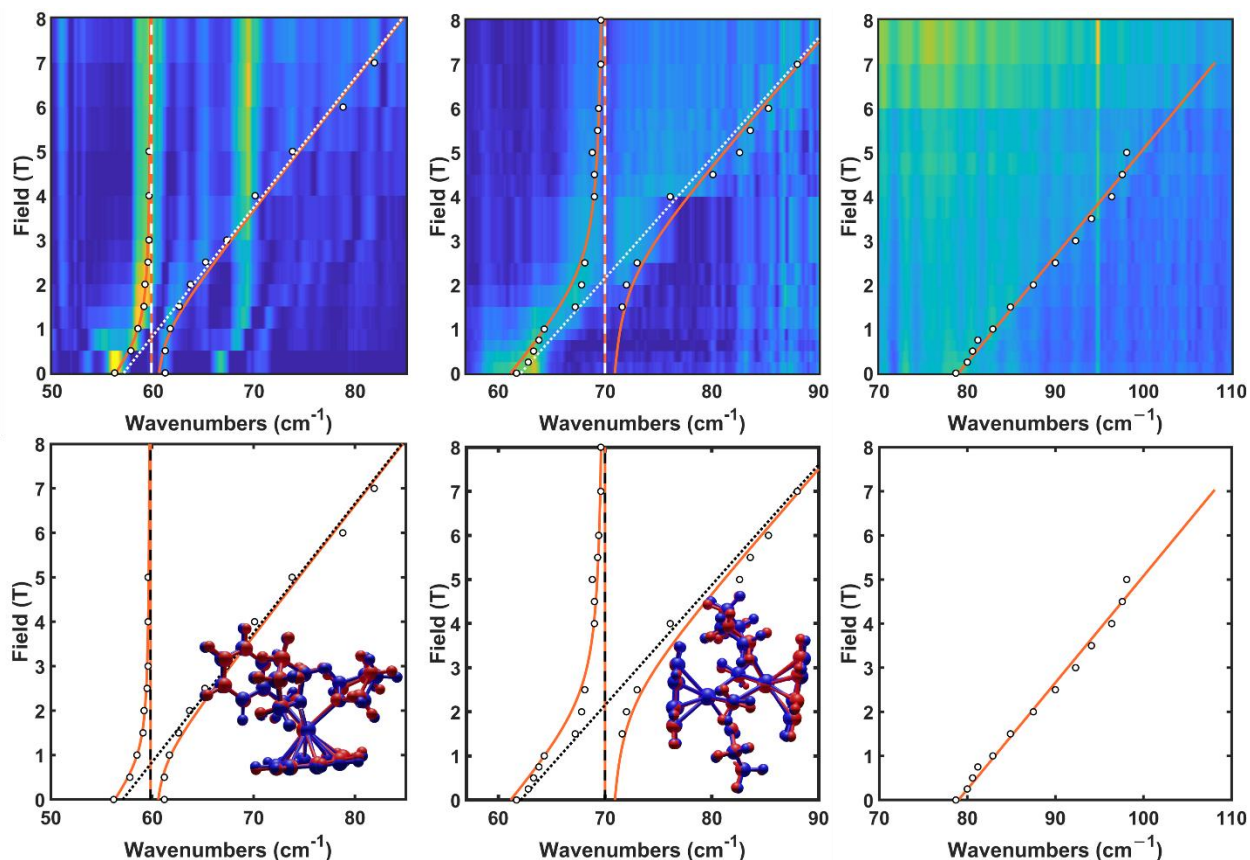
Figure 3.6: Lowest energy transitions visible in far-IR magnetospectroscopy for **1** (left), **2** (middle), and **3** (right). White dots represent experimental points, orange curves are fits to eqn. 3.5, and dashed and dotted lines represent vibrational modes and magnetic transitions extracted from FIRMS data, respectively. Modes are plotted both with (top) and without (bottom) contour plots for clarity. Inset structures represent coupled vibrational modes.

When juxtaposing **1** against **2** and **3**, it appears that coupling dampens the ability for highly anisotropic spins to couple to vibrational modes when dipolar coupled. The spectrum for **1** is rich with features with similar intensities across the spectrum. However, the lowest energy transitions for **2** and **3** are very weak compared to higher energy features, and these features are overall less common. When operating under the assumption that the observed coupling persists under an applied field, this discrepancy is consistent with the trend expected from spectroscopic selection rules. Absorption is only "allowed" for $\Delta m_J = \pm 1$; the probability of an event decreases as the moment becomes larger. When the origin state is ferromagnetically coupled, as the ground state of **2** and **3** are, the change in moment between it and any other state is drastically increased; while

we cannot definitively conclude so here, the possible ability of coupling to quench the ability of molecular vibrations to induce relaxation is of great interest in future systems.

3.8 Conclusions

We have herein demonstrated the ability to finely control magnetic states through the dipolar interaction; furthermore, we have built upon design criteria in molecular magnetism by dissecting the effects of the local magnetic environment through varied and extensive characterization. The two dinuclear complexes display how enforcing collinearity between axially anisotropic ions maximizes the strength of the ferromagnetic interaction between them. This strength is important not to create a well-isolated ferromagnetic ground state, but to enhance the single-ion anisotropy through dipolar-induced exchange biasing. Juxtaposed against the mononuclear complex **1**, the parallel arrangement of ferromagnetically coupled spins in **2** and **3** are enough to suppress adiabatic QTM transitions.

A combination of computational and experimental techniques suggests that introducing the tool of controlled dipole-dipole design strategies has the potential to expand beyond a strategy for increasing magnetic relaxation times and become a generalized method for manipulating quantum manifolds of states and the transition state space that governs their stimulus response and approach to equilibrium. Our results show how dipole-dipole coupling is a natural extension of single-ion design, offering an energy-scale independent means of modifying current state-of-the-art ideas in crystal field control. The ground states across our series are highly anisotropic which, when aligned favorably, effectively quench QTM relaxation pathways within coupled multiplets. FIRMS measurements further reveal the effects of inter-KD mixing, as output states can be visualized by their relative moments to the ground state when in proximity to a vibrational mode. Additionally,

transitions in **2** and **3** appear to have drastically decreased intensities, implying that the high-moment ground states impede vibronic coupling.

Acknowledgements

4.1 Introduction

Design principles in molecular magnetism have evolved greatly in the relatively short time since its inception. From a top-down perspective, the ability to control spin-lattice relaxation behavior is advantageous in designing new technologies in fields such as spintronics[168–172] and sensors[173,174]. Approaching it from the bottom-up, such control has been realized with well-refined synthetic design principles in the single-ion case with lanthanide systems even to liquid nitrogen temperatures.[37,39] Furthermore, understanding continues to grow regarding the interaction of anisotropic spins with the vibronic environment,[33,124,125,138,161–164,175,176] allowing for the fine-tuning of the energy landscape down to sub-Kelvin scales. While examples of fantastic success become more common, design principles guiding the next step in a building-block approach[72] – coupling multiple spins together toward the formation of functional materials – are less well-defined.

Interest in coupling multiple anisotropic spins is rapidly growing, encompassing a diverse range of dinuclear molecular magnets,[59,115,177–181] several multi-metal clusters,[88,99,154,156,182,183] and a handful of extended magnetic materials[184–189]. One design paradigm attempts to isolate polynuclear structures bearing strong exchange interactions between spin centers, with the most successful examples arising from spin-bearing bridging ligands[65,68,70,129,190] and directly confining an electron within overlapping orbitals on multiple spin centers.[64,127] However, such design comes at a cost. Successful design in the lanthanide single-ion case has been strongly driven by taking advantage of the relatively weak crystal field perturbation acting upon high moment spin-orbit coupled states. The use of charge-dense and deeply-penetrating radical ligands to impart strong orbital exchange interactions is challenging to implement cooperatively with this design. Between

deleterious crystal field environments limiting anisotropy, increased orbital overlap diminishing the efficacy of first-order perturbations as a model, and large coupling interactions leading to possible mixing in previously well separated magnetic multiplets, success in isolating performant exchange coupled systems, especially from a building block approach, has been difficult.

In contrast to very strong coupling, smaller perturbations have been shown to allow fine control of the magnetic landscape with measurable effects that are more amenable to an iterative design process.[191] Of these small interactions, dipolar coupling is an ideal candidate for carefully manipulating magnetic states and building intuition of the resultant effects. Ground states in lanthanides molecular magnets are highly axially anisotropic, allowing them to be treated as semiclassical point dipoles. Thus, the output states representing different orientations of these dipoles have their energy modified as equation 4.1:

$$E_{dip} = \frac{\mu_0}{r^3}\left(\mu_1 \cdot \mu_2 - 3\frac{(\mu_1 \cdot \vec{r})(\mu_2 \cdot \vec{r})}{r^2}\right) \qquad \text{Eqn. 4.1}$$

where μ_1 and μ_2, the magnetic moments along the principal axis, are governed by single-ion synthetic design principles, and r, the internuclear vector, is structurally defined.

We have previously described the ErCOT subunit[74,73] (composed of Er^{3+} bound to the cyclooctatetraene dianion, COT^{2-}) and the capacity to direct its ground state anisotropy along the metal-ligand centroid vector. Such structural design has allowed for the deliberate manipulation of anisotropy vectors to directly control the dipolar interaction[75] and subsequently observe the effect in magnetic relaxation behavior.[113] Such examples have employed a variety of crystal field environments opposite the COT^{2-} ligand, and consequently the environment surrounding excited states has varied considerably.[50,51,53,134] While behavior arising where the effective suppression of quantum tunneling of magnetization (QTM) within the *ground* state is relevant has been well described in the examples above, the capacity for highly anisotropic *excited* states in ErCOT

complexes to couple via the dipolar interaction has not yet been described in the context of relaxation behavior. Herein, we describe a series of approximately inversion symmetric halide-bridged Er^{TMS}COT (^{TMS}COT = 1,4-bis(trimethylsilyl)cyclooctatetraene) complexes. The isostructural series differs only by the charge density of the isolobal bridging ligands, allowing us to effectively isolate the effect of the crystal field environment on magnetic coupling. The three complexes bear high anisotropy in their ground and first excited states, allowing us to describe their behavior using a simple perturbation model wherein well separated states are allowed to couple separately without mixing ground and first excited single-ion levels.
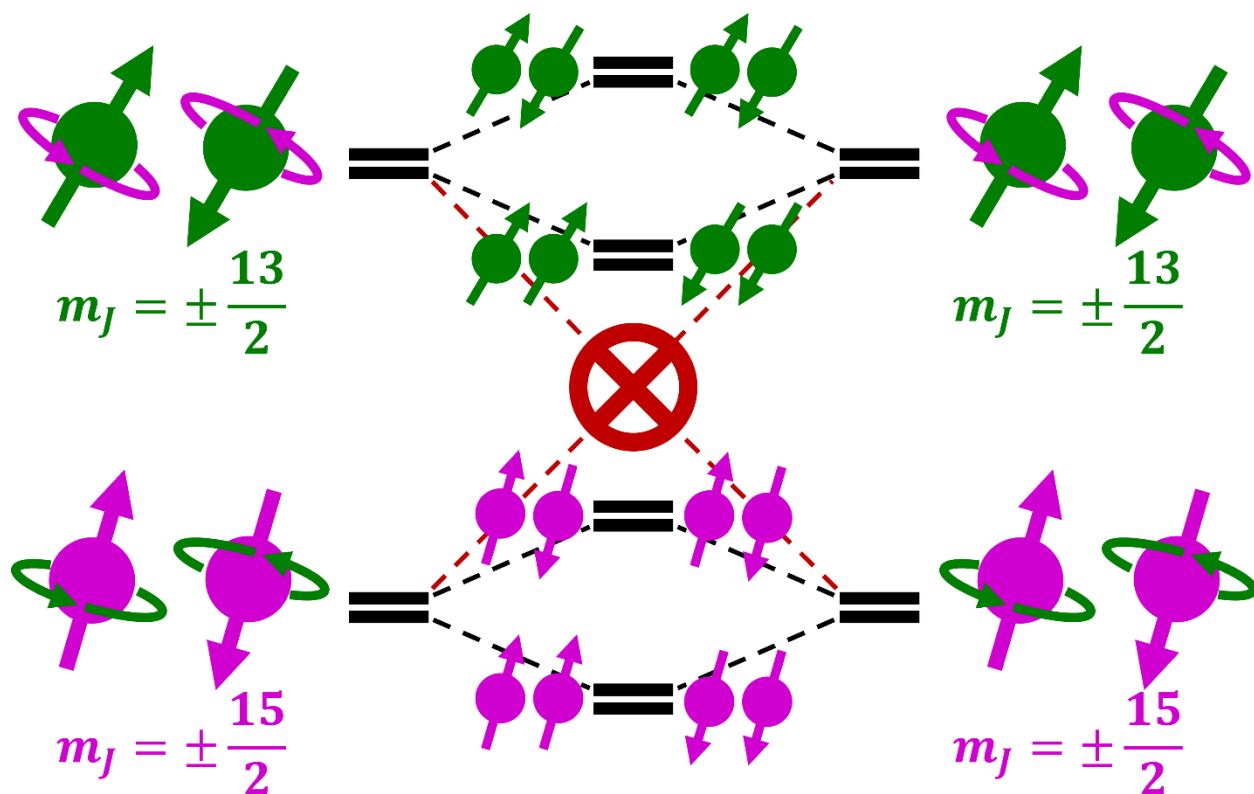
Figure 4.1: Representative schematic of dipolar coupling within the lowest two energy levels in ErCOT systems. High-anisotropy states that are well separated in energy can be modeled as coupling separately, with minimal mixing occurring between them.

4.2 General Methods

General synthetic considerations

All manipulations were carried out under anaerobic, anhydrous conditions under an atmosphere of nitrogen gas using standard Schlenk line and glovebox techniques. Pentane, toluene, and tetrahydrofuran (THF) were dried on activated alumina columns and stored over a 1:1 mixture of 3 and 4 Å molecular sieves for at least two days before use. ErI_3, $ErCl_3$, GdI_3, $GdBr_3$ and $GdCl_3$ powders were purchased from Alfa Aesar and Strem Chemicals; ammonium bromide (NH_4Br), ammonium chloride (NH_4Cl), trimethylsilyl-chloride (TMSCl) tetramethyethylenediamend (TMEDA), n-buthyllithium (n-BuLi), cyclooctadiene (COD), and cyclooctatetraene (COT) were purchased from Aldrich; TMEDA, n-BuLi, COD, and COT were used as received, and ammonium bromide and chloride were heated under vacuum to dry. Dipotassium cyclooctatetraenide,[48] (η^8-cyclooctatetraenyl)-iodo-bis-tetrahydrofuran-erbium[73] and benzyl potassium[135] were prepared via previously reported methods. Elemental analyses were conducted by Midwest Microlab, Indianapolis, IN. Dilutions into isostructural yttrium congeners were performed by mixing a 95:5 molar ratio of Y^{3+}-based and Er^{3+}-based congeners of **1**, **2**, and **3** in THF, removing THF via vacuum, then recrystallization from aromatic solvents in an attempt to isolate matrices with only one Er^{3+} center per dinuclear unit.

<u>Synthesis of 1,4-bis(trimethylsilyl)-cycloocta-2,5,7-triene</u>

The following synthetic procedure was adapted from previous work by Burton et al.[192] *From cyclooctadiene:* Hexane solutions of COD (5 mL, 40.8 mmol), TMEDA (18.32 mL, 122.3 mmol, 3 eq), and n-BuLi (76.93 mL, 1.6 M, 123.1 mmol, 3 eq) were prepared in separate Schlenk flasks and cooled to −78 °C under argon. The cooled pale-yellow n-BuLi solution was added to the stirring cooled colorless COD solution via cannula, and the cooled TMEDA solution was added via cannula immediately afterward. The mixture was then warmed to 0 °C and allowed to warm slowly to room temperature in a thawing ice bath overnight, during which time the solution became

a vivid blood orange. After approximately 16-24 hours, the solution was again cooled to −78 °C. To this cooled solution was added a −78 °C colorless hexane solution of TMS-Cl (18.62 mL, 146.7 mmol, 3.5 eq) via cannula, upon which it rapidly became yellow. The solution was again warmed to 0 °C and allowed to warm to room temperature overnight, during which time it became an off-white suspension. After approximately 16-24 hours, the solution was cooled again to 0 °C and opened to air and began to evolve a white smoke. Once the smoking finished, the mixture was added slowly to a stirring ice water bath. The resultant mixture was added to a separation funnel, where it separated into a pale yellow organic layer and a very slightly colored aqueous layer with a brown residue insoluble in either remaining at the interface. After draining the aqueous layer, the organic layer was washed with 5x100 mL DI H_2O. The organic layer was then dried over $MgSO_4$ and filtered, removing the drying agent and the brown residue. The filtrate was dried on a rotary evaporator, yielding a waxy yellow crude product. (If an oil persists, further washes with H_2O can help remove excess TMEDA, but can also still be worked up without doing so). To this residue was added dry methanol at room temperature until a cloudy mixture is formed. The mixture was cooled to −16 °C, and the yellow solution was filtered away from the resultant colorless/white crystals. Persistent colored impurities were washed away with cold methanol. These crystals were dried, introduced into an air-free environment and recrystallized from minimal pentane at −50 °C to yield colorless crystals of 1,4-bis(trimethylsilyl)-cycloocta-2,5,7-triene; the solution freezes completely at high concentrations, so multiple crops were collected form a slightly diluted solution. These crystals are air sensitive, and a brown colored decomposition product will slowly appear over several hours if left under ambient conditions. Yield: 4.9559 g (19.78 mmol, 48.53%).

From K_2COT: A K_2COT solution (2.0454 g, 11.217 mmol) was prepared according to previous methods by stirring COT over solid potassium in THF under air-free conditions. The solution was

cooled to −40 °C. To this cooled solution was added dropwise a cold solution of (4.983 mL, 39.25 mmol) TMS-Cl in THF. Over the next three hours, the brown solution became off-white. This solution was centrifuged at 3000 rpm, and the pellet was washed several times with pentane. The combined mother liquors were dried under vacuum and then redissolved in pentane. Crystals grew at −40 °C within an hour, yielding highly pure colorless/white crystals of 1,4-bis(trimethylsilyl)-cycloocta-2,5,7-triene. Yield: 928.0 mg (3.70 mmol, 33.0 %).

Synthesis of (η8-1,4-bis(trimethylsilyl)-cyclooctatetraenyl)-erbium-iodide-bis(tetrahydrofuran) and bis((η8-1,4-bis(trimethylsilyl)-cyclooctatetraenyl)-erbium-(μ-iodido)-tetrahydrofuran) **(3)**

Small scale in glove box: The following synthetic procedure was adapted from previous work by Lorenz et al.[167] Tetrahydrofuran mixtures of 1,4-bis(trimethylsilyl)-cycloocta-2,5,7-triene (520.3.8 mg, 2.077 mmol), erbium iodide (1.2488 g, 2.2791 mmol, 1.1 eq), and benzyl potassium (540.9 mg, 4.152 mmol, 2 eq) were prepared and cooled to −40 °C in the glove box freezer. The red benzyl potassium solution was added dropwise to the stirring pale yellow bis(trimethylsilyl)-cycloocta-2,5,7-triene solution, slowly changing color to a more substantial yellow color upon finishing the addition. This solution was stirred for 30 minutes at room temperature, then returned to the freezer to cool to −40 °C. The yellow solution was then added at a "fast dropwise" rate to the stirring ErI$_3$ suspension; the resulting yellow mixture was allowed to stir overnight, slowly changing to a vibrant pink over the course of about 10-30 minutes. The pink mixture was centrifuged after 24 hours, yielding a white pellet and clear pink mother liquor which was decanted away and dried under vacuum. The waxy solid was redissolved in THF, filtered, and layered with pentane at −40 °C to yield vibrant pink crystallographically suitable plank crystals. Yield: 1.2209 g (1.7775 mmol, 85.59 %). Crystals of of **3** were obtained by dissolving the half-sandwich into toluene at 50 °C, filtering the resulting solution, and performing a vapor diffusion with pentane at

85

room temperature to yield peach-colored plates. EA: Calc: 35.17% C, 5.25% H, 0% N; Meas: 35.20% C, 5.47% H, 0% N.

Large scale on Schlenk line: Synthetic procedure was adapted from previous work by Lorenz et al.[167] Tetrahydrofuran mixtures of 1,4-bis(trimethylsilyl)-cycloocta-2,5,7-triene (1.4996 g, 5.786 mmol), erbium iodide (3.4855 g, 6.361 mmol, 1.1 eq), and benzyl potassium (1.5098 g, 11.590 mmol, 2 eq) were prepared in the glove box, transferred to a Schlenk line, and cooled to −78 °C in a dry ice/acetone/isopropyl alcohol bath. The red benzyl potassium solution was added via cannula to the stirring pale yellow bis(trimethylsilyl)-cycloocta-2,5,7-triene, and the resultant dark yellow solution was warmed to 0 °C and allowed to stir for 30 minutes. After being cooled back to −78 °C, this solution was then added to the stirring ErI_3 solution which quickly turned a vibrant yellow. The mixture was then placed in an ice bath and allowed to stir overnight, gradually warming to room temperature. The resultant pink mixture was filtered through a frit with celite, and the filtrate was dried under vacuum. The crude waxy solid was brought into a glovebox, where it was recrystallized via the diffusion of pentane into THF at −40 °C to yield vibrant pink planks identical to those obtained in the small-scale procedure. Yield: 2.8321 g (4.1231 mmol, 71.26%).

Synthesis of (η8-1,4-bis(trimethylsilyl)-cyclooctatetraenyl)-erbium-chloride-bis(tetrahydrofuran) and bis((η8-1,4-bis(trimethylsilyl)-cyclooctatetraenyl)-erbium-(μ-chlorido)-tetrahydrofuran) **(1)**

Synthetic procedure is similar to that of **3** when performed at small scales in a glove box. Tetrahydrofuran mixtures of 1,4-bis(trimethylsilyl)-cycloocta-2,5,7-triene (269.4 mg, 1.075 mmol), erbium chloride (322.3 mg, 1.178 mmol, 1.1 eq), and benzyl potassium (280.8 mg, 2.156 mmol, 2 eq) were prepared and cooled to −40 °C in the glove box freezer. The benzyl potassium solution was added dropwise to the stirring pale yellow 1,4-bis(trimethylsilyl)-cycloocta-2,5,7-triene solution, which rapidly changed to a clear dark yellow color. This solution was allowed to

stir for 30 minutes, after which it was cooled back to −40 °C in the glove box freezer. The cooled solution was then added quickly to the cold stirring $ErCl_3$ mixture. The solution initially turns a vibrant yellow, then may shift to a pale green color as it warms to room temperature. After stirring overnight, the solution changes to a vibrant pink (if pure) or orange/peach (in the presence of impurities). This solution was centrifuged at 3000 rpm and the mother liquor was removed and dried under vacuum. The half-sandwich was isolated as a pink crystalline solid by diffusion of pentane into a filtered THF solution of the product at −40 °C. Yield: 521.9 mg (0.877 mmol, 81.5%). The dinuclear **1** was isolated as a pink crystalline solid by dissolving the product in toluene at room temperature and layering the resulting filtered solution with pentane at room temperature or −40 °C. EA: Calc: 41.31% C, 6.16% H, 0% N; Meas: 41.21% C, 6.15 H, 0% N.

Synthesis of benzyl-(η8-1,4-bis(trimethylsilyl)-cyclooctatetraenyl)-erbium-bis(tetrahydrofuran)

Tetrahydrofuran solutions of **3** as a pink solution (285.1 mg, 0.415 mmol) and benzyl potassium as a deep red solution (54.6 mg, 0.420 mmol) were cooled to −40 °C. The cold benzyl potassium solution was added dropwise to the stirring solution of **3**, immediately forming a bright pink suspension. After being allowed to stir for 1 hour, the solution was centrifuged at 3000 rpm to yield a bright pink solution and white pellet. The mother liquor was removed and dried under vacuum to yield a bright pink solid. This solid was redissolved in minimum THF, filtered, and worked up by the diffusion of pentane into the solution at −40 °C to yield bright pink crystals of the half-sandwich compound. Yield: 181.2 mg (0.279 mmol, 67.2%). EA:

Synthesis of (η8-1,4-bis(trimethylsilyl)-cyclooctatetraenyl)-erbium-bromide-bis(tetrahydrofuran) and bis((η8-1,4-bis(trimethylsilyl)-cyclooctatetraenyl)-erbium-(μ-bromido)-tetrahydrofuran) **(2)**

Tetrahydrofuran mixtures of benzyl-(η8-1,4-bis(trimethylsilyl)-cyclooctatetraenyl)-erbium-bis(tetrahydrofuran) as a pink solution (181.2 mg, 0.281 mmol) and NH_4Br as a suspension

of white solid (27.5 mg, 0.279 mmol) were cooled to −40 °C. The cold solutions were quickly mixed while stirring and allowed to stir overnight while warming to room temperature. A small amount of white precipitate formed. After filtration, the resultant bright pink solution was dried, redissolved in tetrahydrofuran, and isolated by the diffusion of pentane at −40 °C to form bright pink crystals of the half-sandwich. Crystals of dinuclear **2** were obtained by dissolving the half-sandwich into toluene at 50 °C, filtering the resulting solution, and performing a vapor diffusion with pentane at room temperature to yield peach-colored plates. Yield: 99.1 mg (0.0872 mmol, 62.6 %). EA: Calc: 38.08% C, 5.68% H, 0% N; Meas: 37.88% C, 5.79% H, 0% N. This procedure is also able to be performed with NH_4Cl to yield **1 or** NH_4I to yield **3**, albeit at a lower yield than the reported procedures.

Physical Measurements

Single crystal X-ray data for all compounds, unless otherwise noted, were collected at 100 K on single crystals immobilized in Paratone on a Bruker κ(α) Diffractometer with a Mo Kα radiation source and an Apex II Area Detector. The structures were solved using direct methods via the SHELXT routine and refined using full-matrix least-squares procedures with the SHELXL[105] routine. Olex2 was used as a graphical front-end.[106] Hydrogens were modelled using a riding model for non-bridging carbon positions.

Powder crystal X-ray data for all compounds were collected at 100 K on a Bruker κ(α) Diffractometer with a Mo Kα radiation source and an Apex II CCD Area Detector. Dried samples were ground, covered in paratone oil, and mounted onto a standard loupe and immediately moved under a cold nitrogen stream to freeze. Powdered diffraction patterns were compared to calculated patterns from the Mercury visualization software. PXRD patterns are provided for all paramagnetic

species; yttrium-based compounds have bulk purity determined by nuclear magnetic resonance instead.

Magnetic analyses were conducted with a Quantum Design MPMS3 SQUID Magnetometer running in DC scan mode. All samples were loaded in custom quartz tubes (D & G Glassblowing Inc.) and sealed under static vacuum. Eicosane wax was added to each sample. After sealing, the eicosane was melted to minimize torquing and ensure good thermal conductivity during measurements. All static susceptibility data were corrected for diamagnetic contributions from eicosane and the samples themselves using Pascal's constants.[107] DC susceptibility measurements were collected with H_{DC} = 200 Oe. Isothermal magnetization data was either collected by allowing the sample to equilibrate at steps at an average sweep rate of H_{dc} = 10 Oe/s or by sweeping the field in VSM mode at a rate of H_{dc} = 20 Oe/s. Zero-field AC susceptibility studies for all compounds were conducted between 0.1–1000 Hz (H_{dc} = 0 Oe, H_{AC} = 2 Oe). Zero-field DC waveform techniques were applied according to our previous methods[60,113] and analyzed using the SUPER computational package in MatLab for frequencies below 0.1 Hz.[193]

Baseline-corrected solid-state FT-IR spectra were collected on crystalline samples with a Bruker ALPHA II diamond-anvil ATR spectrometer (32 scan average, 2 cm^{-1} resolution) inside an N$_2$-atmosphere glovebox.

Computational Methods

All single-ion calculations were performed using the SEWARD / RASSCF / RASSI / SINGLE_ANISO modules of OPENMOLCAS.[153] Input atom coordinates were taken from molecular geometries from crystallographic data. (In dinuclear structures, one erbium center was replaced with closed-shell yttrium. Solvent molecules were not included in the calculations to lower computation time. Basis sets of the ANO-RCC type were used and the quality of the specific

basis function was selected based on the proximity of the atom to the metal (**Er:** ANO-RCC-VTZP; **atoms bound to Er:** ANO-RCC-VDZP; **all other atoms:** ANO-RCC-VDZ). Two-electron integrals were Cholesky decomposed (10^{-6} cutoff) to speed up calculations and save disk space. A CAS(11,7) was selected for the complete active space self-consistent f ield (CASSCF) procedure and in this space we included 35 CI roots of spin multiplicity 4 and 112 CI roots of spin multiplicity 2. All RASSCF module output wavefunctions were used to compute the spin-orbit matrix elements by the RASSI module. The RASSI module output was directed to SINGLE_ANISO for magnetic properties calculations. Outputs from SINGLE_ANISO were used as is for single-ion descriptions, and were used with POLY_ANISO to describe coupling.

All coupling calculations for **1, 2** and **3** were performed using the POLY_ANISO module of OPENMOLCAS.[154–156] Each magnetic center was approximated as an Ising spin, and computations were performed employing the Lines model for anisotropic exchange coupling. Input files called upon by the module were obtained as outputs from the SINGLE_ANISO calculations performed above. A**s** each compound has two distinct magnetic centers after geometry optimization, no symmetry-generated centers were used in such cases. Only the lowest energy doublet for each center was considered, and thus four states representing two pseudospin-½ doublets were computed. Dipolar interactions were calculated explicitly using *g* tensors obtained from SINGLE_ANISO.

Manual calculations of the dipolar interaction were performed with an in-house MatLab code using inputs directly taken from SINGLE_ANISO. The mathematical description of the employed method is included in the Appendix; it is an adaptation of the same methods used in the POLY_ANISO module.

4.3 Magnetostructural Description

Compounds **1**, **2**, and **3** are approximately inversion-symmetric halide-bridged dinuclear structures of the general formula [Er($^{1,4\text{-TMS}}$COT)(μ-X)(THF)]$_2$ (X = Cl (**1**), Br (**2**), I (**3**); THF = tetrahydrofuran). All three are synthesized by the deprotonation of 1,4-bis(trimethylsilyl)-2,5,7-cyclooctatriene followed by the addition of the appropriate dry erbium trihalide salt in dry, air-free THF. The resulting piano-stool complexes Er($^{1,4\text{-TMS}}$COT)(X)(THF)$_2$ can be isolated from the reaction solvent; upon rigorous removal of one stoichometric equivalent of and any residual THF, the inversion-symmetric dinuclear structures **1**, **2**, and **3** can be recrystallized from aromatic solvents.
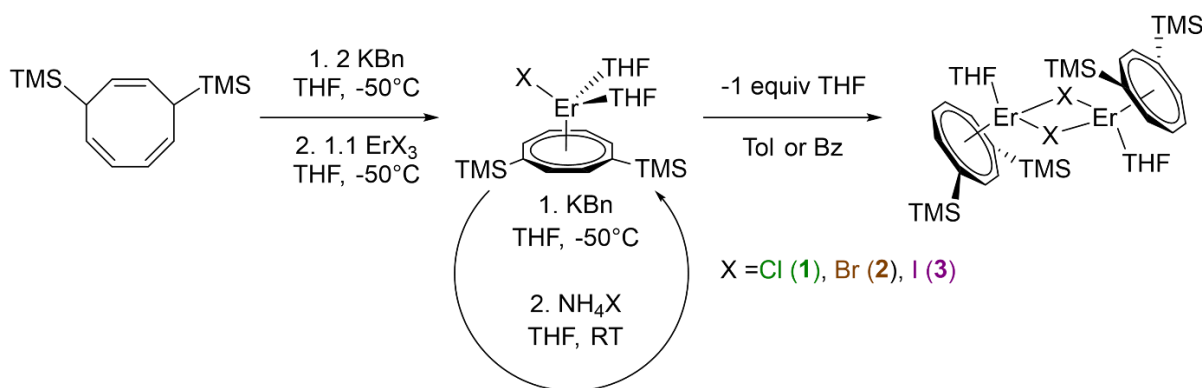
Scheme 4.1: Representative synthetic route to and between **1**, **2**, and **3**

All three compounds bear very similar structural environments. Complexes bearing Er^{3+} bound to a COT^{2-} derivative have their ground state anisotropy effectively pinned to the Er-centroid vector $\vec{r}_{ErCOT}$. The length of $\vec{r}_{ErCOT}$ is nearly identical in **1**, **2**, and **3** at 1.74 Å, suggesting a similar level of stabilization imparted by the ring. Similarly, the THF ligand on all metal centers across the series have bond distances and angles relative to $\vec{r}_{ErCOT}$ within 0.05 Å and 1°, respectively, implying that it, too, exerts a similar effect on the crystal field environment for **1**, **2**, and **3**. Thus, the only significant differences between the three complexes arise from the differing ionic radii of the bridging halide and the consequential structural parameters (Table 4.1). The Er-

X bond lengths are consistent with the sum of the effective ionic radii of Er^{3+} and X^-, implying an almost entirely ionic interaction between the two. Furthermore, the intramolecular Er-Er distance increases from **1** to **3** in accordance with the radii of their bridging ions. The angles describing the orientation of $\vec{r}_{ErCOT}$ for each metal center relative to the other and relative to the internuclear vector are key handles to describing the dipolar interaction. For all three complexes, $\vec{r}_{ErCOT}$ for both metal centers are oriented approximately parallel to one another, and $\vec{r}_{ErCOT}$ forms a similar angle to the internuclear vector across the series.
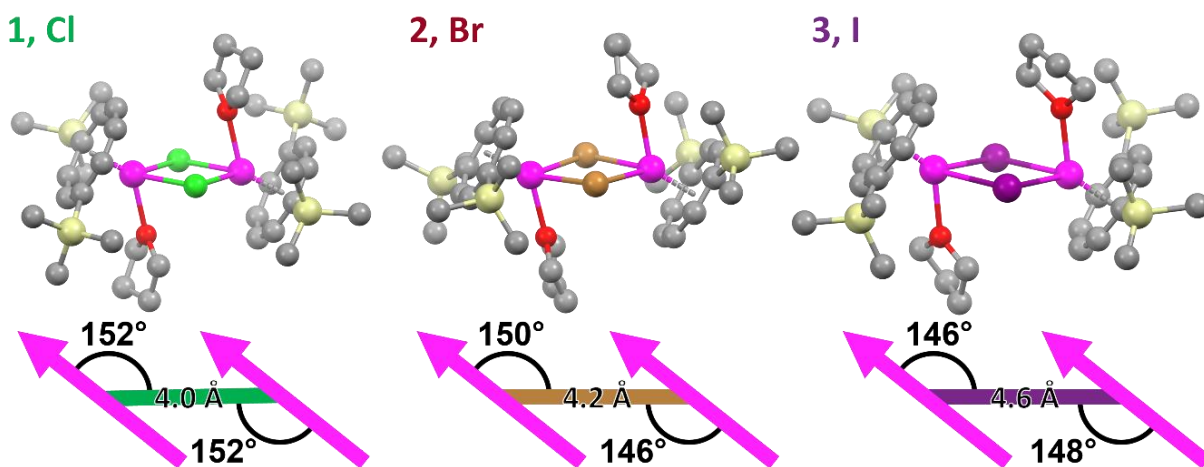
Figure 4.2: Crystallographic structures (top) and abbreviated description (bottom) of the bridging geometries for **1**, **2**, and **3**. Pink arrows represent r_{ErCOT}, lines connecting them represent the internuclear vector, and angles are the angle between these vectors as described crystallographically

The magnetic behavior for **1**, **2**, and **3** are therefore expected to differ primarily due to the nature of the bridging halide. The different crystal field environments should principally affect single-ion properties, such as state separation and purity. The inter-metal separation primarily dictates the strength of the intramolecular dipolar coupling, whose energy falls off as the cube of the internuclear distance. As all three complexes are predicted to bear parallel magnetic anisotropy axes that are also at shallow angles with the internuclear vector, the ground states of the two metal centers are expected to ferromagnetically couple.

Table 4.1: Selected averaged structural parameters from **1**, **2**, and **3**

	1	2	3
r_{12}	3.9807(5) Å	4.2431(8) Å	4.5767(7) Å
r_{ErCOT}	1.7293(5) Å	1.741(5)Å	1.7370(14) Å
r_{Er-X}	2.681(4) Å	2.862(9) Å	3.106(11) Å
θ_{12}	178.75(2)°	175.85(2)°	176.9(2)°
θ_{1-int}	151.798(17)°	149.75(3)°	146.265(14)°
θ_{2-int}	151.881(17)°	145.60(3)°	147.674(18)°

4.4 Magnetic Properties

To probe the effect of changing the halide bridge on magnetic behavior across the series, static and dynamic magnetic properties of **1**, **2**, and **3** were measured in a Quantum Design MPMS3 SQUID magnetometer on ground microcrystalline samples immobilized in eicosane. Zero-field cooled (ZFC) and field-cooled (FC) variable temperature magnetic susceptibility measurements were performed under a 200 Oe field to see the effect on state population. At 300 K, experimental ZFC $\chi_M T$ values for **1**, **2**, and **3** are consistent with theoretical values for two uncoupled Er^{3+} ions (22.7, 23.0, and 22.3 emu K mol^{-1} **1**, **2**, and **3**, respectively; $J = 15/2$, $g = 6/5$ per ion; 11.48 emu K mol^{-1} per Er^{3+}).[3] As the temperature decreases, $\chi_M T$ decreases accordingly consistent with the thermal depopulation of anisotropic magnetic states. At low temperatures (**1**, 20.5 K; **2**, 13 K; **3**, 17 K), a local minimum is reached, and $\chi_M T$ increases sharply to a maximum (25.2, 20.5, and 23.3 emu K mol^{-1} for **1**, **2**, and **3** at 2, 2.2 , and 4.2 K, respectively) before dropping precipitously in **2** and **3**. For **2** and **3**, $\chi_M T$ values in FC measurements deviate from those extracted from ZFC below this maximum, which is a common indicator of magnetic blocking on the timescale of the measurement. This metric is heavily dependent on the temperature sweep rate, however, so we eschew it in favor of dynamic measurements in regard to determination of a blocking temperature.

Isothermal DC magnetization curves were collected at between −7 and 7 T at a sweep rate of 20 Oe/s for each compound, and isothermal vibrating sample magnetometry (VSM)

measurements were collected at 10 Oe/s to corroborate them. At 2 K, magnetization curves for **1** and **2** show only very slight, if any, hysteretic behavior. Both show very slight openings near zero field, with coercive fields less than 1000 Oe (the point density of the measurement was not sufficient to adequately extract this in DC measurements, and noise in VSM measurements obscures observing this opening). The magnetization in **3**, however, displays clear hysteretic behavior. The coercivity is observed to be between 1000 Oe and 1500 Oe in DC experiments, and VSM measurements place this field at 1350 Oe. Furthermore, inflection points, or "steps," in the hysteresis curve are visible near 1000 Oe. These are attributed to QTM events near avoided crossings of magnetic states;[194] such avoided crossings are especially common in compounds with small coupling barriers.
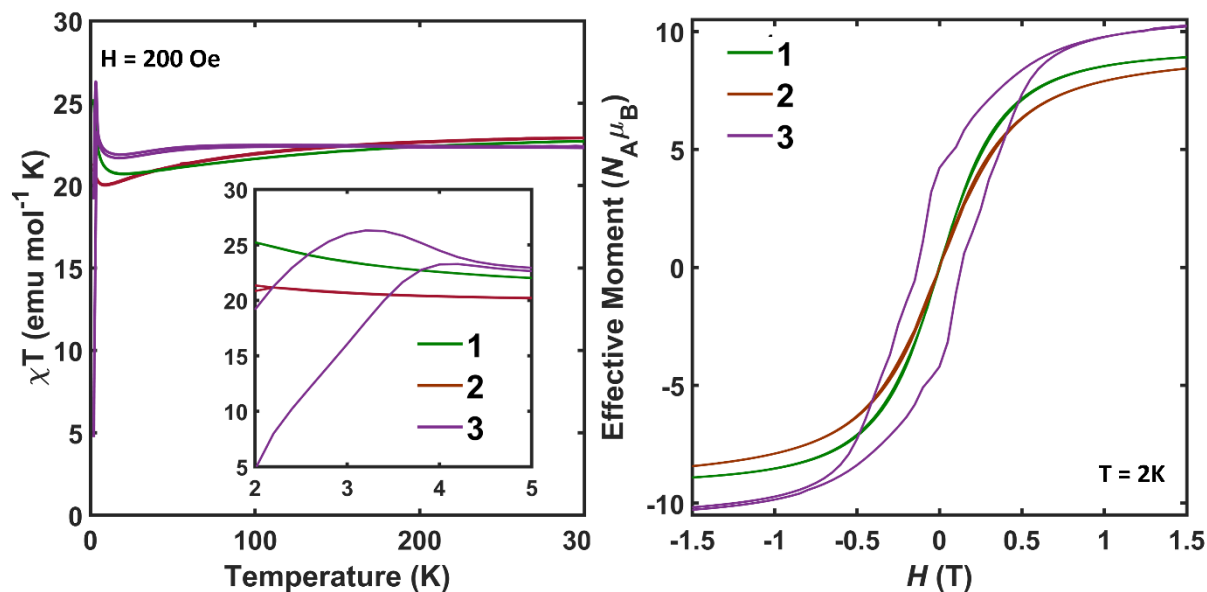
Figure 4.3: DC magnetic measurements for **1**, **2**, and **3**. (Left) Temperature-dependent susceptibility measurements with both ZFC and FC sweeps. (Left inset) zoomed lowest-temperature region of ZFC and FC sweeps showing presence or lack of splitting. (Right) Field-dependent DC magnetization measurements collected at 10 Oe/s.

To extract characterization relaxation times (τ) associated with zero-field demagnetization rates, frequency-dependent AC susceptibility and long-timescale DC waveform[60] measurements were performed. In-phase (χ') and out-of-phase (χ'') susceptibility components were

fit to a generalized Debye equation.[4] For **1** and **2**, χ'' vs frequency curves display one peak each, and plotting χ' vs χ'' forms low-eccentricity semicircles. Thus, only one characteristic relaxation time is observed for each sample. For **1**, two different magnetic species that are crystallographically indistinct can be isolated depending on crystallization and sample preparation conditions. Following the same exhaustive recrystallization conditions at room temperature as done for **2** and **3** yields a sample with longer relaxation times, whereas recrystallization at −50 °C yields a sample with shorter relaxation times that are not consistent with the single-ion. Crystallographically, this may correspond to an increased presence of a 5% disordered position of Er^{3+} observed in some crystallographic datasets. Thus, magnetic datasets representing longer relaxation times for **1** are used for comparison to remain consistent with conditions employed for **2** and **3**, but both sets of data are reported in Table 2 to reflect their description of **1**. For **3**, two peaks are visible in χ'' vs frequency, and two semicircles are visible in χ' vs χ''. The ratio of the susceptibilities of these peaks changes between samples, implying a change in the ratio of the two species from which they originate, but fits to an extended Debye model yield consistent tau values across those samples.[4,104,195] Given the single unique dinuclear molecule present in the crystallographic asymmetric unit, this implies that the two relaxation processes are associated with two different discrete magnetic environments, which could arise from either sample purity or deviations in crystal defects rather than with two independent magnetic centers inherent to the structure. Across several samples, the slower process was consistently the dominant mechanism. Furthermore, the faster process was significantly suppressed through exhaustive recrystallization from aromatic solvents and drying of the sample. Upon exposure to minimal THF and recrystallization from toluene, the second process reappeared. Thus, this faster process is

associated with incomplete desolvation of THF, and the slower process is taken to be characteristic for **3**.

Plotting fit τ values as $\ln(\tau)$ vs $1/T$ already reveals dramatic differences between **1**, **2**, and **3** (Figure 4.4). Both **1** and **2** display similar relaxation dynamics at high temperatures, and relaxation times for **2** become slightly longer at low temperatures. Compound **3** meanwhile has much longer relaxation times at all temperatures, reflecting its more pronounced hysteretic behavior. All three complexes' relaxation behavior maintains some level of thermal dependence at all temperatures. The differences between the three are most clearly reflected in their maximum relaxation time measured at 2 K (τ_{2K}). For **1** and **2**, τ_{2K} are modest at 3.0(3) s and 4.3(1) s, respectively. In **3**, τ_{2K} increases dramatically to 1790(70) s.
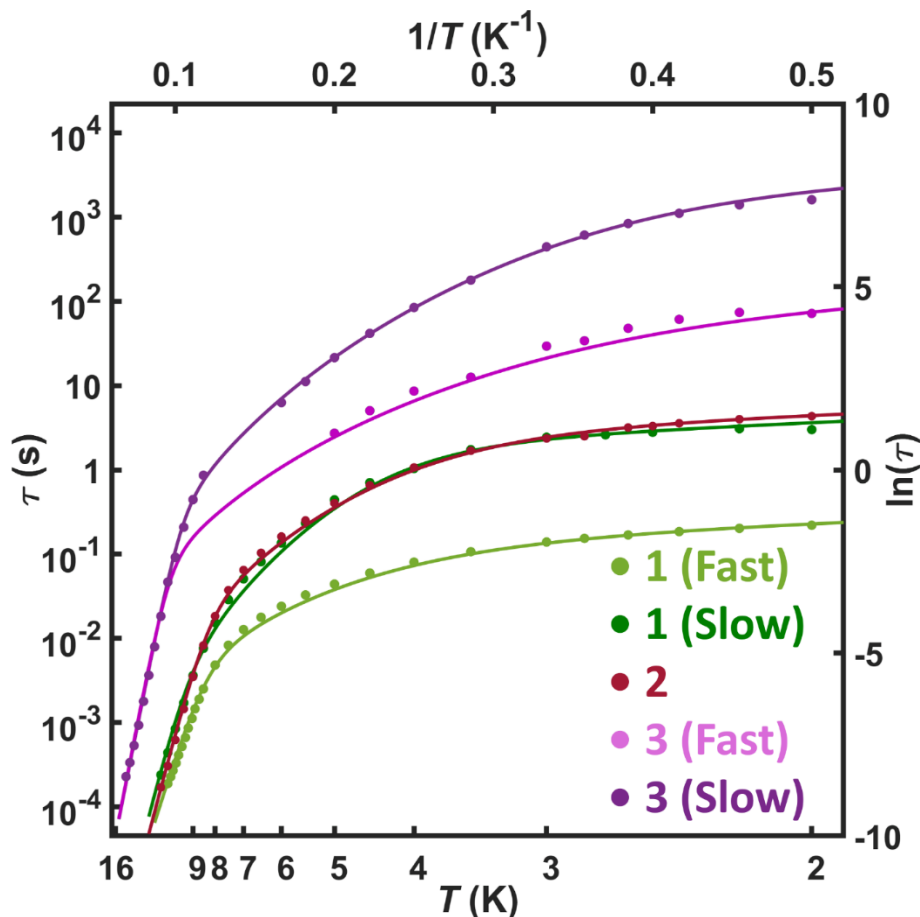
Figure 4.4: Relaxation data extracted from AC susceptibility experiments and fits to equation 4.2

Relaxation behavior for **1**, **2**, and **3** can be described by fitting extracted τ values to a magnetic relaxation equation:

$$\tau^{-1} = \tau_0^{-1} e^{-\frac{U_{eff}}{k_B T}} + C T^n + \tau_D^{-1} e^{-\frac{D_{eff}}{k_B T}} \qquad \text{Eqn 4.2}$$

The first term represents thermal relaxation via an excited magnetic state, where U_{eff} describes this energy gap. The second term describes Raman (or vibronic) relaxation mechanisms involving virtual excited states. The third term represents another thermal relaxation mechanism over the much smaller energy barrier associated with coupled magnetic states represented by D_{eff}. Thus, these phenomenological fit parameters can be used to extract meaningful information about the energy landscape and meaningfully compare these isostructural compounds.[113] Both **1** and **2** appear to have similar relaxation dynamics. The two share very similar effective barriers, whereas U_{eff} for **3** is about 50 cm^{-1} larger. All three complexes have similar secondary barriers of approximately ~1 cm^{-1} caused by coupling. The dramatically different low-temperature relaxation behavior across the series can then instead be described by the dipolar attempt time (τ_D), which increases from 1.4(5) s in **1** to 2.1(6) in **2**, and in **3** increases by two orders of magnitude to 1.4(3)$\times 10^3$ s s. Since all three complexes have approximately the same D_{eff}, τ_D can be considered akin to the rate of the quantum tunneling mechanism (τ_{QTM}) in SIMs in so much that it describes the approximate rate of these small thermal transitions. Thus, the low-temperature dipolar coupled relaxation mechanism dramatically increases across the series from **1** to **3**.

To reinforce the claim that intramolecular dipolar coupling is the primary mechanism suppressing QTM pathways operant at low temperatures, magnetically dilute samples were prepared into an isostructural Y^{3+}-based matrix with the intent of eliminating intramolecular dipolar interactions as well as stray intermolecular fields. While susceptibility and isothermal magnetization experiments demonstrate that dipolar coupling has not been completely removed,

relaxation dynamics have been dramatically affected. While all three have their low-temperature relaxation accelerated, **1** and **3** were observed to most thoroughly have dipolar interactions removed, as their low-temperature relaxation behavior is almost entirely temperature independent. Furthermore, U_{eff} for **1** has increased dramatically, while those for **2** and **3** largely remain the same.

Table 4.2: Relaxation parameters for undiluted and diluted **1**, **2**, and **3**

	1 (fast)	1 (slow)	1 (dil)	2	2 (dil)	3 (fast)	3 (slow)	3 (dil)
$\mathbf{U_{eff}}$	98.7(10) cm^{-1}	122(6) cm^{-1}	138(4) cm^{-1}	116(4) cm^{-1}	109(7) cm^{-1}	157(3) cm^{-1}	153(3) cm^{-1}	147(5) cm^{-1}
$\mathbf{\tau_0}$	3(2) $\times10^{-10}$ s	4(5) $\times10^{-11}$ s	4(2) $\times10^{-12}$ s	4(3) $\times10^{-11}$ s	2(3) $\times10^{-10}$ s	3.4(15) $\times10^{-11}$ s	5(2) $\times10^{-11}$ s	3.2(18) $\times10^{-10}$ s
$\mathbf{C}$	0.026(15)	3(2) $\times10^{-5}$	3.7(4) $\times10^{-5}$	2.7(15) $\times10^{-4}$	4(4) $\times10^{-3}$	2.4(6) $\times10^{-4}$	2.1(4) $\times10^{-6}$	4(3) $\times10^{-5}$
$\mathbf{n}$	4.1(4)	7.1(4)	7.26(5)	5.7(3)	4.9(5)	4.6(2)	6.20(10)	5.3(5)
$\mathbf{D_{eff}}$	1.0(4) cm^{-1}	1.3(6) cm^{-1}	■	1.1(5) cm^{-1}	0.8(2) cm^{-1}	0.9(5) cm^{-1}	1.0(4) cm^{-1}	■
$\mathbf{\tau_D}$ or $\mathbf{\tau_{QTM}}$	0.13(3) s	1.4(5) s	0.1860(4) s	2.2(6) s	0.058(7) s	70(20) s	1.4(3)$\times10^3$ s	2.22(18) s
$\mathbf{\tau_{2K}}$	0.22(6) s	3.0(3) s	0.14(2) s	4.34(10) s	0.106(8) s	66(6) s	1790(70) s	2.2(3) sτ

4.5 Modeling of magnetic states

To describe the origin of the observed magnetic behavior, magnetic energy manifolds of **1**, **2**, and **3** were modeled with the SINGLE_ANISO[153] and POLY_ANISO[154–156] modules of OpenMolcas (Figure 4.5, Table 4.3). When modeling single-ion states of the independent Er^{3+} metal centers in SINGLE_ANISO, the opposite metal position was substituted with the diamagnetic Y^{3+} ion, which is suitable due to its similar ionic radius. Given the ionic nature of the lanthanide-halide bonds as described above, the exchange interaction is expected to be minimal. Thus, only the dipolar interaction was modeled in POLY_ANISO. Furthermore, as will be discussed, the ground Kramers doublet is well isolated from other computed magnetic states. As the dipolar interaction is expected to be at least an order of magnitude smaller than this separation, only the ground Kramers doublet for each center was included in POLY_ANISO.

The uncoupled $J = \frac{15}{2}$ manifolds for each Er^{3+} center across **1**, **2**, and **3** are very similar to each other, differing subtly in energy separation scaling and degree of mixing within each Kramers doublet (Figure 4.5, top). All three compounds have a highly anisotropic ground pseudospin-½ doublet (KD_0) principally composed of the $m_J = \pm \frac{15}{2}$ states with g_z four orders of magnitude larger than g_x or g_y. The first excited doublet (KD_1) is similarly axially anisotropic. For all three complexes, KD_1 is predominantly composed of $m_J = \pm \frac{13}{2}$ with less than 10% $m_J = \pm \frac{7}{2}$ mixed in; this mixing decreases across the series from **1** to **3**, which is attributed to the lower charge density of Br^- and I^- compared to Cl^-. Similarly, the energy gap between KD_0 and KD_1 is largest for **1** and smallest for **3**, as the higher charge density of Cl^- should result in a larger perturbation. While the measured U_{eff} for **1** and **2** are largely consistent with a transition to KD_1, thermal relaxation for **3** appears to proceed through the second excited state, KD_2. With completely rhombic anisotropy, the anisotropy tensor describes the hard axis of KD_2 as lying along the easy axis of the lower two doublets when oriented relative to those of KD_0 and KD_1. Principally consisting of $m_J = \pm \frac{1}{2}$ with some $m_J = \pm \frac{3}{2}$ mixed in, relaxation through the barrier is expected to be rapid within this doublet, consistent with experimental data.
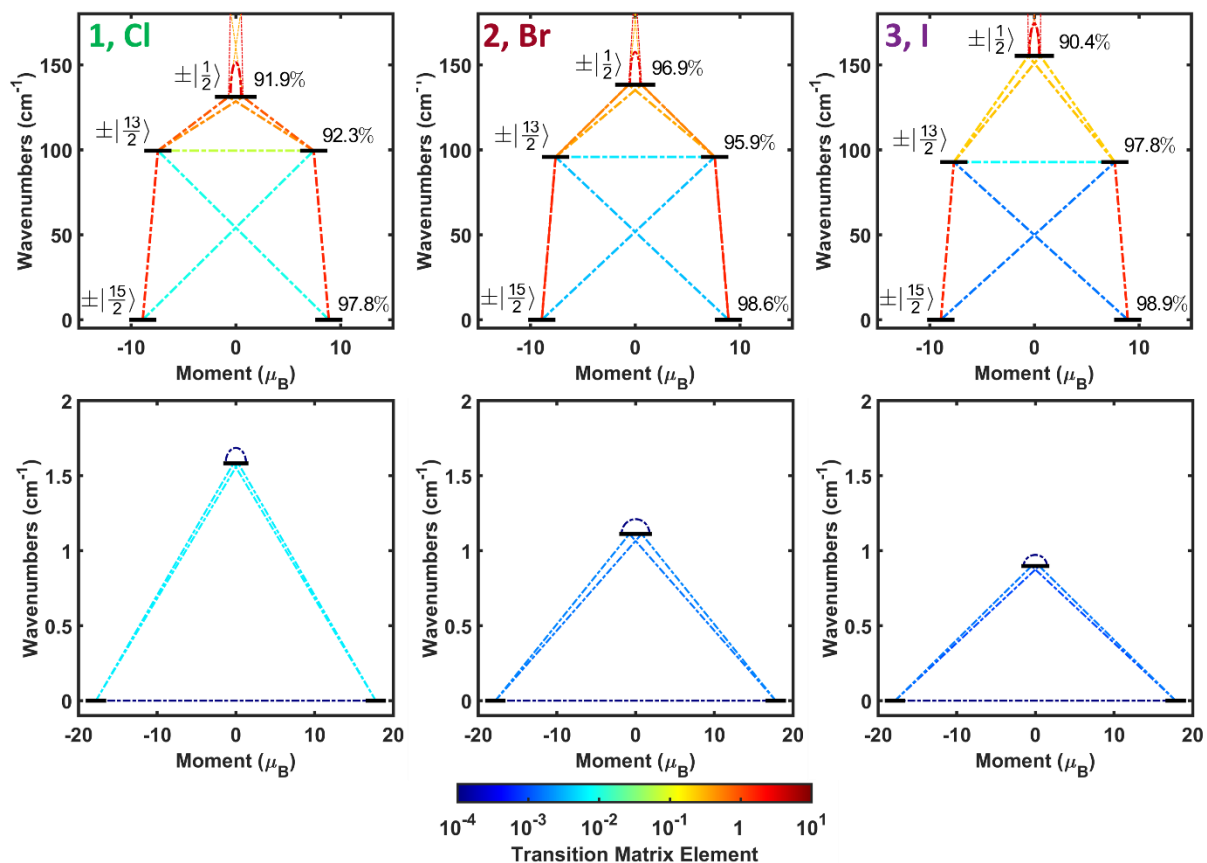
Figure 4.5: Representative SINGLE_ANISO (top) and POLY_ANISO (bottom) output transition matrix elements between calculated states for **1** (left), **2** (center), and **3** (right). QTM transition probabilities from POLY_ANISO are ten orders of magnitude lower than the lowest represented by the color scale. SINGLE_ANISO output states are labeled with the largest m_J contribution.

At low temperatures, relaxation should be limited to pathways within the energy regime of KD_0. Since **1**, **2**, and **3** contain two magnetic lanthanides in close proximity, the local dipolar interaction involving the ground doublets for each was modeled using POLY_ANISO (Figure 4.5, bottom).[154–156] The energy separation between the ferromagnetically coupled ground pseudo-doublet (DD_0) and the antiferromagnetically coupled excited pseudo-doublet (DD_1) decreases monotonically from **1** to **3** in accordance with the increased internuclear distance. For all three, DD_0 is extremely axially anisotropic such that they could be considered pure Ising-type spins. On the other hand, DD_1 has an extremely small moment consistent with the near-exact canceling of

moments in the antiferromagnetic arrangement of spins. The moments and energy separation between these doublets are consistent with the inflection points in hysteresis curves observed near 1000. Within DD_0 and DD_1, relative transition rates between states can be approximated as proportional to the corresponding transition matrix elements due to their degeneracy.[196] After coupling, the output states are no longer half-integer spins, and therefore such matrix elements may not be representative of relaxation. However, for DD_0 and DD_1, the tunneling splitting is vanishingly small, and the pairs of states can therefore be considered doublets where this approximation is still accurate. Transition matrix elements describing QTM mechanisms in both DD_0 and DD_1 are extremely small, and the rate of such a mechanism is expected to be over twelve orders of magnitude slower than any other transition described in SINGLE_ANISO. Thus, QTM within the ground doublet is essentially quenched. Thermal transitions between DD_0 and DD_1 are more likely, with transition matrix elements a few orders of magnitude smaller than those between KD_0 and KD_1 extracted from SINGLE_ANISO. Thus, at high temperatures these higher energy pathways should be more favored. At low temperatures, a two-phonon process involving DD_0 and DD_1 is expected to drive relaxation. The transition matrix elements describing this transition decrease by about five times between **1** and **3**, which may account for its dramatically larger "attempt time" for the dipolar-coupled mechanism τ_D.

Unfortunately, while relaxation in the ground state is well described by the POLY_ANISO outputs, outputs from SINGLE_ANISO alone are not able to account for the differences in relaxation at temperatures where KD_1 and beyond are accessible. When only considering single-ion transition matrix elements, **2** would be expected to relax slower than **1** and **3** at zero field based on transition matrix elements between KD_0 and $KD_1$and between KD_1 and KD_2. Since KD_1

displays easy-axis anisotropy in **1**, **2**, and **3**, coupling in this and further excited states should be accounted for to describe the differences in magnetic properties.

Table 4.3: Calculated energy splittings, anisotropy tensor elements, and transition matrix elements for single-ion and coupled magnetic states of **1**, **2**, and **3**.

Single-Ion	1	2	3
E_{KD0}	0 cm^{-1}	0 cm^{-1}	0 cm^{-1}
$\{g_x \mid g_y \mid g_z\}_{KD0}$	0.00997(4) 0.0158(8) 17.78(1)	0.0027(3) 0.0038(2) 17.831(3)	0.0021(7) 0.0025(10) 17.850(8)
E_{KD1}	98.7(11) cm^{-1}	91(5) cm^{-1}	90(7) cm^{-1}
$\{g_x \mid g_y \mid g_z\}_{KD1}$	0.196(14) 0.24(3) 14.85(3)	0.09(6) 0.13(9) 15.16(3)	0.029(6) 0.024(5) 15.32(5)
E_{KD2}	129(3) cm^{-1}	132(5) cm^{-1}	151(4) cm^{-1}
$\{g_x \mid g_y \mid g_z\}_{KD2}$	10.3(4) 8.3(3) 1.34(5)	11.8(11) 6.9(11) 1.2(1)	12.0(2) 6.7(4) 1.20(5)
Coupled	1	2	3
$\Delta E_{Dip,0,Poly}$	1.583 cm^{-1}	1.112 cm^{-1}	0.898 cm^{-1}
$\{g_x \mid g_y \mid g_z\}_{DD0}$	2.3E-7 | 4.8E-6 | 35.547	1E-12 | 4.8E-7 | 35.627	1E-12 | 6.7E-7 | 35.697
$\{g_x \mid g_y \mid g_z\}_{DD1}$	1E-12 | 3.4E-9 | 0.594	1E-12 | 1E-12 | 1.54	1E-12 | 3.7E-9 | 0.958
$DD_{0+} \rightarrow DD_{1+}$	0.0062	0.0019	0.0017
$DD_{0+} \rightarrow DD_{1-}$	0.0066	0.0016	0.0010
$\Delta E_{Dip,0,manual}$	1.584 cm^{-1}	1.112 cm^{-1}	0.898 cm^{-1}
$\{g_x \mid g_y \mid g_z\}_{DD0}$	0.0139 | 0.0315 | 35.5470	0.0056 | 0.0078 | 35.6268	0.0047 | 0.0056 | 35.6972
$\{g_x \mid g_y \mid g_z\}_{DD1}$	0.0143 | 0.0014 | 0.5941	0.0008 | 0.0007 | 1.5439	0.0010 | 0.0017 | 0.9578
$DD_{0+} \rightarrow DD_{1+}$	0.0059	0.0017	0.0015
$DD_{0+} \rightarrow DD_{1-}$	0.0029	0.0014	0.0010
$\Delta E_{Dip,1,manual}$	0.9332 cm^{-1}	0.7799 cm^{-1}	0.6865 cm^{-1}
$\{g_x \mid g_y \mid g_z\}_{DD0}$	0.3894 | 0.4752 | 29.7022	0.1083 | 0.1787 | 30.3164	0.0419 | 0.0499 | 30.6791
$\{g_x \mid g_y \mid g_z\}_{DD1}$	0.0409 | 0.0591 | 0.6029	0.1357 | 0.2110 | 0.8919	0.0039 | 0.0042 | 0.6031
$DD_{0+} \rightarrow DD_{1+}$	0.1114	0.0731	0.0114
$DD_{0+} \rightarrow DD_{1-}$	0.0986	0.0083	0.0110

As KD_0 and KD_1 are separated by an energy approximately two orders of magnitude larger than that of the dipolar interaction, the dipolar interactions between Kramers doublets are considered independent of one another – i.e., the interactions between KD_1 on both metal centers

is independent of KD$_0$. Thus, working under the assumption that the uncoupled single-ion states are well described as pseudospin-½ doublets with diagonal *g*-tensors describing their magnetic anisotropy, they can be used as inputs in a Hamiltonian describing their interaction:

$$\hat{\mathcal{H}}_{inter} = \hat{\mathcal{H}}_{dip} + \hat{\mathcal{H}}_{Zee} \qquad \text{Eqn. 4.3}$$

Here, $\hat{H}_{dip}$ describes dipolar coupling, as described by equation 4.4:

$$\hat{\mathcal{H}}_{dip} = \frac{\mu_B^2 \mu_0}{r^3}\left(\tilde{S}_1 \otimes \tilde{S}_2 - 3\frac{(\vec{r}^T \cdot \tilde{S}_1)\otimes(\tilde{S}_2 \cdot \vec{r})}{r^2}\right) \qquad \text{Eqn. 4.4}$$

and $\hat{H}_{Zee}$ describes how the two spins interact under an applied field via the Zeeman interaction:

$$\hat{\mathcal{H}}_{Zee} = \boldsymbol{B} \cdot \tilde{S}_1 \oplus \boldsymbol{B} \cdot \tilde{S}_2 \qquad \text{Eqn. 4.5}$$

In both equations, the pseudospins $\tilde{S}_i$ are 3×2×2 rank 3 tensors consisting of the 2×2 spin-½ operators $\tilde{S}_x$, $\tilde{S}_y$, and $\tilde{S}_z$ operated on by the 3×3 *g*-tensor as derived from SINGLE_ANISO. In Eqn. 4.4, $\boldsymbol{B}$ is a 1×3 vector consisting of B_x, B_y, and B_z, as defined by the chosen coordinate system. A full description of the employed method is included in Appendix 1.
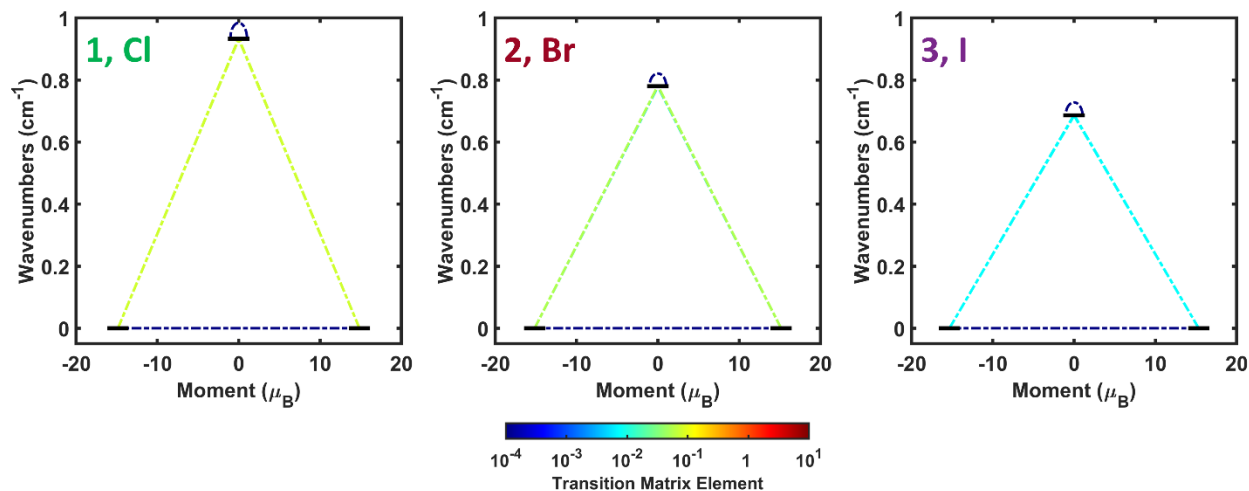

Figure 4.6: Manually calculated output states and transition matrix elements describing coupling between KD$_1$ of both metal centers in **1** (left), **2** (center), and **3** (right).

The interactions within KD$_0$ and KD$_1$ were modeled for all three compounds, and KD$_2$ was modeled for **3** to further reinforce the described relaxation pathway (TABLE, Figure 4.6). When

modeling KD_0, we compare extracted parameters to those output from POLY_ANISO to test the accuracy of the method. All three compounds show very good agreement with anisotropy tensors, orientation, and transition matrix elements. While the outputs agree nearly exactly with moments aligned associated with $\tilde{S}_z$, all other transition matrix elements agree within an order of magnitude down to 10^{-6}, below which values diverge or, below 10^{-8}, vanish entirely, likely due to the limitations of the employed software package. The degree of corroboration suggests the method is suitable to describe interactions in the excited states.

Interactions within KD_1 show a clear decrease in transition probability through the barrier from **1** to **3**. While the adiabatic QTM probability is still considered effectively quenched, the Orbach pathway from DD_0 to DD_1 within this energy regime is easily accessible, as the amount of accessible thermal energy required to meaningfully populate KD_1 is over an order of magnitude larger than the dipole interaction. This thermal pathway is an order of magnitude faster in **1** than in **2**, which is in turn several times faster than in **3**. These matrix elements are a direct consequence of the increasing degree of anisotropy in the excited doublet KD_1. Furthermore, in **1**, the coupled doublets from KD_1 are no longer rigorously degenerate, and thus the tunnel splitting ($\sim 1 \times 10^{-4}$ cm^{-1}) should be used as a more relevant parameter. The tunnel splitting within KD_1 for both **2** and **3** are two orders of magnitude smaller than in **1**. The increased degree of state mixing in **1** relative to **2** and **3** agrees well to the trend observed in other Er^{3+} systems, wherein a decrease in charge density in unfavorable coordination environments[38,122] or opposite an anisotropy-directing ligand[51,53,197] improves state purity and strengthens anisotropy. The dipolar interaction is well suited as a complement to this design philosophy, as the small energy perturbation preserves and amplifies the design principles employed in engineering the crystal field environment.
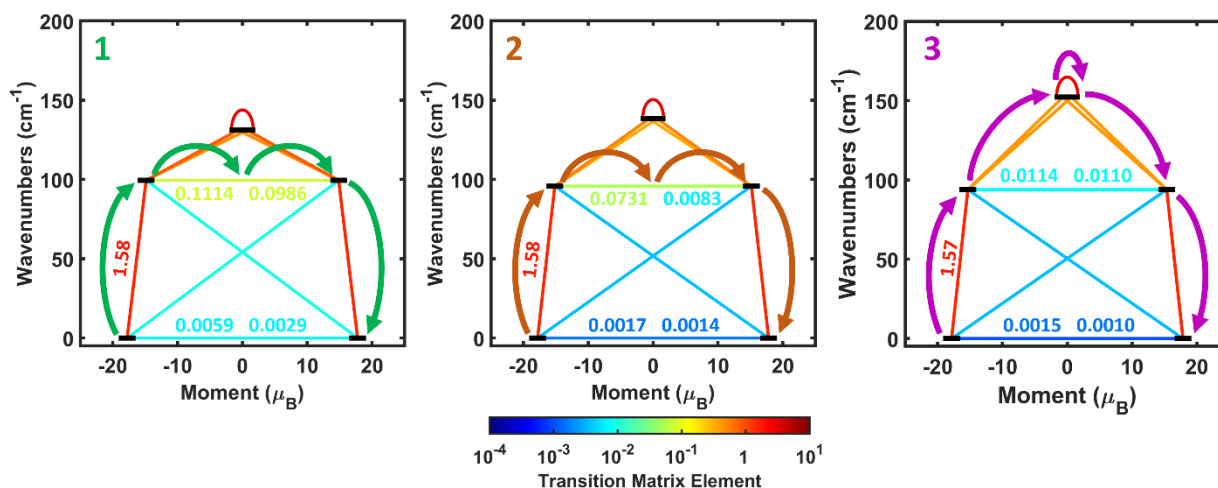
Figure 4.7: Full description of primary relaxation pathways for **1**, **2**, and **3** with dipolar coupling accounted for. Vertical transitions are obtained from SINGLE_ANISO. Through-barrier transitions represent Orbach mechanisms within dipolar-coupled energy manifolds; two transition probabilities are included to represent excitations from the ferromagnetically coupled lower energy states to either of the antiferromagnetically coupled excited state as depicted in Figure 4.6. Energy levels above KD_2 are omitted for simplicity, as they are expected to minimally contribute to relaxation.

Our description of the relaxation dynamics is completed when we consider the interactions of KD_2 in **1, 2,** and **3**. All four output states modeled for all three complexes have low moments and are non-degenerate, implying heavy mixing as described by output eigenvectors. Thus, while Zeeman matrix elements are no longer useful in describing transitions between these states, relaxation mechanisms within these four coupled states is expected to be rapid. Now we can describe primary relaxation pathways across the series (Figure 4.7). High-temperature magnetic relaxation for the faster sample of **1** are expected to proceed via thermal excitation from KD_0 to KD_1, after which it relaxes to the opposite moment state of KD_0 either directly after excitation or after another Orbach process within the dipolar-coupled multiplet. Relaxation in the slower relaxing congener of **1** and in **2** is expected to follow a similar route, though the increased measured barrier implies a similar rate of relaxation is achieved via excitation to KD_2 or a virtual excited state in between. Finally, for both habits of **3** magnetic relaxation behavior is consistent with

105

thermal excitation to KD_2, wherein through-barrier relaxation pathways are abundant and the system relaxes back to KD_0.

4.6 Conclusions

Using an isostructural series with isolobal halide bridging ligands with decreasing charge density, we have demonstrated and dissected the effects of the consequential perturbations on their magnetic energy landscape. Across the series, the lowest energy magnetic states through which magnetic relaxation is expected to proceed are well separated, and the purity of these states increases as the charge density of the bridging halide decreases. However, the large discrepancy in magnetic relaxation behavior across the series is not solely able to be described by the subtly different single-ion properties. Furthermore, while at low temperatures relaxation is well described by treating the dipolar coupling within the ground state as a first-order perturbation, the difference in high-temperature relaxation behavior required further description. We have endeavored here to illustrate this difference by treating the ground and first excited states across the series as separately coupled, treating the interactions as being limited to states within the same energy regime. Dipolar coupling is expected to be effectively suppressed in these coupled states, but the thermal excitations within the output dipolar doublets show a monotonic decrease in transition probability across the series. Since the system is expected to easily have access to these transitions within the temperature regime in which the relevant states are appreciably populated, we suggest that this can account for the difference in relaxation in the high- and intermediate-temperature regimes.

While we have effectively employed this strategy to describe magnetic behavior within this system, further refinement of how coupling is described is needed to develop an intuitive, but still general, approach. Even within this system, the proximity of the $m_J = \frac{1}{2}$ state to the lower two Kramers doublets grows closer as the charge density of the bridging ligand increases; thus, mixing

of these energy levels could in other systems increase in a way not accounted for with a first-order perturbation model using the pseudospin-½ doublets as independent input states. However, in systems with well-isolated states of high purity, we propose that this simple model can allow for good predictive power in magnetic design.

Acknowledgements

Prerequisite mathematical concepts:

Dot products in three dimensions

Change of basis

Matrix diagonalization and eigensystems

Mathematical concept #1: Kronecker Product

$$\begin{bmatrix} a & b \\ c & d \end{bmatrix} \otimes \begin{bmatrix} e & f \\ g & h \end{bmatrix} = \begin{bmatrix} ae & af & be & bf \\ ag & ah & bg & bh \\ ce & cf & de & df \\ cg & ch & dg & dh \end{bmatrix} \quad \text{Eqn. A.1}$$

Mathematical concept #2: Kronecker Sum

$$\begin{bmatrix} a & b \\ c & d \end{bmatrix} \oplus \begin{bmatrix} e & f \\ g & h \end{bmatrix}$$

$$= \begin{bmatrix} a & b \\ c & d \end{bmatrix} \otimes \begin{bmatrix} 1 & 0 \\ 0 & 1 \end{bmatrix} + \begin{bmatrix} 1 & 0 \\ 0 & 1 \end{bmatrix} \otimes \begin{bmatrix} e & f \\ g & h \end{bmatrix}$$

$$= \begin{bmatrix} a+e & f & b & 0 \\ g & a+h & 0 & b \\ c & 0 & d+e & f \\ 0 & c & g & d+h \end{bmatrix} \quad \text{Eqn. A.2}$$

Relevant Hamiltonians:

Spin Operators:

$$\tilde{S} = \begin{bmatrix} S_x \\ S_y \\ S_z \end{bmatrix} \quad \text{Eqn. A.3}$$

$$S_i = \frac{\hbar}{2}\sigma_i$$

For pseudospin-½: $\sigma_x = \begin{pmatrix} 0 & -1 \\ 1 & 0 \end{pmatrix}$ $\sigma_y = \begin{pmatrix} 0 & -i \\ i & 0 \end{pmatrix}$ $\sigma_z = \begin{pmatrix} 1 & 0 \\ 0 & -1 \end{pmatrix}$

$$S_i S_j = S_i \otimes S_j \qquad \text{Eqn. A.4}$$

Total Interaction Hamiltonian:

$$\hat{H}_{tot} = \hat{H}_{dip} + \hat{H}_{Zee} \quad \text{Eqn. A.5}$$

Dipolar Coupling:

$$\hat{H}_{dip} = \frac{C_{dip}}{r^3}\left((g_1 \cdot S_1)(g_2 \cdot S_2)^T - 3\frac{(\vec{r}^T \cdot g_1 \cdot S_1)(\vec{r}^T \cdot g_2 \cdot S_2)}{r^2} \right) \qquad \text{Eqn. A.6}$$

Additional terms:

$$\vec{r}^T = [r_x \quad r_y \quad r_z]$$

$$r = |\vec{r}^T|$$

$$g_i = \begin{bmatrix} g_{x,i} & 0 & 0 \\ 0 & g_{y,i} & 0 \\ 0 & 0 & g_{z,i} \end{bmatrix} \quad \text{(if diagonal)}$$

$$g_i = \begin{bmatrix} g_{xx,i} & g_{xy,i} & g_{xz,i} \\ g_{yx,i} & g_{yy,i} & g_{yz,i} \\ g_{zx,i} & g_{zy,i} & g_{zz,i} \end{bmatrix} \quad \text{(if not diagonal)}$$

$$C_{dip} = \frac{\mu_0 \mu_B^2}{4\pi \hbar^2} = 0.43297 \text{ Å}^3 \frac{cm^{-1}}{T}$$

μ_0 = Permittivity of free space; μ_B = Bohr magneton; $\hbar$ = Reduced Planck's constant

Zeeman Interaction:

$$\hat{H}_{Zee,single} = B \cdot g \cdot \hat{S} \qquad \text{Eqn. A.7}$$

$$\hat{H}_{Zee,coup} = \frac{\mu_B}{\hbar}\left(B \cdot g_1 \cdot \hat{S}_1\right) \oplus \left(B \cdot g_2 \cdot \hat{S}_2\right) \qquad \text{Eqn. A.8}$$

Additional terms:

$$B = [B_x \quad B_y \quad B_z]$$

$$g = \begin{bmatrix} g_x & 0 & 0 \\ 0 & g_y & 0 \\ 0 & 0 & g_z \end{bmatrix} \quad \text{(if diagonal)}$$

$$g = \begin{bmatrix} g_{xx} & g_{xy} & g_{xz} \\ g_{yx} & g_{yy} & g_{yz} \\ g_{zx} & g_{zy} & g_{zz} \end{bmatrix} \quad \text{(if not diagonal)}$$

Process for coupling pseudospin-½ systems:

g-tensor for each center:

Output from single_aniso: $\begin{bmatrix} g_x \\ g_y \\ g_z \end{bmatrix}$; represented as a diagnal 3×3 matrix: $\begin{bmatrix} g_x & 0 & 0 \\ 0 & g_y & 0 \\ 0 & 0 & g_z \end{bmatrix}$

Rotation matrix between diagonal magnetic axes and crystallographic coordinate system:

Output from single_aniso as an orthonormal 3×3 matrix (R_i) representing the change-of-basis rotation from the crystallographic coordinate system to the basis where the main magnetic axes are orthogonal

Finding the bases of output dipolar coupled states with diagonal *g*-tensors:

$$g_{i,cryst} = R_i^T \cdot \begin{bmatrix} g_{xi} & 0 & 0 \\ 0 & g_{yi} & 0 \\ 0 & 0 & g_{zi} \end{bmatrix} \qquad \text{Eqn. A.10}$$

$$g_{F,cryst} = g_{1,cryst} + g_{2,cryst} \quad \text{Eqn. A.11}$$

$$g_{AF,cryst} = g_{1,cryst} - g_{2,cryst} \qquad \text{Eqn. A.12}$$

Rotating output *g*-tensors into a block-diagonal basis:

The rotation matrix from a diagonal magnetic coordinate system crystallographic coordinates can be described as the rotation from the identity matrix to an orthonormal matrix. Thus, the g-tensors in crystallographic coordinates can be decomposed into an orthonormal basis; we implemented the Gram-Schmidt algorithm[198] in MatLab. This then becomes a rotation matrix analogous to R_i^T, so it is dubbed R_F^T or R_{AF}^T.

Rotating g-tensors for each center into basis of chosen coupled state:

$$g_{i,F} = R_F \cdot g_{i,cryst} \qquad \text{Eqn. A.13}$$

$$g_{i,AF} = R_{AF} \cdot g_{i,cryst} \quad \text{Eqn. A.14}$$

These values can then be used to compute the above Hamiltonians. In the case of the dipolar

Hamiltonian, $\vec{r}^T$ must be rotated into the same basis as g_i

REFERENCES

(1)   Kurti, N. *Selected Works of Louis Neel*; Taylor & Francis, 1988.

(2)   Farrelly, D.; Milligan, J. A. Classical and Quantum Mechanics of the Driven Double Well. In *Time-Dependent Quantum Molecular Dynamics*; Broeckhove, J., Lathouwers, L., Eds.; Nato ASI Series; Springer US: Boston, MA, 1992; pp 45–55. https://doi.org/10.1007/978-1-4899-2326-4_4.

(3)   Haase, W. Oliver Kahn: Molecular Magnetism. VCH-Verlag, Weinheim, New York 1993. ISBN 3-527-89566-3, 380 Seiten, Preis: DM 154,—. *Berichte der Bunsengesellschaft für physikalische Chemie* **1994**, *98* (9), 1208–1208. https://doi.org/10.1002/bbpc.19940980935.

(4)   Gatteschi, D.; Sessoli, R.; Villain, J. *Molecular Nanomagnets*; 2006; Vol. 376. https://doi.org/10.1093/acprof:oso/9780198567530.001.0001.

(5)   Orchard, A. F. *Magnetochemistry*; Oxford University Press, 2007.

(6)   Woodruff, D. N.; Winpenny, R. E. P.; Layfield, R. A. Lanthanide Single-Molecule Magnets. *Chem. Rev.* **2013**, *113* (7), 5110–5148. https://doi.org/10.1021/cr400018q.

(7)   McInnes, E. J. L. Introduction to Molecular Magnetism. From Transition Metals to Lanthanides By Cristiano Benelli and Dante Gatteschi. *Angewandte Chemie International Edition* **2016**, *55* (6), 1959–1959. https://doi.org/10.1002/anie.201511481.

(8)   Chen, Y.-C.; Tong, M.-L. Single-Molecule Magnets beyond a Single Lanthanide Ion: The Art of Coupling. *Chem. Sci.* **2022**. https://doi.org/10.1039/D2SC01532C.

(9)   Fisher, M. E. Transformations of Ising Models. *Phys. Rev.* **1959**, *113* (4), 969–981. https://doi.org/10.1103/PhysRev.113.969.

(10)   Glauber, R. J. Time-Dependent Statistics of the Ising Model. *Journal of Mathematical Physics* **1963**, *4* (2), 294–307. https://doi.org/10.1063/1.1703954.

(11)   Drillon, M.; Coronado, E.; Beltran, D.; Georges, R. Classical Treatment of a Heisenberg Linear Chain with Spin Alternation; Application to the MnNi(EDTA)-6H2O Complex. *Chemical Physics* **1983**, *79* (3), 449–453. https://doi.org/10.1016/0301-0104(83)85267-7.

(12)   Coronado, E.; Drillon, M.; Nugteren, P. R.; Jongh, L. J. D.; Beltran, D.; Georges, R. *Low-temperature investigation of the ferrimagnetic chains MnM' (EDTA).cntdot.6H2O [M' = cobalt, nickel, and copper(II)]: thermal and magnetic properties*. ACS Publications. https://doi.org/10.1021/ja00193a019.

(13)   Miyasaka, H.; Julve, M.; Yamashita, M.; Clérac, R. Slow Dynamics of the Magnetization in One-Dimensional Coordination Polymers: Single-Chain Magnets. *Inorg. Chem.* **2009**, *48* (8), 3420–3437. https://doi.org/10.1021/ic802050j.

(14)   Sessoli, R.; Gatteschi, D.; Caneschi, A.; Novak, M. A. Magnetic Bistability in a Metal-Ion Cluster. *Nature* **1993**, *365* (6442), 141–143. https://doi.org/10.1038/365141a0.

(15)   Sessoli, R.; Tsai, H. L.; Schake, A. R.; Wang, S.; Vincent, J. B.; Folting, K.; Gatteschi, D.; Christou, G.; Hendrickson, D. N. High-Spin Molecules: [Mn12O12(O2CR)16(H2O)4]. *J. Am. Chem. Soc.* **1993**, *115* (5), 1804–1816. https://doi.org/10.1021/ja00058a027.

(16) Layfield, R. A. Organometallic Single-Molecule Magnets. *Organometallics* **2014**, *33* (5), 1084–1099. https://doi.org/10.1021/om401107f.

(17) Milios, C. J.; Vinslava, A.; Wernsdorfer, W.; Moggach, S.; Parsons, S.; Perlepes, S. P.; Christou, G.; Brechin, E. K. A Record Anisotropy Barrier for a Single-Molecule Magnet. *J. Am. Chem. Soc.* **2007**, *129* (10), 2754–2755. https://doi.org/10.1021/ja068961m.

(18) Ishikawa, N.; Sugita, M.; Ishikawa, T.; Koshihara, S.; Kaizu, Y. Lanthanide Double-Decker Complexes Functioning as Magnets at the Single-Molecular Level. *J. Am. Chem. Soc.* **2003**, *125* (29), 8694–8695. https://doi.org/10.1021/ja029629n.

(19) Miessler, G. L.; Fischer, P. J.; Tarr, D. A. *Inorganic Chemistry*; Pearson Education, 2013.

(20) Cubic Harmonic. *Wikipedia*; 2021.

(21) Spherical Harmonics. *Wikipedia*; 2023.

(22) Table of Spherical Harmonics. *Wikipedia*; 2023.

(23) *Difference Between Spin-orbit Coupling and Russell-Saunders Effect*. Compare the Difference Between Similar Terms. https://www.differencebetween.com/difference-between-spin-orbit-coupling-and-russell-saunders-effect/ (accessed 2023-05-27).

(24) Angular Momentum Coupling. *Wikipedia*; 2023.

(25) Tasaki, H. *Physics and Mathematics of Quantum Many-Body Systems*; Graduate texts in physics; Springer: Cham, 2020.

(26) Rinehart, J. D.; Long, J. R. Exploiting Single-Ion Anisotropy in the Design of f-Element Single-Molecule Magnets. *Chem. Sci.* **2011**, *2* (11), 2078–2085. https://doi.org/10.1039/C1SC00513H.

(27) Sievers, J. Asphericity of 4f-Shells in Their Hund's Rule Ground States. *Zeitschrift für Physik B Condensed Matter* **1982**, *45* (4), 289–296. https://doi.org/10.1007/BF01321865.

(28) Liu, J.-L.; Chen, Y.-C.; Tong, M.-L. Symmetry Strategies for High Performance Lanthanide-Based Single-Molecule Magnets. *Chem. Soc. Rev.* **2018**, *47* (7), 2431–2453. https://doi.org/10.1039/C7CS00266A.

(29) Orbach, R. Spin-Lattice Relaxation in Rare-Earth Salts. *Proceedings of the Royal Society of London. Series A, Mathematical and Physical Sciences* **1961**, *264* (1319), 458–484.

(30) Aravena, D.; Ruiz, E. Spin Dynamics in Single-Molecule Magnets and Molecular Qubits. *Dalton Trans.* **2020**, *49* (29), 9916–9928. https://doi.org/10.1039/D0DT01414A.

(31) Gu, L.; Wu, R. Origin of the Anomalously Low Raman Exponents in Single Molecule Magnets. *Phys. Rev. B* **2021**, *103* (1), 014401. https://doi.org/10.1103/PhysRevB.103.014401.

(32) Briganti, M.; Santanni, F.; Tesi, L.; Totti, F.; Sessoli, R.; Lunghi, A. A Complete Ab Initio View of Orbach and Raman Spin–Lattice Relaxation in a Dysprosium Coordination Compound. *J. Am. Chem. Soc.* **2021**. https://doi.org/10.1021/jacs.1c05068.

(33) Gu, L.; Li, J.; Wu, R. Reconsidering Spin-Phonon Relaxation in Magnetic Molecules. *Journal of Magnetism and Magnetic Materials* **2022**, *564*, 170138. https://doi.org/10.1016/j.jmmm.2022.170138.

(34)   Gómez-Coca, S.; Urtizberea, A.; Cremades, E.; Alonso, P. J.; Camón, A.; Ruiz, E.; Luis, F. Origin of Slow Magnetic Relaxation in Kramers Ions with Non-Uniaxial Anisotropy. *Nat Commun* **2014**, *5* (1), 4300. https://doi.org/10.1038/ncomms5300.

(35)   Gu, L.; Wu, R. Origins of Slow Magnetic Relaxation in Single-Molecule Magnets. *Phys. Rev. Lett.* **2020**, *125* (11), 117203. https://doi.org/10.1103/PhysRevLett.125.117203.

(36)   Jackson, C. E.; Moseley, I. P.; Martinez, R.; Sung, S.; Zadrozny, J. M. A Reaction-Coordinate Perspective of Magnetic Relaxation. *Chem. Soc. Rev.* **2021**, *50* (12), 6684–6699. https://doi.org/10.1039/D1CS00001B.

(37)   Guo, F.-S.; Day, B. M.; Chen, Y.-C.; Tong, M.-L.; Mansikkamäki, A.; Layfield, R. A. Magnetic Hysteresis up to 80 Kelvin in a Dysprosium Metallocene Single-Molecule Magnet. *Science* **2018**, *362* (6421), 1400. https://doi.org/10.1126/science.aav0652.

(38)   Ding, Y.-S.; Chilton, N. F.; Winpenny, R. E. P.; Zheng, Y.-Z. On Approaching the Limit of Molecular Magnetic Anisotropy: A Near-Perfect Pentagonal Bipyramidal Dysprosium(III) Single-Molecule Magnet. *Angewandte Chemie International Edition* **2016**, *55* (52), 16071–16074. https://doi.org/10.1002/anie.201609685.

(39)   Goodwin, C. A. P.; Ortu, F.; Reta, D.; Chilton, N. F.; Mills, D. P. Molecular Magnetic Hysteresis at 60 Kelvin in Dysprosocenium. *Nature* **2017**, *548* (7668), 439–442. https://doi.org/10.1038/nature23447.

(40)   Ding, Y.-S.; Han, T.; Zhai, Y.-Q.; Reta, D.; Chilton, N. F.; Winpenny, R. E. P.; Zheng, Y.-Z. A Study of Magnetic Relaxation in Dysprosium(III) Single-Molecule Magnets. *Chemistry – A European Journal* **2020**, *26* (26), 5893–5902. https://doi.org/10.1002/chem.202000646.

(41)   Huang, G.-Z.; Ruan, Z.-Y.; Zheng, J.-Y.; Chen, Y.-C.; Wu, S.-G.; Liu, J.-L.; Tong, M.-L. Seeking Magneto-Structural Correlations in Easily Tailored Pentagonal Bipyramid Dy(III) Single-Ion Magnets. *Sci. China Chem.* **2020**, *63* (8), 1066–1074. https://doi.org/10.1007/s11426-020-9746-x.

(42)   Chen, Y.-C.; Liu, J.-L.; Ungur, L.; Liu, J.; Li, Q.-W.; Wang, L.-F.; Ni, Z.-P.; Chibotaru, L. F.; Chen, X.-M.; Tong, M.-L. Symmetry-Supported Magnetic Blocking at 20 K in Pentagonal Bipyramidal Dy(III) Single-Ion Magnets. *J. Am. Chem. Soc.* **2016**, *138* (8), 2829–2837. https://doi.org/10.1021/jacs.5b13584.

(43)   Chen, Y.-C.; Liu, J.-L.; Lan, Y.; Zhong, Z.-Q.; Mansikkamäki, A.; Ungur, L.; Li, Q.-W.; Jia, J.-H.; Chibotaru, L. F.; Han, J.-B.; Wernsdorfer, W.; Chen, X.-M.; Tong, M.-L. Dynamic Magnetic and Optical Insight into a High Performance Pentagonal Bipyramidal DyIII Single-Ion Magnet. *Chemistry – A European Journal* **2017**, *23* (24), 5708–5715. https://doi.org/10.1002/chem.201606029.

(44)   Canaj, A. B.; Singh, M. K.; Wilson, C.; Rajaraman, G.; Murrie, M. Chemical and in Silico Tuning of the Magnetisation Reversal Barrier in Pentagonal Bipyramidal Dy(III) Single-Ion Magnets. *Chem. Commun.* **2018**, *54* (59), 8273–8276. https://doi.org/10.1039/C8CC03929A.

(45)   Zhang, P.; Zhang, L.; Wang, C.; Xue, S.; Lin, S.-Y.; Tang, J. Equatorially Coordinated Lanthanide Single Ion Magnets. *J. Am. Chem. Soc.* **2014**, *136* (12), 4484–4487. https://doi.org/10.1021/ja500793x.

(46) Zhang, H.; Nakanishi, R.; Katoh, K.; Breedlove, B. K.; Kitagawa, Y.; Yamashita, M. Low Coordinated Mononuclear Erbium(Iii) Single-Molecule Magnets with C3v Symmetry: A Method for Altering Single-Molecule Magnet Properties by Incorporating Hard and Soft Donors. *Dalton Trans.* **2018**, *47* (2), 302–305. https://doi.org/10.1039/C7DT04053A.

(47) Lu, F.; Ding, M.-M.; Li, J.-X.; Wang, B.-L.; Zhang, Y.-Q. Why Lanthanide ErIII SIMs Cannot Possess Huge Energy Barriers: A Theoretical Investigation. *Dalton Trans.* **2020**, *49* (41), 14576–14583. https://doi.org/10.1039/D0DT02868A.

(48) Meihaus, K. R.; Long, J. R. Magnetic Blocking at 10 K and a Dipolar-Mediated Avalanche in Salts of the Bis(H8-Cyclooctatetraenide) Complex [Er(COT)2]−. *J. Am. Chem. Soc.* **2013**, *135* (47), 17952–17957. https://doi.org/10.1021/ja4094814.

(49) Jiang, S.-D.; Wang, B.-W.; Sun, H.-L.; Wang, Z.-M.; Gao, S. An Organometallic Single-Ion Magnet. *J. Am. Chem. Soc.* **2011**, *133* (13), 4730–4733. https://doi.org/10.1021/ja200198v.

(50) Jiang, S.-D.; Liu, S.-S.; Zhou, L.-N.; Wang, B.-W.; Wang, Z.-M.; Gao, S. Series of Lanthanide Organometallic Single-Ion Magnets. *Inorg. Chem.* **2012**, *51* (5), 3079–3087. https://doi.org/10.1021/ic202511n.

(51) Meng, Y.-S.; Wang, C.-H.; Zhang, Y.-Q.; Leng, X.-B.; Wang, B.-W.; Chen, Y.-F.; Gao, S. (Boratabenzene)(Cyclooctatetraenyl) Lanthanide Complexes: A New Type of Organometallic Single-Ion Magnet. *Inorg. Chem. Front.* **2016**, *3* (6), 828–835. https://doi.org/10.1039/C6QI00028B.

(52) Lorenz, V.; Liebing, P.; Böhme, M.; Buchholz, A.; Plass, W.; Geue, N.; Hilfert, L.; Busse, S.; Engelhardt, F.; Hrib, C. G.; Edelmann, F. T. Lanthanide(III) Sandwich and Half-Sandwich Complexes with Bulky Cyclooctatetraenyl Ligands: Synthesis, Structures, and Magnetic Properties. *European Journal of Inorganic Chemistry* **2017**, *2017* (41), 4840–4849. https://doi.org/10.1002/ejic.201700878.

(53) Chen, S.-M.; Xiong, J.; Zhang, Y.-Q.; Yuan, Q.; Wang, B.-W.; Gao, S. A Soft Phosphorus Atom to "Harden" an Erbium(III) Single-Ion Magnet. *Chem. Sci.* **2018**, *9* (38), 7540–7545. https://doi.org/10.1039/C8SC01626G.

(54) He, M.; Chen, X.; Bodenstein, T.; Nyvang, A.; Schmidt, S. F. M.; Peng, Y.; Moreno-Pineda, E.; Ruben, M.; Fink, K.; Gamer, M. T.; Powell, A. K.; Roesky, P. W. Enantiopure Benzamidinate/Cyclooctatetraene Complexes of the Rare-Earth Elements: Synthesis, Structure, and Magnetism. *Organometallics* **2018**, *37* (21), 3708–3717. https://doi.org/10.1021/acs.organomet.8b00412.

(55) Meng, Y.-S.; Yang, M.-W.; Xu, L.; Xiong, J.; Hu, J.-Y.; Liu, T.; Wang, B.-W.; Gao, S. Design Principle of Half-Sandwich Type Erbium Single-Ion Magnets through Crystal Field Engineering: A Combined Magnetic and Electronic Structure Study. *Dalton Trans.* **2019**, *48* (28), 10407–10411. https://doi.org/10.1039/C9DT01954E.

(56) Le Roy, J. J.; Jeletic, M.; Gorelsky, S. I.; Korobkov, I.; Ungur, L.; Chibotaru, L. F.; Murugesu, M. An Organometallic Building Block Approach To Produce a Multidecker 4f Single-Molecule Magnet. *J. Am. Chem. Soc.* **2013**, *135* (9), 3502–3510. https://doi.org/10.1021/ja310642h.

(57) Ungur, L.; Le Roy, J. J.; Korobkov, I.; Murugesu, M.; Chibotaru, L. F. Fine-Tuning the Local Symmetry to Attain Record Blocking Temperature and Magnetic Remanence in a Single-Ion Magnet. *Angewandte Chemie* **2014**, *126* (17), 4502–4506. https://doi.org/10.1002/ange.201310451.

(58) Le Roy, J. J.; Korobkov, I.; Murugesu, M. A Sandwich Complex with Axial Symmetry for Harnessing the Anisotropy in a Prolate Erbium(Iii) Ion. *Chem. Commun.* **2014**, *50* (13), 1602–1604. https://doi.org/10.1039/C3CC48557A.

(59) Le Roy, J. J.; Ungur, L.; Korobkov, I.; Chibotaru, L. F.; Murugesu, M. Coupling Strategies to Enhance Single-Molecule Magnet Properties of Erbium–Cyclooctatetraenyl Complexes. *J. Am. Chem. Soc.* **2014**, *136* (22), 8003–8010. https://doi.org/10.1021/ja5022552.

(60) Hilgar, J. D.; Butts, A. K.; Rinehart, J. D. A Method for Extending AC Susceptometry to Long-Timescale Magnetic Relaxation. *Phys. Chem. Chem. Phys.* **2019**, *21* (40), 22302–22307. https://doi.org/10.1039/C9CP03936H.

(61) von Kugelgen, S.; Krzyaniak, M. D.; Gu, M.; Puggioni, D.; Rondinelli, J. M.; Wasielewski, M. R.; Freedman, D. E. Spectral Addressability in a Modular Two Qubit System. *J. Am. Chem. Soc.* **2021**, *143* (21), 8069–8077. https://doi.org/10.1021/jacs.1c02417.

(62) Sessoli, R. Toward the Quantum Computer: Magnetic Molecules Back in the Race. *ACS Cent. Sci.* **2015**, *1* (9), 473–474. https://doi.org/10.1021/acscentsci.5b00384.

(63) Gaita-Ariño, A.; Luis, F.; Hill, S.; Coronado, E. Molecular Spins for Quantum Computation. *Nature Chemistry* **2019**, *11* (4), 301–309. https://doi.org/10.1038/s41557-019-0232-y.

(64) Gould Colin A.; McClain K. Randall; Reta Daniel; Kragskow Jon G. C.; Marchiori David A.; Lachman Ella; Choi Eun-Sang; Analytis James G.; Britt R. David; Chilton Nicholas F.; Harvey Benjamin G.; Long Jeffrey R. Ultrahard Magnetism from Mixed-Valence Dilanthanide Complexes with Metal-Metal Bonding. *Science* **2022**, *375* (6577), 198–202. https://doi.org/10.1126/science.abl5470.

(65) Demir, S.; Zadrozny, J. M.; Nippe, M.; Long, J. R. Exchange Coupling and Magnetic Blocking in Bipyrimidyl Radical-Bridged Dilanthanide Complexes. *J. Am. Chem. Soc.* **2012**, *134* (45), 18546–18549. https://doi.org/10.1021/ja308945d.

(66) Rinehart, J. D.; Fang, M.; Evans, W. J.; Long, J. R. Strong Exchange and Magnetic Blocking in N_2^{3-}-Radical-Bridged Lanthanide Complexes. *Nature Chem* **2011**, *3* (7), 538–542. https://doi.org/10.1038/nchem.1063.

(67) Demir, S.; Nippe, M.; Gonzalez, M. I.; Long, J. R. Exchange Coupling and Magnetic Blocking in Dilanthanide Complexes Bridged by the Multi-Electron Redox-Active Ligand 2,3,5,6-Tetra(2-Pyridyl)Pyrazine. *Chem. Sci.* **2014**, *5* (12), 4701–4711. https://doi.org/10.1039/C4SC02154A.

(68) Demir, S.; Jeon, I.-R.; Long, J. R.; Harris, T. D. Radical Ligand-Containing Single-Molecule Magnets. *Coordination Chemistry Reviews* **2015**, *289–290*, 149–176. https://doi.org/10.1016/j.ccr.2014.10.012.

(69) Guo, F.-S.; Layfield, R. A. Strong Direct Exchange Coupling and Single-Molecule Magnetism in Indigo-Bridged Lanthanide Dimers. *Chem. Commun.* **2017**, *53* (21), 3130–3133. https://doi.org/10.1039/C7CC01046J.

(70) Demir, S.; Gonzalez, M. I.; Darago, L. E.; Evans, W. J.; Long, J. R. Giant Coercivity and High Magnetic Blocking Temperatures for N2 3− Radical-Bridged Dilanthanide Complexes upon Ligand Dissociation. *Nat Commun* **2017**, *8* (1), 2144. https://doi.org/10.1038/s41467-017-01553-w.

(71) Pedersen, K. S.; Bendix, J.; Clérac, R. Single-Molecule Magnet Engineering: Building-Block Approaches. *Chem. Commun.* **2014**, *50* (34), 4396–4415. https://doi.org/10.1039/C4CC00339J.

(72) Harriman, K. L. M.; Murugesu, M. An Organolanthanide Building Block Approach to Single-Molecule Magnets. *Acc. Chem. Res.* **2016**, *49* (6), 1158–1167. https://doi.org/10.1021/acs.accounts.6b00100.

(73) Hilgar, J. D.; Bernbeck, M. G.; Flores, B. S.; Rinehart, J. D. Metal–Ligand Pair Anisotropy in a Series of Mononuclear Er–COT Complexes. *Chemical Science* **2018**, *9* (36), 7204–7209. https://doi.org/10.1039/C8SC01361F.

(74) Hilgar, J. D.; Flores, B. S.; Rinehart, J. D. Ferromagnetic Coupling in a Chloride-Bridged Erbium Single-Molecule Magnet. *Chemical Communications* **2017**, *53* (53), 7322–7324. https://doi.org/10.1039/C7CC02356A.

(75) Hilgar, J. D.; Bernbeck, M. G.; Rinehart, J. D. Million-Fold Relaxation Time Enhancement across a Series of Phosphino-Supported Erbium Single-Molecule Magnets. *J. Am. Chem. Soc.* **2019**, *141* (5), 1913–1917. https://doi.org/10.1021/jacs.8b13514.

(76) Sessoli, R.; Gatteschi, D.; Caneschi, A.; Novak, M. A. Magnetic Bistability in a Metal-Ion Cluster. *Nature* **1993**, *365* (6442), 141–143. https://doi.org/10.1038/365141a0.

(77) Sessoli, R.; Tsai, H. L.; Schake, A. R.; Wang, S.; Vincent, J. B.; Folting, K.; Gatteschi, D.; Christou, G.; Hendrickson, D. N. *High-spin molecules: [Mn12O12(O2CR)16(H2O)4]*. https://doi.org/10.1021/ja00058a027.

(78) Frost, J. M.; Harriman, K. L. M.; Murugesu, M. The Rise of 3-d Single-Ion Magnets in Molecular Magnetism: Towards Materials from Molecules? *Chem. Sci.* **2016**, *7* (4), 2470–2491. https://doi.org/10.1039/C5SC03224E.

(79) Maniaki, D.; Pilichos, E.; Perlepes, S. P. Coordination Clusters of 3d-Metals That Behave as Single-Molecule Magnets (SMMs): Synthetic Routes and Strategies. *Frontiers in Chemistry* **2018**, *6*, 461. https://doi.org/10.3389/fchem.2018.00461.

(80) McAdams, S. G.; Ariciu, A.-M.; Kostopoulos, A. K.; Walsh, J. P. S.; Tuna, F. Molecular Single-Ion Magnets Based on Lanthanides and Actinides: Design Considerations and New Advances in the Context of Quantum Technologies. *Coordination Chemistry Reviews* **2017**, *346*, 216–239. https://doi.org/10.1016/j.ccr.2017.03.015.

(81) Harriman, K. L. M.; Errulat, D.; Murugesu, M. Magnetic Axiality: Design Principles from Molecules to Materials. *Trends in Chemistry* **2019**. https://doi.org/10.1016/j.trechm.2019.04.005.

(82) Liu, J.-L.; Chen, Y.-C.; Tong, M.-L. Symmetry Strategies for High Performance Lanthanide-Based Single-Molecule Magnets. *Chem. Soc. Rev.* **2018**, *47* (7), 2431–2453. https://doi.org/10.1039/C7CS00266A.

(83) Dey, A.; Kalita, P.; Chandrasekhar, V. Lanthanide(III)-Based Single-Ion Magnets. *ACS Omega* **2018**, *3* (8), 9462–9475. https://doi.org/10.1021/acsomega.8b01204.

(84) Guo, F.-S.; Day, B. M.; Chen, Y.-C.; Tong, M.-L.; Mansikkamäki, A.; Layfield, R. A. A Dysprosium Metallocene Single-Molecule Magnet Functioning at the Axial Limit. *Angewandte Chemie International Edition* **2017**, *56* (38), 11445–11449. https://doi.org/10.1002/anie.201705426.

(85) Goodwin, C. A. P.; Ortu, F.; Reta, D.; Chilton, N. F.; Mills, D. P. Molecular Magnetic Hysteresis at 60 Kelvin in Dysprosocenium. *Nature* **2017**, *548*, 439.

(86) Giansiracusa, M. J.; Moreno-Pineda, E.; Hussain, R.; Marx, R.; Martínez Prada, M.; Neugebauer, P.; Al-Badran, S.; Collison, D.; Tuna, F.; van Slageren, J.; Carretta, S.; Guidi, T.; McInnes, E. J. L.; Winpenny, R. E. P.; Chilton, N. F. Measurement of Magnetic Exchange in Asymmetric Lanthanide Dimetallics: Toward a Transferable Theoretical Framework. *J. Am. Chem. Soc.* **2018**, *140* (7), 2504–2513. https://doi.org/10.1021/jacs.7b10714.

(87) Rinehart, J. D.; Fang, M.; Evans, W. J.; Long, J. R. A N23– Radical-Bridged Terbium Complex Exhibiting Magnetic Hysteresis at 14 K. *J. Am. Chem. Soc.* **2011**, *133* (36), 14236–14239. https://doi.org/10.1021/ja206286h.

(88) Gould, C. A.; Darago, L. E.; Gonzalez, M. I.; Demir, S.; Long, J. R. A Trinuclear Radical-Bridged Lanthanide Single-Molecule Magnet. *Angewandte Chemie International Edition* **2017**, *56* (34), 10103–10107. https://doi.org/10.1002/anie.201612271.

(89) Steenbock, T.; Shultz, D. A.; Kirk, M. L.; Herrmann, C. Influence of Radical Bridges on Electron Spin Coupling. *J. Phys. Chem. A* **2017**, *121* (1), 216–225. https://doi.org/10.1021/acs.jpca.6b07270.

(90) Huang, G.; Daiguebonne, C.; Calvez, G.; Suffren, Y.; Guillou, O.; Guizouarn, T.; Le Guennic, B.; Cador, O.; Bernot, K. Strong Magnetic Coupling and Single-Molecule-Magnet Behavior in Lanthanide-TEMPO Radical Chains. *Inorg. Chem.* **2018**, *57* (17), 11044–11057. https://doi.org/10.1021/acs.inorgchem.8b01640.

(91) Le Roy, J. J.; Jeletic, M.; Gorelsky, S. I.; Korobkov, I.; Ungur, L.; Chibotaru, L. F.; Murugesu, M. An Organometallic Building Block Approach To Produce a Multidecker 4f Single-Molecule Magnet. *J. Am. Chem. Soc.* **2013**, *135* (9), 3502–3510. https://doi.org/10.1021/ja310642h.

(92) Jiang, S.-D.; Wang, B.-W.; Sun, H.-L.; Wang, Z.-M.; Gao, S. An Organometallic Single-Ion Magnet. *J. Am. Chem. Soc.* **2011**, *133* (13), 4730–4733. https://doi.org/10.1021/ja200198v.

(93) Meng, Y.-S.; Wang, C.-H.; Zhang, Y.-Q.; Leng, X.-B.; Wang, B.-W.; Chen, Y.-F.; Gao, S. (Boratabenzene)(Cyclooctatetraenyl) Lanthanide Complexes: A New Type of Organometallic Single-Ion Magnet. *Inorg. Chem. Front.* **2016**, *3* (6), 828–835. https://doi.org/10.1039/C6QI00028B.

(94) Westin, L. G.; Kritikos, M.; Caneschi, A. Self Assembly, Structure and Properties of the Decanuclear Lanthanide Ring Complex, Dy10(OC2H4OCH3)30. *Chem. Commun.* **2003**, *0* (8), 1012–1013. https://doi.org/10.1039/B300237C.

(95) Yang, P.-P.; Gao, X.-F.; Song, H.-B.; Zhang, S.; Mei, X.-L.; Li, L.-C.; Liao, D.-Z. Slow Magnetic Relaxation in Novel Dy4 and Dy8 Compounds. *Inorg. Chem.* **2011**, *50* (3), 720–722. https://doi.org/10.1021/ic1021643.

(96) Baniodeh, A.; Magnani, N.; Bräse, S.; Anson, C. E.; Powell, A. K. Ligand Field Variations: Tuning the Toroidal Moment of Dy6 Rings. *Dalton Trans.* **2015**, *44* (14), 6343–6347. https://doi.org/10.1039/C5DT00237K.

(97) Gao, F.; Feng, X.; Yang, L.; Chen, X. New Sandwich-Type Lanthanide Complexes Based on Closed-Macrocyclic Schiff Base and Phthalocyanine Molecules. *Dalton Trans.* **2016**, *45* (17), 7476–7482. https://doi.org/10.1039/C6DT00683C.

(98) Sun, H.; Liu, M.; Zhang, B. Two Dysprosium Complexes Based on 8-Hydroxyquinoline Schiff Base: Structures, Luminescence Properties and Single-Molecule Magnets Behaviors. *Inorganica Chimica Acta* **2016**, *453*, 681–686. https://doi.org/10.1016/j.ica.2016.09.026.

(99) Peng, G.; Zhang, Y.-Y.; Li, Z.-Y.; Kostakis, G. E. First Examples of Polynuclear Lanthanide Diethylene Glycol Based Coordination Clusters. *European Journal of Inorganic Chemistry* **2017**, *2017* (20), 2700–2706. https://doi.org/10.1002/ejic.201700168.

(100) Baniodeh, A.; Mondal, A.; Galeev, R.; Sukhanov, A.; Eremina, R.; Voronkova, V.; Anson, C. E.; Powell, A. K. How Far Can the Anisotropy Deviate from Uniaxiality in a Dy-Based Single-Molecule Magnet? Dinuclear Dy(III) Complex Study. *Appl Magn Reson* **2017**, *48* (1), 101–113. https://doi.org/10.1007/s00723-016-0852-y.

(101) Zahra, A.; Mahmud, T.; Tahir, M. N.; Shad, H. A.; Rehman, H.; Naseem, S. Synthesis, Characterization and Magnetic Studies of Dysprosium Complex, [Dy2(TEA)2(O2CPh)4·2H2O]. *J Chem Crystallogr* **2017**, *47* (5), 151–156. https://doi.org/10.1007/s10870-017-0691-1.

(102) Wang, W.-M.; Wang, S.; Wu, Z.-L.; Ran, Y.-G.; Ren, Y.-H.; Zhang, C.-F.; Fang, M. Two Phenoxo-O Bridged Dy2 Complexes Based on 8-Hydroxyquinolin Derivatives with Different Magnetic Relaxation Features. *Inorganic Chemistry Communications* **2017**, *76*, 48–51. https://doi.org/10.1016/j.inoche.2017.01.001.

(103) Palumbo, C. T.; Darago, L. E.; Windorff, C. J.; Ziller, J. W.; Evans, W. J. Trimethylsilyl versus Bis(Trimethylsilyl) Substitution in Tris(Cyclopentadienyl) Complexes of La, Ce, and Pr: Comparison of Structure, Magnetic Properties, and Reactivity. *Organometallics* **2018**, *37* (6), 900–905. https://doi.org/10.1021/acs.organomet.7b00881.

(104) Guo, Y.-N.; Xu, G.-F.; Wernsdorfer, W.; Ungur, L.; Guo, Y.; Tang, J.; Zhang, H.-J.; Chibotaru, L. F.; Powell, A. K. Strong Axiality and Ising Exchange Interaction Suppress Zero-Field Tunneling of Magnetization of an Asymmetric Dy2 Single-Molecule Magnet. *J. Am. Chem. Soc.* **2011**, *133* (31), 11948–11951. https://doi.org/10.1021/ja205035g.

(105) Sheldrick, G. M. Crystal Structure Refinement with It SHELXL. *Acta Crystallographica Section C* **2015**, *71* (1), 3–8. https://doi.org/10.1107/S2053229614024218.

(106) Dolomanov, O. V.; Bourhis, L. J.; Gildea, R. J.; Howard, J. a. K.; Puschmann, H. OLEX2: A Complete Structure Solution, Refinement and Analysis Program. *J Appl Cryst* **2009**, *42* (2), 339–341. https://doi.org/10.1107/S0021889808042726.

(107) Bain, G. A.; Berry, J. F. Diamagnetic Corrections and Pascal's Constants. *J. Chem. Educ.* **2008**, *85* (4), 532. https://doi.org/10.1021/ed085p532.

(108) Cendrowski-Guillaume, S. M.; Le Gland, G.; Nierlich, M.; Ephritikhine, M. Lanthanide Borohydrides as Precursors to Organometallic Compounds. Mono(Cyclooctatetraenyl) Neodymium Complexes. *Organometallics* **2000**, *19* (26), 5654–5660. https://doi.org/10.1021/om000558f.

(109) Chen, S.-M.; Xiong, J.; Zhang, Y.-Q.; Yuan, Q.; Wang, B.-W.; Gao, S. A Soft Phosphorus Atom to "Harden" an Erbium(III) Single-Ion Magnet. *Chem. Sci.* **2018**, *9* (38), 7540–7545. https://doi.org/10.1039/C8SC01626G.

(110) Meng, Y.-S.; Yang, M.-W.; Xu, L.; Xiong, J.; Hu, J.-Y.; Liu, T.; Wang, B.-W.; Gao, S. Design Principle of Half-Sandwich Type Erbium Single-Ion Magnets through Crystal Field Engineering: A Combined Magnetic and Electronic Structure Study. *Dalton Trans.* **2019**. https://doi.org/10.1039/C9DT01954E.

(111) *Molcas 8: New capabilities for multiconfigurational quantum chemical calculations across the periodic table - Aquilante - 2016 - Journal of Computational Chemistry - Wiley Online Library*. https://onlinelibrary.wiley.com/doi/10.1002/jcc.24221 (accessed 2019-05-05).

(112) Ungur, L.; Chibotaru, L. F. Magnetic Anisotropy in the Excited States of Low Symmetry Lanthanide Complexes. *Phys. Chem. Chem. Phys.* **2011**, *13* (45), 20086–20090. https://doi.org/10.1039/C1CP22689D.

(113) Orlova, A. P.; Hilgar, J. D.; Bernbeck, M. G.; Gembicky, M.; Rinehart, J. D. Intuitive Control of Low-Energy Magnetic Excitations via Directed Dipolar Interactions in a Series of Er(III)-Based Complexes. *J. Am. Chem. Soc.* **2022**, *144* (25), 11316–11325. https://doi.org/10.1021/jacs.2c03236.

(114) Sorace, L.; Benelli, C.; Gatteschi, D. Lanthanides in Molecular Magnetism: Old Tools in a New Field. *Chemical Society Reviews* **2011**, *40* (6), 3092–3104. https://doi.org/10.1039/C0CS00185F.

(115) Habib, F.; Murugesu, M. Lessons Learned from Dinuclear Lanthanide Nano-Magnets. *Chemical Society Reviews* **2013**, *42* (8), 3278–3288. https://doi.org/10.1039/C2CS35361J.

(116) T. Liddle, S.; Slageren, J. van. Improving F-Element Single Molecule Magnets. *Chemical Society Reviews* **2015**, *44* (19), 6655–6669. https://doi.org/10.1039/C5CS00222B.

(117) Edelmann, F. T. Lanthanides and Actinides: Annual Survey of Their Organometallic Chemistry Covering the Year 2017. *Coordination Chemistry Reviews* **2018**, *370*, 129–223. https://doi.org/10.1016/j.ccr.2018.05.013.

(118) Guo, F.-S.; Bar, A. K.; Layfield, R. A. Main Group Chemistry at the Interface with Molecular Magnetism. *Chem. Rev.* **2019**. https://doi.org/10.1021/acs.chemrev.9b00103.

(119) Goodwin, C. A. P. Blocking like It's Hot: A Synthetic Chemists' Path to High-Temperature Lanthanide Single Molecule Magnets. *Dalton Trans.* **2020**. https://doi.org/10.1039/D0DT01904F.

(120) Guo, F.-S.; Day, B. M.; Chen, Y.-C.; Tong, M.-L.; Mansikkamäki, A.; Layfield, R. A. A Dysprosium Metallocene Single-Molecule Magnet Functioning at the Axial Limit.

Angewandte Chemie International Edition **2017**, *56* (38), 11445–11449. https://doi.org/10.1002/anie.201705426.

(121) Gupta, S. K.; Murugavel, R. Enriching Lanthanide Single-Ion Magnetism through Symmetry and Axiality. *Chem. Commun.* **2018**, *54* (30), 3685–3696. https://doi.org/10.1039/C7CC09956H.

(122) Thomas-Hargreaves, L. R.; Giansiracusa, M. J.; Gregson, M.; Zanda, E.; O'Donnell, F.; Wooles, A. J.; Chilton, N. F.; Liddle, S. T. Correlating Axial and Equatorial Ligand Field Effects to the Single-Molecule Magnet Performances of a Family of Dysprosium Bis-Methanediide Complexes. *Chem. Sci.* **2021**, *12* (11), 3911–3920. https://doi.org/10.1039/D1SC00238D.

(123) McClain, K. R.; Gould, C. A.; Chakarawet, K.; Teat, S. J.; Groshens, T. J.; Long, J. R.; Harvey, B. G. High-Temperature Magnetic Blocking and Magneto-Structural Correlations in a Series of Dysprosium(III) Metallocenium Single-Molecule Magnets. *Chem. Sci.* **2018**, *9* (45), 8492–8503. https://doi.org/10.1039/C8SC03907K.

(124) Moseley, D. H.; Stavretis, S. E.; Zhu, Z.; Guo, M.; Brown, C. M.; Ozerov, M.; Cheng, Y.; Daemen, L. L.; Richardson, R.; Knight, G.; Thirunavukkuarasu, K.; Ramirez-Cuesta, A. J.; Tang, J.; Xue, Z.-L. Inter-Kramers Transitions and Spin–Phonon Couplings in a Lanthanide-Based Single-Molecule Magnet. *Inorg. Chem.* **2020**, *59* (7), 5218–5230. https://doi.org/10.1021/acs.inorgchem.0c00523.

(125) Marbey, J.; Kragskow, J. G. C.; Buch, C. D.; Nehrkorn, J.; Ozerov, M.; Piligkos, S.; Hill, S.; Chilton, N. Vibronic Coupling in a Molecular 4f Qubit. **2021**. https://doi.org/10.26434/chemrxiv.13725904.v1.

(126) Zhang, P.; Benner, F.; Chilton, N. F.; Demir, S. Organometallic Lanthanide Bismuth Cluster Single-Molecule Magnets. *Chem* **2022**, *8* (3), 717–730. https://doi.org/10.1016/j.chempr.2021.11.007.

(127) Velkos, G.; S. Krylov, D.; Kirkpatrick, K.; Liu, X.; Spree, L.; B. Wolter, A. U.; Büchner, B.; C. Dorn, H.; A. Popov, A. Giant Exchange Coupling and Field-Induced Slow Relaxation of Magnetization in Gd 2 @C 79 N with a Single-Electron Gd–Gd Bond. *Chemical Communications* **2018**, *54* (23), 2902–2905. https://doi.org/10.1039/C8CC00112J.

(128) Benner, F.; Demir, S. From Unprecedented 2,2′-Bisimidazole-Bridged Rare Earth Organometallics to Magnetic Hysteresis in the Dysprosium Congener. *Inorg. Chem. Front.* **2023**. https://doi.org/10.1039/D3QI00546A.

(129) Benner, F.; Droitte, L. L.; Cador, O.; Guennic, B. L.; Demir, S. Magnetic Hysteresis and Large Coercivity in Bisbenzimidazole Radical-Bridged Dilanthanide Complexes. *Chem. Sci.* **2023**, *14* (21), 5577–5592. https://doi.org/10.1039/D3SC01562A.

(130) Zhang, P.; Nabi, R.; Staab, J. K.; Chilton, N. F.; Demir, S. Taming Super-Reduced Bi23– Radicals with Rare Earth Cations. *J. Am. Chem. Soc.* **2023**, *145* (16), 9152–9163. https://doi.org/10.1021/jacs.3c01058.

(131) Lin, P.-H.; Burchell, T. J.; Ungur, L.; Chibotaru, L. F.; Wernsdorfer, W.; Murugesu, M. A Polynuclear Lanthanide Single-Molecule Magnet with a Record Anisotropic Barrier. *Angewandte Chemie* **2009**, *121* (50), 9653–9656. https://doi.org/10.1002/ange.200903199.

(132) Ke, H.; Gamez, P.; Zhao, L.; Xu, G.-F.; Xue, S.; Tang, J. Magnetic Properties of Dysprosium Cubanes Dictated by the M−O−M Angles of the [Dy4(M3-OH)4] Core. *Inorg. Chem.* **2010**, *49* (16), 7549–7557. https://doi.org/10.1021/ic101057e.

(133) Alexandropoulos, D. I.; Alaimo, A. A.; Sun, D.; Stamatatos, T. C. A New {Dy5} Single-Molecule Magnet Bearing the Schiff Base Ligand N-Naphthalidene-2-Amino-5-Chlorophenol. *Magnetochemistry* **2018**, *4* (4), 48. https://doi.org/10.3390/magnetochemistry4040048.

(134) Bernbeck, M. G.; Hilgar, J. D.; Rinehart, J. D. Probing Axial Anisotropy in Dinuclear Alkoxide-Bridged Er–COT Single-Molecule Magnets. *Polyhedron* **2020**, *175*, 114206. https://doi.org/10.1016/j.poly.2019.114206.

(135) Gilman, H.; Pacevitz, H. A.; Baine, O. Benzylalkali Compounds1. *J. Am. Chem. Soc.* **1940**, *62* (6), 1514–1520. https://doi.org/10.1021/ja01863a054.

(136) Weiss, E.; Sauermann, G. Darstellung Und Struktur Des Methylkaliums. *Angewandte Chemie* **1968**, *80* (3), 123–124. https://doi.org/10.1002/ange.19680800315.

(137) Kuveke, R. E. H.; Barwise, L.; van Ingen, Y.; Vashisth, K.; Roberts, N.; Chitnis, S. S.; Dutton, J. L.; Martin, C. D.; Melen, R. L. An International Study Evaluating Elemental Analysis. *ACS Cent. Sci.* **2022**. https://doi.org/10.1021/acscentsci.2c00325.

(138) Moseley, D. H.; Stavretis, S. E.; Thirunavukkuarasu, K.; Ozerov, M.; Cheng, Y.; Daemen, L. L.; Ludwig, J.; Lu, Z.; Smirnov, D.; Brown, C. M.; Pandey, A.; Ramirez-Cuesta, A. J.; Lamb, A. C.; Atanasov, M.; Bill, E.; Neese, F.; Xue, Z.-L. Spin–Phonon Couplings in Transition Metal Complexes with Slow Magnetic Relaxation. *Nature Communications* **2018**, *9* (1), 2572. https://doi.org/10.1038/s41467-018-04896-0.

(139) Neese, F. Software Update: The ORCA Program System, Version 4.0. *WIREs Computational Molecular Science* **2018**, *8* (1), e1327. https://doi.org/10.1002/wcms.1327.

(140) Neese, F. The ORCA Program System. *WIREs Computational Molecular Science* **2012**, *2* (1), 73–78. https://doi.org/10.1002/wcms.81.

(141) Jaoul, A.; Nocton, G.; Clavaguéra, C. Assessment of Density Functionals for Computing Thermodynamic Properties of Lanthanide Complexes. *ChemPhysChem* **2017**, *18* (19), 2688–2696. https://doi.org/10.1002/cphc.201700629.

(142) Pantazis, D. A.; Neese, F. All-Electron Scalar Relativistic Basis Sets for the Lanthanides. *J. Chem. Theory Comput.* **2009**, *5* (9), 2229–2238. https://doi.org/10.1021/ct900090f.

(143) *Chemcraft - Graphical program for visualization of quantum chemistry computations*. https://www.chemcraftprog.com/ (accessed 2022-07-18).

(144) Hodgson, K. O.; Raymond, K. N. Dimeric .Pi.-Cyclooctatetraene Dianion Complex of Cerium(III). Crystal and Molecular Structure of [Ce(C8H8)Cl.20C4H8]2. *Inorg. Chem.* **1972**, *11* (1), 171–175. https://doi.org/10.1021/ic50107a037.

(145) Mashima, K.; Nakayama, Y.; Nakamura, A.; Kanehisa, N.; Kai, Y.; Takaya, H. A New Convenient Preparation of Monocyclooctatetraenyl-Lanthanide Complexes from Metallic Lanthanides and Oxidants. *Journal of Organometallic Chemistry* **1994**, *473* (1), 85–91. https://doi.org/10.1016/0022-328X(94)80108-8.

(146) Zhang, S.; Wei, G.; Chen, W.; Liu, J. Synthesis and Crystal Structure of (C8H8)Dy[μ-OCH2(CH2)2CH☐CH2(THF)2. *Polyhedron* **1994**, *13* (12), 1927–1930. https://doi.org/10.1016/0277-5387(94)80016-2.

(147) Cendrowski-Guillaume, S. M.; Nierlich, M.; Lance, M.; Ephritikhine, M. First Chemical Transformations of Lanthanide Borohydride Compounds: Synthesis and Crystal Structures of [(η-C8H8)Nd(BH4)(THF)]2 and [(η-C8H8)Nd(THF)4][BPh4]. *Organometallics* **1998**, *17* (5), 786–788. https://doi.org/10.1021/om9709446.

(148) Cendrowski-Guillaume, S. M.; Le Gland, G.; Nierlich, M.; Ephritikhine, M. Lanthanide Borohydrides as Precursors to Organometallic Compounds. Mono(Cyclooctatetraenyl) Neodymium Complexes. *Organometallics* **2000**, *19* (26), 5654–5660. https://doi.org/10.1021/om000558f.

(149) Visseaux, M.; Nief, F.; Ricard, L. Synthesis of Mixed Phospholyl/Cyclooctatetraenyl–Lanthanide Complexes. Crystal and Molecular Structure of (Cyclooctatetraenyl)[3,4-Dimethyl-2,5-Bis(Trimethylsilyl)-Phospholyl](Tetrahydrofuran)Neodymium. *Journal of Organometallic Chemistry* **2002**, *647* (1), 139–144. https://doi.org/10.1016/S0022-328X(01)01402-4.

(150) Evans, W. J.; Champagne, T. M.; Davis, B. L.; Allen, N. T.; Nyce, G. W.; Johnston, M. A.; Lin, Y.-C.; Khvostov, A.; Ziller, J. W. Structural Studies of Mono(Pentamethylcyclopentadienyl)Lanthanide Complexes. *Journal of Coordination Chemistry* **2006**, *59* (10), 1069–1087. https://doi.org/10.1080/00958970500512831.

(151) Meermann, C.; Ohno, K.; Törnroos, K. W.; Mashima, K.; Anwander, R. Rare-Earth Metal Bis(Dimethylsilyl)Amide Complexes Supported by Cyclooctatetraenyl Ligands. *European Journal of Inorganic Chemistry* **2009**, *2009* (1), 76–85. https://doi.org/10.1002/ejic.200800649.

(152) Edelmann, A.; Lorenz, V.; Hrib, C. G.; Hilfert, L.; Blaurock, S.; Edelmann, F. T. Steric Effects in Lanthanide Sandwich Complexes Containing Bulky Cyclooctatetraenyl Ligands. *Organometallics* **2013**, *32* (5), 1435–1444. https://doi.org/10.1021/om3010993.

(153) *OpenMolcas: From Source Code to Insight | Journal of Chemical Theory and Computation*. https://pubs.acs.org/doi/10.1021/acs.jctc.9b00532 (accessed 2021-04-14).

(154) Chibotaru, L. F.; Ungur, L.; Soncini, A. The Origin of Nonmagnetic Kramers Doublets in the Ground State of Dysprosium Triangles: Evidence for a Toroidal Magnetic Moment. *Angewandte Chemie International Edition* **2008**, *47* (22), 4126–4129. https://doi.org/10.1002/anie.200800283.

(155) Chibotaru, L. F.; Ungur, L.; Aronica, C.; Elmoll, H.; Pilet, G.; Luneau, D. Structure, Magnetism, and Theoretical Study of a Mixed-Valence CoII3CoIII4 Heptanuclear Wheel: Lack of SMM Behavior despite Negative Magnetic Anisotropy. *J. Am. Chem. Soc.* **2008**, *130* (37), 12445–12455. https://doi.org/10.1021/ja8029416.

(156) Ungur, L.; Heuvel, W. V. den; Chibotaru, L. F. Ab Initio Investigation of the Non-Collinear Magnetic Structure and the Lowest Magnetic Excitations in Dysprosium Triangles. *New J. Chem.* **2009**, *33* (6), 1224–1230. https://doi.org/10.1039/B903126J.

(157) Sievers, A. J.; Tinkham, M. Far Infrared Spectra of Rare-Earth Iron Garnets. *Phys. Rev.* **1963**, *129* (5), 1995–2004. https://doi.org/10.1103/PhysRev.129.1995.

(158) Bloor, D.; Copland, G. M. Far Infrared Spectra of Magnetic Ions in Crystals. *Reports on Progress in Physics* **1972**, *35* (3), 1173–1264. https://doi.org/10.1088/0034-4885/35/3/304.

(159) Sirenko, A. A.; O'Malley, S. M.; Ahn, K. H.; Park, S.; Carr, G. L.; Cheong, S.-W. Infrared-Active Excitations Related to Ho 3 + Ligand-Field Splitting at the Commensurate-Incommensurate Magnetic Phase Transition in HoMn 2 O 5. *Phys. Rev. B* **2008**, *78* (17), 174405. https://doi.org/10.1103/PhysRevB.78.174405.

(160) Rogers, P. D.; Choi, Y. J.; Standard, E. C.; Kang, T. D.; Ahn, K. H.; Dubroka, A.; Marsik, P.; Wang, Ch.; Bernhard, C.; Park, S.; Cheong, S.-W.; Kotelyanskii, M.; Sirenko, A. A. Adjusted Oscillator Strength Matching for Hybrid Magnetic and Electric Excitations in Dy 3 Fe 5 O 12 Garnet. *Phys. Rev. B* **2011**, *83* (17), 174407. https://doi.org/10.1103/PhysRevB.83.174407.

(161) Albino, A.; Benci, S.; Tesi, L.; Atzori, M.; Torre, R.; Sanvito, S.; Sessoli, R.; Lunghi, A. First-Principles Investigation of Spin–Phonon Coupling in Vanadium-Based Molecular Spin Quantum Bits. *Inorg. Chem.* **2019**, *58* (15), 10260–10268. https://doi.org/10.1021/acs.inorgchem.9b01407.

(162) Blockmon, A. L.; Ullah, A.; Hughey, K. D.; Duan, Y.; O'Neal, K. R.; Ozerov, M.; Baldoví, J. J.; Aragó, J.; Gaita-Ariño, A.; Coronado, E.; Musfeldt, J. L. Spectroscopic Analysis of Vibronic Relaxation Pathways in Molecular Spin Qubit [Ho(W5O18)2]9−: Sparse Spectra Are Key. *Inorg. Chem.* **2021**, *60* (18), 14096–14104. https://doi.org/10.1021/acs.inorgchem.1c01474.

(163) Stavretis, S. E.; Moseley, D. H.; Fei, F.; Cui, H.-H.; Cheng, Y.; Podlesnyak, A. A.; Wang, X.; Daemen, L. L.; Hoffmann, C. M.; Ozerov, M.; Lu, Z.; Thirunavukkuarasu, K.; Smirnov, D.; Chang, T.; Chen, Y.-S.; Ramirez-Cuesta, A. J.; Chen, X.-T.; Xue, Z.-L. (Ben). Spectroscopic Studies of the Magnetic Excitation and Spin-Phonon Couplings in a Single-Molecule Magnet. *Chemistry – A European Journal* **2019**, *25* (69), 15846–15857. https://doi.org/10.1002/chem.201903635.

(164) Kragskow, J. G. C.; Marbey, J.; Buch, C. D.; Nehrkorn, J.; Ozerov, M.; Piligkos, S.; Hill, S.; Chilton, N. F. Analysis of Vibronic Coupling in a 4f Molecular Magnet with FIRMS. *Nature Communications* **2022**, *13* (1), 825. https://doi.org/10.1038/s41467-022-28352-2.

(165) Blockmon, A. L.; Ullah, A.; Hughey, K. D.; Duan, Y.; O'Neal, K. R.; Ozerov, M.; Baldoví, J. J.; Aragó, J.; Gaita-Ariño, A.; Coronado, E.; Musfeldt, J. L. Spectroscopic Analysis of Vibronic Relaxation Pathways in Molecular Spin Qubit [Ho(W5O18)2]9−: Sparse Spectra Are Key. *Inorg. Chem.* **2021**. https://doi.org/10.1021/acs.inorgchem.1c01474.

(166) Görller-Walrand, C.; Binnemans, K. Chapter 167 Spectral Intensities of F-f Transitions. In *Handbook on the Physics and Chemistry of Rare Earths*; Elsevier, 1998; Vol. 25, pp 101–264. https://doi.org/10.1016/S0168-1273(98)25006-9.

(167) Lorenz, V.; Schmiege, B. M.; Hrib, C. G.; Ziller, J. W.; Edelmann, A.; Blaurock, S.; Evans, W. J.; Edelmann, F. T. Unprecedented Bending and Rearrangement of F-Element Sandwich Complexes Induced by Superbulky Cyclooctatetraenide Ligands. *J. Am. Chem. Soc.* **2011**, *133* (5), 1257–1259. https://doi.org/10.1021/ja109604t.

(168) Bogani, L.; Wernsdorfer, W. Molecular Spintronics Using Single-Molecule Magnets. *Nature Mater* **2008**, *7* (3), 179–186. https://doi.org/10.1038/nmat2133.

(169) Burzurí, E.; van der Zant, H. S. J. Single-Molecule Spintronics. In *Molecular Magnets: Physics and Applications*; Bartolomé, J., Luis, F., Fernández, J. F., Eds.; NanoScience and Technology; Springer Berlin Heidelberg: Berlin, Heidelberg, 2014; pp 297–318. https://doi.org/10.1007/978-3-642-40609-6_12.

(170) Ganzhorn, M.; Wernsdorfer, W. Molecular Quantum Spintronics Using Single-Molecule Magnets. In *Molecular Magnets: Physics and Applications*; Bartolomé, J., Luis, F., Fernández, J. F., Eds.; NanoScience and Technology; Springer Berlin Heidelberg: Berlin, Heidelberg, 2014; pp 319–364. https://doi.org/10.1007/978-3-642-40609-6_13.

(171) Molecular Spintronics. In *Introduction to Molecular Magnetism*; John Wiley & Sons, Ltd, 2015; pp 295–328. https://doi.org/10.1002/9783527690541.ch17.

(172) Zhao, P.; Li, J.; Jin, H.; Yu, L.; Huang, B.; Ying, D. Designing Lateral Spintronic Devices with Giant Tunnel Magnetoresistance and Perfect Spin Injection Efficiency Based on Transition Metal Dichalcogenides. *Phys. Chem. Chem. Phys.* **2018**, *20* (15), 10286–10291. https://doi.org/10.1039/C8CP00557E.

(173) Martínez-Prieto, L. M.; Marbaix, J.; Asensio, J. M.; Cerezo-Navarrete, C.; Fazzini, P.-F.; Soulantica, K.; Chaudret, B.; Corma, A. Ultrastable Magnetic Nanoparticles Encapsulated in Carbon for Magnetically Induced Catalysis. *ACS Appl. Nano Mater.* **2020**, *3* (7), 7076–7087. https://doi.org/10.1021/acsanm.0c01392.

(174) Yu, C.-J.; von Kugelgen, S.; Laorenza, D. W.; Freedman, D. E. A Molecular Approach to Quantum Sensing. *ACS Cent. Sci.* **2021**, *7* (5), 712–723. https://doi.org/10.1021/acscentsci.0c00737.

(175) Lunghi, A.; Sanvito, S. How Do Phonons Relax Molecular Spins? *Science Advances* **2019**, *5* (9), eaax7163. https://doi.org/10.1126/sciadv.aax7163.

(176) Staab, J.; Chilton, N. *An Analytic Linear Vibronic Coupling Method for First-Principles Spin-Dynamics Calculations in Single-Molecule Magnets*; preprint; Chemistry, 2022. https://doi.org/10.26434/chemrxiv-2022-kc0k3.

(177) Roy, L. E.; Hughbanks, T. Magnetic Coupling in Dinuclear Gd Complexes. *J. Am. Chem. Soc.* **2006**, *128* (2), 568–575. https://doi.org/10.1021/ja055035j.

(178) Jarenmark, M.; Carlsson, H.; Nordlander, E. Asymmetric Dinuclear Metal Complexes as Models for Active Sites in Hydrolases and Redox Enzymes. *Comptes Rendus Chimie* **2007**, *10* (4), 433–462. https://doi.org/10.1016/j.crci.2007.02.015.

(179) Lin, P.-H.; Burchell, T. J.; Clérac, R.; Murugesu, M. Dinuclear Dysprosium(III) Single-Molecule Magnets with a Large Anisotropic Barrier. *Angewandte Chemie International Edition* **2008**, *47* (46), 8848–8851. https://doi.org/10.1002/anie.200802966.

(180) Y. Chow, C.; Bolvin, H.; E. Campbell, V.; Guillot, R.; W. Kampf, J.; Wernsdorfer, W.; Gendron, F.; Autschbach, J.; L. Pecoraro, V.; Mallah, T. Assessing the Exchange Coupling in Binuclear Lanthanide(Iii) Complexes and the Slow Relaxation of the Magnetization in the Antiferromagnetically Coupled Dy 2 Derivative. *Chemical Science* **2015**, *6* (7), 4148–4159. https://doi.org/10.1039/C5SC01029B.

(181) Reed, W. R.; Dunstan, M. A.; Gable, R. W.; Phonsri, W.; Murray, K. S.; Mole, R. A.; Boskovic, C. Tetraoxolene-Bridged Rare-Earth Complexes: A Radical-Bridged Dinuclear

Dy Single-Molecule Magnet. *Dalton Trans.* **2019**, *48* (41), 15635–15645. https://doi.org/10.1039/C9DT01320B.

(182) Wu, J.; Demeshko, S.; Dechert, S.; Meyer, F. Hexanuclear [Cp*Dy]6 Single-Molecule Magnet. *Chem. Commun.* **2020**, *56* (27), 3887–3890. https://doi.org/10.1039/C9CC09774K.

(183) Houard, F.; Gendron, F.; Suffren, Y.; Guizouarn, T.; Dorcet, V.; Calvez, G.; Daiguebonne, C.; Guillou, O.; Guennic, B. L.; Mannini, M.; Bernot, K. Single-Chain Magnet Behavior in a Finite Linear Hexanuclear Molecule. *Chem. Sci.* **2021**, *12* (31), 10613–10621. https://doi.org/10.1039/D1SC02033A.

(184) Bogani, L.; Sessoli, R.; Pini, M. G.; Rettori, A.; Novak, M. A.; Rosa, P.; Massi, M.; Fedi, M. E.; Giuntini, L.; Caneschi, A.; Gatteschi, D. Finite-Size Effects on the Static Properties of a Single-Chain Magnet. *Phys. Rev. B* **2005**, *72* (6), 064406. https://doi.org/10.1103/PhysRevB.72.064406.

(185) Bernot, K.; Bogani, L.; Caneschi, A.; Gatteschi, D.; Sessoli, R. A Family of Rare-Earth-Based Single Chain Magnets: Playing with Anisotropy. *J. Am. Chem. Soc.* **2006**, *128* (24), 7947–7956. https://doi.org/10.1021/ja0611101l.

(186) Bogani, L.; Vindigni, A.; Sessoli, R.; Gatteschi, D. Single Chain Magnets: Where to from Here? *J. Mater. Chem.* **2008**, *18* (40), 4750–4758. https://doi.org/10.1039/B807824F.

(187) Gatteschi, D.; Vindigni, A. Single-Chain Magnets. In *Molecular Magnets: Physics and Applications*; Bartolomé, J., Luis, F., Fernández, J. F., Eds.; NanoScience and Technology; Springer Berlin Heidelberg: Berlin, Heidelberg, 2014; pp 191–220. https://doi.org/10.1007/978-3-642-40609-6_8.

(188) Pichon, C.; Suaud, N.; Duhayon, C.; Guihéry, N.; Sutter, J.-P. Cyano-Bridged Fe(II)–Cr(III) Single-Chain Magnet Based on Pentagonal Bipyramid Units: On the Added Value of Aligned Axial Anisotropy. *Journal of the American Chemical Society* **2018**, *140* (24), 7698–7704. https://doi.org/10.1021/jacs.8b03891.

(189) Evrard, Q.; Houard, F.; Daiguebonne, C.; Calvez, G.; Suffren, Y.; Guillou, O.; Mannini, M.; Bernot, K. Sonocrystallization as an Efficient Way to Control the Size, Morphology, and Purity of Coordination Compound Microcrystallites: Application to a Single-Chain Magnet. *Inorg. Chem.* **2020**. https://doi.org/10.1021/acs.inorgchem.0c01126.

(190) Rinehart, J. D.; Fang, M.; Evans, W. J.; Long, J. R. Strong Exchange and Magnetic Blocking in N_2^{3-}-Radical-Bridged Lanthanide Complexes. *Nature Chem* **2011**, *3* (7), 538–542. https://doi.org/10.1038/nchem.1063.

(191) Moreno Pineda, E.; Chilton, N. F.; Marx, R.; Dörfel, M.; Sells, D. O.; Neugebauer, P.; Jiang, S.-D.; Collison, D.; van Slageren, J.; McInnes, E. J. L.; Winpenny, R. E. P. Direct Measurement of Dysprosium(III)⋯dysprosium(III) Interactions in a Single-Molecule Magnet. *Nature Communications* **2014**, *5* (1), 5243. https://doi.org/10.1038/ncomms6243.

(192) Burton, N. C.; Cloke, F. G. N.; Joseph, S. C. P.; Karamallakis, H.; Sameh, A. A. Trimethylsilyl Derivatives of Cyclooctatetraene. *Journal of Organometallic Chemistry* **1993**, *462* (1), 39–43. https://doi.org/10.1016/0022-328X(93)83339-W.

(193) Hilgar, J.; Orlova, A.; Bernbeck, M. Super-Matlab, 2022. https://doi.org/110.1039/C9CP03936H.

(194) Wernsdorfer, W. Quantum Dynamics in Molecular Nanomagnets. *Comptes Rendus Chimie* **2008**, *11* (10), 1086–1109. https://doi.org/10.1016/j.crci.2008.08.005.

(195) Ho, L. T. A.; Chibotaru, L. F. Multiple Relaxation Times in Single-Molecule Magnets. *Physical Review B* **2016**, *94* (10). https://doi.org/10.1103/PhysRevB.94.104422.

(196) Ungur, L.; Chibotaru, L. F. Magnetic Anisotropy in the Excited States of Low Symmetry Lanthanide Complexes. *Phys. Chem. Chem. Phys.* **2011**, *13* (45), 20086–20090. https://doi.org/10.1039/C1CP22689D.

(197) Murrie, M.; Canaj, A.; Dey, S.; Cespedes, O.; Wilson, C.; Rajaraman, G. There Is Nothing Wrong with Being Soft: Using Sulfur Ligands to Increase Axiality in a Dy(III) Single-Ion Magnet. *Chem. Commun.* **2020**. https://doi.org/10.1039/C9CC07292F.

(198) Gram–Schmidt Process. *Wikipedia*; 2023.